



UNIVERSITÀ DEGLI STUDI DI PADOVA
DIPARTIMENTO DI INGEGNERIA INDUSTRIALE
CORSO DI LAUREA IN INGEGNERIA AEROSPAZIALE

**Tesi di Laurea Magistrale in
Ingegneria Aerospaziale**

**Fluid dynamics impact
on the performance
of a Vanadium Redox Flow Battery**

Relatore: Prof. Francesco Picano

*Laureando: MATTEO TREVENZOLO
Matricola: 1132358*

ANNO ACCADEMICO 2017 – 2018

Abstract

The vanadium redox flow batteries (VRFBs) are one of the most promising technologies for large-scale energy storage thanks to their flexible energy and power capacity configurations. Unlike other devices whose energy and power are bounded, a VRFB can easily vary its energy capacity simply by increasing or decreasing externally stored electrolyte volumes without changing its power capacity. The flow rate control is very important and can increase the efficiency of the battery. In this work, a fluid dynamics characterization of the battery has been conducted to study the behaviour of the system. The total losses that are present within the system, namely the internal resistance losses and the pump losses, have been investigated. In particular, we will consider the internal resistance as the sum of a ionic resistance and a flow resistance. We will find out that the ionic resistance depends on electrical factors and decreases as the SOC increases, while the flow resistance depends on the flow rate and the flow factor. We will see that this resistance decreases with the flow factor but only up to a certain point, and then it continues to reduce as the flow rate increases. A study of the head losses on the feeding system has been conducted to better understand where there are the major losses where to act to reduce the pump power which impacts on the efficiency of the VRFB. The battery efficiency has been studied in order to define an optimal flow rate that can allow to reach the maximum performances and minimized the total losses. Based on this optimal flow rate, a strategy of charge and discharge of the VRFB has been established to achieve the greatest overall efficiency of the battery. In addition a numerical model based on Volume Averaged Navier Stokes equations (VANS) for reacting porous media has been implemented in a parallel Fortran code. Preliminary results show a good correspondence with experimental data.

Contents

List of Figures	iv
List of Tables	v
Introduction	vii
1 Vanadium Redox Flow Battery System	1
1.1 Vanadium Redox Flow Battery functioning	1
1.2 Internal resistance and overpotential	5
1.2.1 Activation overpotential	5
1.2.2 Ohmic overpotential	6
1.2.3 Concentration overpotential	6
1.3 Main Components	7
1.4 Pros and Cons	9
1.4.1 Pros	9
1.4.2 Cons	10
1.5 Costs	10
1.6 Main VRFB plants installed	12
2 Fluid dynamics theoretical background	15
2.1 Definition of fluid	15
2.2 Eulerian and Lagrangian flow descriptions	16
2.3 The material derivative	17
2.4 Navier-Stokes equations	18
2.4.1 Continuity equation	18
2.4.2 Newton's second law (momentum equation)	19
2.4.3 Energy equation	21
2.4.4 Compressible Navier-Stokes equations	22
2.4.5 Incompressible Navier-Stokes equations	23
2.4.6 Dimensionless Navier-Stokes equations	24
2.5 Transport of chemical species	27
2.6 Flows through porous media	29
2.7 Fundamental hydraulics	34
2.7.1 Head loss in pipes	35
2.7.2 Pressure losses inside stack	41
2.7.3 Pump energy	41

3	Experimental investigation	43
3.1	The battery	44
3.2	The load	45
3.3	Acquiring and Control system	45
3.3.1	LabVIEW	45
3.3.2	Transducers	47
3.3.3	National Instruments Modules	48
3.4	Experimental campaign and data acquiring	50
3.5	Internal resistance analysis	51
3.6	Pump losses analysis	54
3.7	Optimization of electrolyte flow rate	62
3.8	Viscosity measurement and permeability	68
4	Discussion and interpretation	75
4.1	Interpretation of flow resistance results	75
4.2	Performance optimization study	77
5	Conclusions	81
A	Appendix: Numerical model	83
A.1	Numerical Method	84
A.2	Implementation	85
A.3	Simulation results and validation	87
	Bibliography	91

List of Figures

1.1	VRFB plant schematic [3].	2
1.2	MEA (Membrane Electrode Assembly) schematic illustration [3].	2
1.3	Relation between OCV and SOC.	4
1.4	Typical polarization curve [42].	6
1.5	Illustration of the parallel circulation of the electrolytes inside cells.	9
2.1	Eulerian and Lagrangian approaches [41].	16
2.2	Velocity and position of particle A at time t [41].	17
2.3	Control volume V	19
2.4	Kinds of flow relate to Re	26
2.5	Friction factor versus Re	26
2.6	Geometries that improve fluid mixing.	29
2.7	Flow in a rigid porous medium [45].	30
2.8	Porous structure.	30
2.9	Averaging volume V [44].	31
2.10	The Moody chart [41].	37
2.11	Entrance flow conditions and loss coefficient [41].	38
2.12	Exit flow conditions and loss coefficient [41].	39
2.13	Loss coefficient for a sudden contraction and a sudden expansion [41].	39
2.14	Loss coefficients of a 90° bend pipe [41].	40
3.1	VRFB plant placed in Energy Storage Lab.	44
3.2	Valve system	45
3.3	Load system	46
3.4	LabVIEW's front panel.	47
3.5	Transducers	49
3.6	Polarization curve at SOC 20%.	52
3.7	Polarization curve at SOC 40%.	52
3.8	Polarization curve at SOC 60%.	53
3.9	Polarization curve at SOC 80%.	53
3.10	Ionic resistance relates to SOC.	54
3.11	Flow resistance versus flow rate (lin-lin).	54
3.12	Flow resistance versus flow rate (log-log).	55
3.13	P_{pump} and P_{stack} vs flow rate SOC 20% (lin-lin).	56
3.14	P_{pump} and P_{stack} vs flow rate SOC 20% (log-log).	56
3.15	P_{pump} and P_{stack} vs flow rate SOC 40% (lin-lin).	57
3.16	P_{pump} and P_{stack} vs flow rate SOC 40% (log-log).	57
3.17	P_{pump} and P_{stack} vs flow rate SOC 60% (lin-lin).	57

3.18	P_{pump} and P_{stack} vs flow rate SOC 60% (log-log).	58
3.19	P_{pump} and P_{stack} vs flow rate SOC 80% (lin-lin).	58
3.20	P_{pump} and P_{stack} vs flow rate SOC 80% (log-log).	58
3.21	P_{stack}/P_{pump} versus flow rate SOC 20%.	59
3.22	P_{stack}/P_{pump} versus flow rate SOC 40%.	60
3.23	P_{stack}/P_{pump} versus flow rate SOC 60%.	60
3.24	P_{stack}/P_{pump} versus flow rate SOC 80%.	60
3.25	Performance curve Sanso PMD-641 pump [43].	61
3.26	Rappresentation of head losses.	61
3.27	Total lost power versus flow rate (SOC 20%).	63
3.28	Total lost power versus flow rate (SOC 40%).	63
3.29	Total lost power versus flow rate (SOC 60%).	64
3.30	Total lost power versus flow rate (SOC 80%).	64
3.31	Battery efficiency versus flow rate (SOC 20%).	65
3.32	Battery efficiency versus flow rate (SOC 40%).	65
3.33	Battery efficiency versus flow rate (SOC 60%).	66
3.34	Battery efficiency versus flow rate (SOC 80%).	66
3.35	Battery efficiency versus flow rate, colour map (SOC 20%).	66
3.36	Battery efficiency versus flow rate, colour map (SOC 40%).	67
3.37	Battery efficiency versus flow rate, colour map (SOC 60%).	67
3.38	Battery efficiency versus flow rate, colour map (SOC 80%).	67
3.39	P_{stack} anode/cathode vs flow rate SOC 20% (lin-lin).	69
3.40	P_{stack} anode/cathode vs flow rate SOC 40% (lin-lin).	69
3.41	P_{stack} anode/cathode vs flow rate SOC 60% (lin-lin).	70
3.42	P_{stack} anode/cathode vs flow rate SOC 80% (lin-lin).	70
3.43	Measured viscosities at different SOCs.	71
4.1	Flow resistance versus flow rate (lin-lin).	76
4.2	Flow resistance versus flow rate (log-log).	76
4.3	Gradient of active species near the active surface.	78
A.1	2D staggered grid.	84
A.2	Pencil-like decomposition [45].	86
A.3	Simulated abs velocity field.	88
A.4	Simulated pressure field).	89
A.5	Simulated abs velocity field (rescaled).	89
A.6	Simulated concentration of chemical species.	89

List of Tables

2.1	Equivalent roughness for new pipes [41].	36
2.2	Loss coefficients for pipe components.	40
3.1	Experimental tests.	51
3.2	Ionic resistances at different SOC.	53
3.3	Specifications of VRFB.	55
3.4	Data fit of P_{stack}	59
3.5	Head losses of main components of the VRFB sytem.	62
3.6	Battery efficiencies at various SOCs and applied currents.	68
3.7	Measured viscosities of positive and negative electrolyte at different SOCs [48].	69
3.8	Data fit of P_{stack} - anode.	71
3.9	Data fit of P_{stack} - cathode.	72
3.10	Data fit of P_{stack} - anode without inertial effects.	72
3.11	Data fit of P_{stack} - cathode without inertial effects.	73
3.12	Values of permeability for anode and cathode.	73
3.13	New calculated values of viscosity.	73
4.1	Battery efficiencies at various SOCs and applied currents.	79
A.1	Domain size and simulation parameters.	87
A.2	Velocity boundary conditions (N = Neumann boundary conditions, D = Dirichlet boundary conditions).	88
A.3	Pressure boundary conditions (N = Neumann boundary conditions, D = Dirichlet boundary conditions).	88

Introduction

In recent years more attention has been given to the generation of electrical energy from renewable sources such as wind and solar. The EU Horizon 2020 program has the aim to produce 20% of energy by means of renewable sources to reduce pollution [1]. However, the random and intermittent nature of these power sources induces low-quality output electricity, which affects the stability of the grid [2]. Traditional grids are often unable to provide satisfactory performance and recent studies have suggested that the grid can become instable if the production from intermittent sources exceeds 20% of the total generated power without adequate compensating measures, namely energy storage. These problems require complementing energy generation from renewable sources through energy storage systems capable of storing production surplus during some periods and of coping with higher demand in others [3].

The redox flow battery (RFB) has been one of the most promising large-scale energy storage systems thanks to flexible design, high safety, high efficiency, room temperature operation, power energy independent sizing and extremely long charge/discharge cycle life. Among the various types of RFBs, the all-vanadium redox flow battery (VRFB) is one of the most advanced batteries. This particular system was initially proposed by NASA in mid-1970s and developed by Skyllas-Kazacos in the 1980s at the University of New South Wales, using the V(II)/V(III) and V(IV)/V(V) redox couples in sulfuric acid solution as the anolyte and catholyte, respectively. These batteries have the advantage of minimizing the cross-contamination of the half-cell electrolytes that means to increase the lifetime of the device. However, the interest for this new technology was soon dampened due to its low competitiveness compared to other types of batteries in mobile applications [4]. Only in more recent times, when the need for batteries has grown due to the expansion of intermittent renewable energy sources and the inherent request for services of power quality and energy management, the VRFBs have been re-evaluated because in this field they can offer interesting performances. Thus, VRFB can be used in stationary applications that could be the simultaneous regulation of the frequency and load levelling thanks to the energy accumulated inside these devices, where it is necessary a good response time and the ability of these batteries of working overloaded for a few minutes. Other applications are the possibility of exploit the VRFB in charge stations of electric vehicles, the load peak levelling and in coupling with renewable energies as already mentioned thanks to their high capacity [5]. At the same time, other redox couples were also researched to optimize performance and reduce weaknesses. Now the most successful alternatives include zinc-bromine, iron-chromium, vanadium-bromine and vanadium-oxygen but VRFBs are the only RFB technology already commercialized [3].

The main issues of a VRFB are the total losses that characterized the system. In particular, the main losses are the resistance losses and the pump losses. In literature we can find studies about the internal resistance, which contributes to reduce the battery

efficiency. Often, this internal resistance is related to the flow rate and the flow factor. As we will see, it is better to consider the internal resistance as sum of two main components. The first one is called ionic resistance and it depends on electrical factors and does not depend on flow rate. The second one is called flow resistance, and only this component depends on flow rate and flow factor. It is clear that higher the flow rate and higher the pump power is. However, on the other hand lower the flow rate and higher the electrical losses are. So, studying the relation between the flow rate and the total power losses (pump power plus electrical power) could be useful to find out an optimal flow rate that minimized the total losses and maximize the battery efficiency. As we know, the total pump losses are composed by the losses inside the stack and the losses along the feeding system. Since there are no studies about the characterization of hydraulic losses of feeding system, it was decided to do a thorough study of our plant and to compare these losses with the stack losses.

All these studies have been conducted on a vanadium redox flow battery present in the Energy Storage Laboratory at the Dipartimento di Ingegneria Industriale of the University of Padua. Hence, the aims of this work concern the fluid dynamics characterization of the battery and the study of total losses which characterize the system, including pump losses, and internal resistance losses. The investigation of the optimal flow rate that can increase the battery efficiency and reduce the total losses of the system. The development of a head losses model to better understand the behaviour of the feeding system. Finally, it has been simulated the electrode behaviour by means of Volume Averaged Navier Stokes equations (VANS) implemented by a Fortran code and the subsequent validation with experimental data. The work is organized as follow. In chapter 1 an overview of VRFBs is given. In chapter 2 the fluid dynamics theoretical background needed to study the behaviour of a VRFB is presented. In chapter 3 the experimental setup and the experimental campaign are described. In chapter 4 the main results found from the experimental campaign are discussed and interpreted. In chapter 5 the conclusions are reassumed. In appendix A the numerical simulation of the porous medium that characterized an electrode is treated.

Chapter 1

Vanadium Redox Flow Battery System

In this chapter a short description of the Vanadium Redox Flow Battery (VRFB) functioning will be given. The reactions that occur in the cells and a quick characterization of the internal resistance and overpotentials will be presented. Moreover, the main components that characterized the system will be discussed in detail. Finally, the analyse of the costs and state of the art of these systems will be investigated and pros e cons of a vanadium redox flow battery will be considered and discussed.

1.1 Vanadium Redox Flow Battery functioning

The redox flow batteries are electrochemical systems in which the conversion of the chemical energy possessed by the electrolytes into electrical energy occurs thanks to redox reactions, and vice versa. The configuration of VRFB mainly consists of two electrolyte tanks, containing the electrolyte solutions, $\text{VO}_2^+/\text{VO}^{2+}$ and $\text{V}^{3+}/\text{V}^{2+}$, into the cathode and anode compartment respectively, two pumps for the flow rate management and the battery, consisting in a stack in which each single cell is connected in series.

Membrane-electrode assemblies (MEAs) constitute the active part of each single cell, each formed of two electrodes separated by an electrolyte. The electrodes are made of porous media where the electrolyte solutions, catholyte at the positive electrode and anolyte at the negative electrode, are pumped to produce the electrochemical half-reactions. The porous electrodes are typically made of carbon or graphite felts or paper. The electrolyte separating the electrodes is a polymeric membrane that prevents the two electrolytic solutions from mixing and allows the migration of ions but not of electrons which are thus forced to pass into the external circuit generating the current. A typical membrane is made of Nafion. Figure 1.1 shows the schematic illustration of a VRFB. The electrolytes consist in two solutions of vanadium ions dissolved in aqueous sulfuric acid ($\sim 5\text{M}$) which are pumped from tanks to their respective half-cells by means of two pumps.

During charging at the positive electrode tetravalent vanadium V(IV) within VO^{2+} ions is oxidized to pentavalent vanadium V(V) within VO_2^+ ions and the electron is released, while at the negative electrode trivalent ions V^{3+} are reduced to bivalent ions V^{2+} . During discharging at the negative electrode bivalent ions V^{2+} are oxidized to

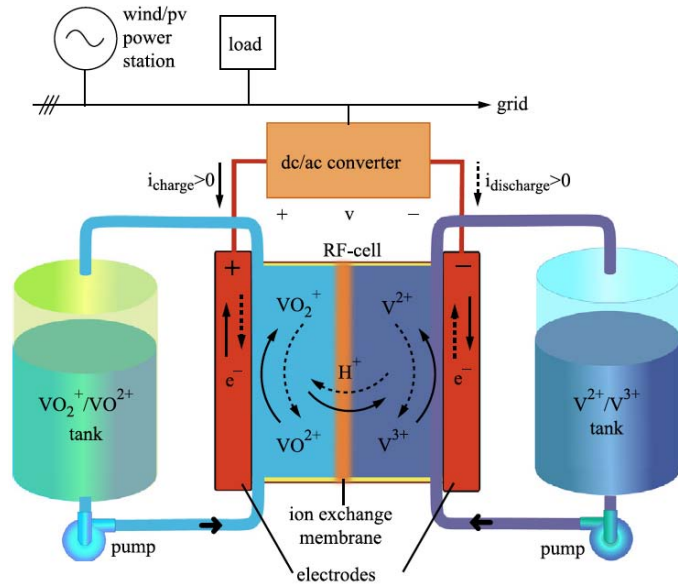


Figure 1.1: VRFB plant schematic [3].

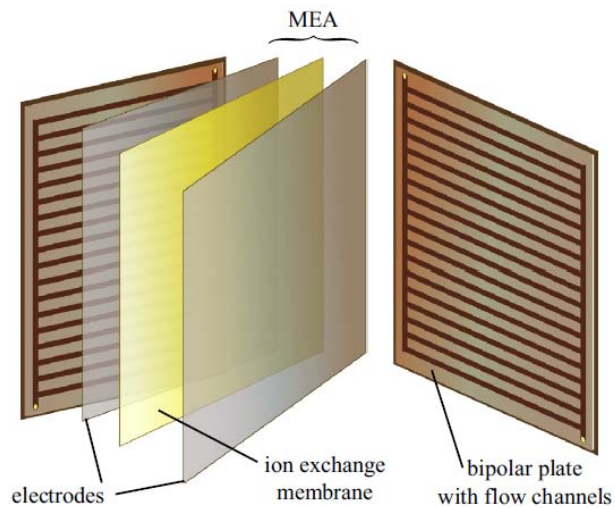
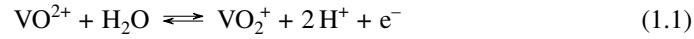


Figure 1.2: MEA (Membrane Electrode Assembly) schematic illustration [3].

trivalent ions V^{3+} and the electron is released, while at the positive electrode pentavalent vanadium V(V) within VO_2^+ ions is reduced to tetravalent vanadium V(IV) within VO^{2+} ions. The hydrogen ions $2H^+$ move through the membrane to maintain the electrical neutrality of the electrolytes [1]. The exchanged electrons are transported in the porous matrix of the carbon electrode up to the current collectors through the graphite plates. The reactions that occur in the electrodes can be expressed as [1]:

At the positive electrode:



At the negative electrode:



The total reaction is:



These reactions produce the positive electrode and negative electrode electrochemical potentials which can be expressed by the Nernst equations [1] as follows:

- Positive electrode electrochemical potential:

$$E_p = E_p^0 + \frac{RT}{F} \ln \left(\frac{a_{V_5} a_{H^+}^2}{a_{V_4}} \right) \quad (1.4)$$

- Negative electrode electrochemical potential:

$$E_n = E_n^0 + \frac{RT}{F} \ln \left(\frac{a_{V_3}}{a_{V_2}} \right) \quad (1.5)$$

While the cell electrochemical potential is given by the difference between positive and negative electrochemical potentials as:

$$E = E_p - E_n = E_p^0 + \frac{RT}{F} \ln \left(\frac{a_{V_2} a_{V_5} a_{H^+}^2}{a_{V_3} a_{V_4}} \right) \quad (1.6)$$

Where E_p^0 and E_n^0 are equilibrium potentials in equilibrium standard conditions, c_i are the activities of the ions inside the electrolytes, approximated with the concentrations of the vanadium ions, R is the universal gas constant, F is the Faraday constant and T is the temperature. The values of E_p^0 and E_n^0 are respectively:

$$E_p^0 = 1.004 \text{ V} \quad (1.7)$$

$$E_n^0 = -0.255 \text{ V} \quad (1.8)$$

The equilibrium standard potential is given by the difference between the positive and negative equilibrium standard potentials:

$$E^0 = E_p^0 - E_n^0 = 1.259 \text{ V} \quad (1.9)$$

The concentrations of each vanadium ions with a certain valence inside the electrolytes keep changing during the charge and discharge cycle, while the total vanadium ions

concentration is approximately constant in both the positive and negative electrolytes. To describe the relative amount of vanadium ions with different valences the State of Charge (SOC) is defined as:

$$SOC = \frac{c_{V^{2+}}}{c_{V^{2+}} + c_{V^{3+}}} \quad (1.10)$$

$$SOC = \frac{c_{V^{5+}}}{c_{V^{4+}} + c_{V^{5+}}} \quad (1.11)$$

The Open Circuit Voltage (OCV) is related to the SOC by means of the Nernst equation:

$$OCV = E^0 + \frac{RT}{F} \ln\left(\frac{c_{V^{2+}}c_{V^{5+}}c_{H^+}^2}{c_{V^{3+}}c_{V^{4+}}}\right) + \frac{RT}{F} \ln\left(\frac{c_{H^+}^C}{c_{H^+}^A}\right) \quad (1.12)$$

Where the last term in the right side of the equation indicates the difference of potential created by the different concentration of protons inside the two half cells at the ends of the membrane in open circuit. If the concentrations of ions are expressed in terms of initial concentrations and SOC, the Nernst equation can be write as:

$$OCV = E^0 + \frac{RT}{F} \ln\left(\frac{SOC^2(c_{H^+} + SOC)^2}{(1 - SOC)^2}\right) + \frac{RT}{F} \ln\left(\frac{c_{H^+}^C}{c_{H^+}^A}\right) \quad (1.13)$$

This relation is shown in figure 1.3. It is worth noting that there is a linear relation between SOC and OCV in a wide range that corresponds the normal operative field of the battery, while when the solutions are very charge or very discharge, at small variations of SOC correspond great gradients of OCV and thus of performance of the battery. It is important to underline that this relation doesn't consider the imbalance phenomena of the battery.

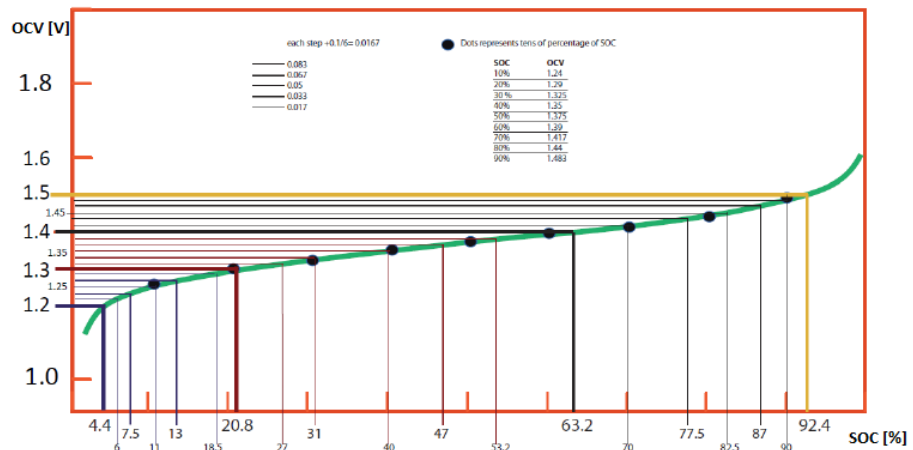


Figure 1.3: Relation between OCV and SOC.

1.2 Internal resistance and overpotential

Total storage capacity, maximum charge and discharge rates and the roundtrip efficiency are the most important parameters which characterize the performance of a battery. The major losses are the internal resistance losses and the pump losses. As the current, also the flow rate is an input parameter. One of the aims of this study is to investigate the relation between the flow rate and the major losses in order to find an optimal flow rate management related to the State of Charge (SOC) and the imposed current that can maximize the performance of the VRFB. In this section the internal resistance and overpotentials are treated. At first a short introduction of the theoretical background is given and then the results of the experimental campaign will be discussed in the following chapters.

The internal resistance R_{int} of a battery is due to the ohmic resistance of the cell components (planar and porous collectors), the resistance of electrolytes and the resistance caused by overpotentials on the surface of the electrodes, as shown below:

$$R_{int} = R_{Ohm} + R_{ele} + R_{\eta} \quad (1.14)$$

According to the Ohm's law, the internal resistance can be determined by:

$$R_{int} = \frac{OCV - V}{I} \quad (1.15)$$

Where OCV is the open circuit voltage, V is the stack voltage, and I is the electric current.

So, during the charge or discharge process, the difference between the OCV and voltage V is called overpotential and it is due to the sum of three voltage drops, namely the activation overpotential, the ohmic overpotential and the concentration overpotential associated with different magnitudes of applied current. Summing up, the overpotential is given by:

$$\eta = OCV - V \quad (1.16)$$

$$\eta = \eta_{act} + \eta_{con} + \eta_{Ohm} \quad (1.17)$$

A polarization curve is a key graphic that characterizes the functioning of a battery. These curves report on the x-axis the value of current and on the y-axis the value of voltage. As shown in figure 1.4, from this curve it is possible to identify three zones representative of three main causes of losses due to the activation overpotential, the ohmic overpotential and the concentrated overpotential.

1.2.1 Activation overpotential

The activation losses are caused by activation overpotential that defines the energy required for an electron to get transferred from electrode to electrolyte. This kind of loss is visible at low values of current, but it is worth mentioning that in VRFBs they are considerably minimized because the electrode thickness is thick enough, so the activation overpotential can be significantly reduced as a consequence of a major effective surface areas. This overpotential can be represented by the Butler-Volmer equation given by:

$$J = J_0 \left\{ \exp \left[\frac{\alpha_a z F \eta_{act}}{RT} \right] - \exp \left[-\frac{\alpha_c z F \eta_{act}}{RT} \right] \right\} \quad (1.18)$$

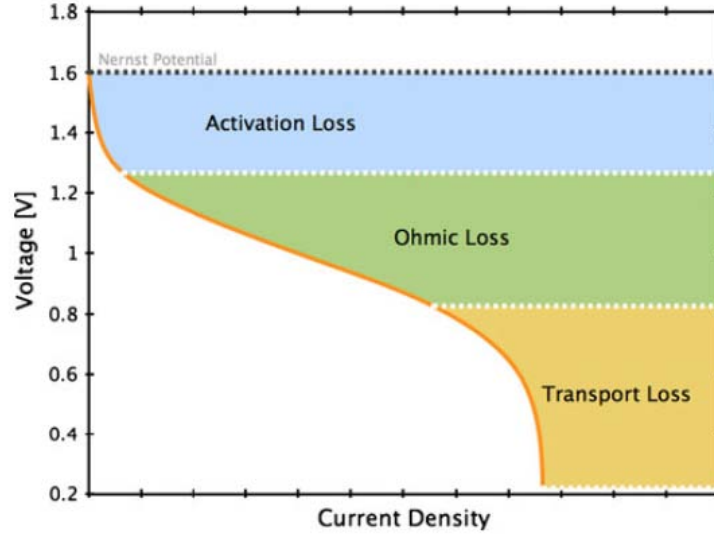


Figure 1.4: Typical polarization curve [42].

Where J_0 is the exchange current density, α_a and α_c are the dimensionless anodic and cathodic charge transfer coefficients respectively, F is the Faraday constant, T is the temperature, R is the universal gas constant and z are the electrons involved in the redox reaction.

1.2.2 Ohmic overpotential

The ohmic losses are caused by ohmic overpotential. Ohmic losses occur in a flow cell because the cell resistance which is the summation of the resistances of membrane, electrode and electrolyte reduce the current flow along the electric path. The membrane and the electrodes most contribute on the overall cell resistance, therefore it is desirable to develop materials with a small resistivity. This overpotential is given by the Ohm's law as shown below:

$$\eta_{Ohm} = \eta_m + \eta_e + \eta_{ely} \quad (1.19)$$

$$\eta_{Ohm} = IR_m + IR_e + IR_{ely} \quad (1.20)$$

Where the Subscripts 'm', 'e' and 'ely' denotes membrane, electrode and electrolyte, respectively. So, the relation between the ohmic overpotential and the current is linear, therefore also the polarization curve is linear where there are ohmic losses.

1.2.3 Concentration overpotential

The concentration losses are caused by the concentration overpotential in turn caused by the difference between reactant concentration near the surface of the electrode and the bulk electrolyte concentration, so the limiting factor is the transport of reactants on the active sites of the electrode. The concentration overpotential occurs at large applied currents and it is particularly dominant at the end of charge or discharge in a flow battery cell when the concentrations of the active species for the redox reaction are

low. Concentration overpotential can be mathematically defined by the Nernst equation as follows:

$$\eta_{con} = \frac{RT}{zF} \ln \frac{C_0}{C_b} \quad (1.21)$$

Where C_0 is the reactant concentration at the electrode surface and C_b is the bulk concentration in solution. Since the mechanism for mass transfer between the electrode surface and bulk solution is diffusion, the Fick's law can be applied to determine the diffusion rate and the final equation for determining concentration overpotential is given by:

$$\eta_{con} = \frac{RT}{zF} \ln \left(1 - \frac{J}{1.6E^{-4}zF(Q/A_e)C_b} \right) \quad (1.22)$$

Where Q is the volumetric flow rate and A is the area of porous electrode. It is worth noting that the higher the flow rates and the lower the concentration overpotential. Therefore, at the end of charge or discharge the flow rate can significantly influence the cell voltage or the stack voltage avoiding a possible premature voltage cut-off. However, on the other hand, as we will see the higher the flow rates and the higher the pump losses. So, an optimal flow rate is needed to reach the maximum performance of a battery.

1.3 Main Components

The main components in a VRFB are the positive and negative electrolytes, the electrodes, the bipolar plates and the membranes that formed the cells which constitute the stack.

The electrolyte is produced by dissolving from 0.1 M to 2 M of VO_2^+ in 0.1 M - 5 M of H_2SO_4 in water solutions. There are two main critical issues: the high cost of the vanadium salts and its low solubility. To reduce the costs, it is possible to replace the VO_2^+ with V_2O_5 (vanadium pentoxide), also called vanadic anhydride, but it is worth reminding that it is extremely toxic if breathed, therefore it is necessary more precaution during the preparation of the electrolyte [7]. The use of sulfuric acid is necessary against the precipitation of vanadium salts, even if it can occur according to the temperature. Indeed, the vanadium V(II), V(III) and V(IV) tend to precipitate if the temperature is less than 10°C , while the vanadium V(V) tends to precipitate at high state of charge when the temperature rises over 40°C . To improve the vanadium solubility, it is possible to add some additives. It is essential to avoid the precipitation of vanadium because it could cause the obstruction of the flow fields inside the stack.

Proton exchange membrane (PEM) is a polymeric electrolyte used to separate the positive and negative electrode and prevents the crossover of the two electrolytes allowing the ions transport between the catholyte and anolyte but not of electrons which are thus forced to pass into the external circuit generating the current. Two important intrinsic properties of PEM are proton conductivity and vanadium permeability. These characteristics depend on thickness of the membrane. Thicker membranes were observed to cause higher cell resistance while thinner membranes cause larger vanadium crossover flux, both of which had negative impacts on the cell performance. Thus, combining these two negative effects it is possible to find the optimal membrane thickness that can increase the overall efficiency of the battery as investigated in [6]. The most used membranes are made of Nafion because they present a high chemical stability, even if one of the limits of this material is the high cost. Another limit is the transfer of water during charge/discharge cycles caused by vanadium ions bound with

water which cross the membrane. This cause the variation of the volume of the electrolytes inside tanks. Moreover, the migration of vanadium ions through the membrane produces a capacity loss, but it can be reprinted by the remixing of the solutions [5]. In recent years other materials have been tested to reduce the costs and improve the performance. One of the better candidates for use as VRFB separators is randomly sulfonated aromatic backbone-based polymers [6].

The electrode is one of the critical component in a VRFB. The electrodes don't take part in the electrochemical reaction directly but provides proper electrochemical reaction sites for the active substances because the redox reactions occur on the electrode surface. The electrode materials must have stable three-dimensional network structure, relatively low cost, large surface area to increment the mass transport and reduce the concentration polarization losses, high conductivity to reduce the ohmic polarization losses, and good chemical and electrochemical stability [2]. The typical electrodes are made of carbon felts or carbon paper. However, modification of the electrode materials is still necessary to enhance the kinetic reversibility and electrochemical activity to reduce the electrochemical polarization. There are more possibilities to enhance the performance of the electrode. One way is using heat treatment and depositing conductive metals such as Pt, Au, Ir, Pd, Ru, Mn_3O_4 , WO_3 and Bi, which reduce the activation barrier for the redox conversion. It was found that the electrode modified with Bi shows the better electrochemical behaviour [8][9][10]. Another method to improve the electrode performance is the compression of the electrode. This method doesn't increase the costs and favours the contact with bipolar plates and membrane reducing the internal resistance. The specific resistance should be low to better transfer the electrons through the electrode and thus improve the efficiency of the cell. The specific resistance decreases with an increase of the percentage of the electrode compression. On the other hand, an excess of electrode compression causes a lower porosity that means increase the electrolyte transport that leading to lower charge/discharge properties. In [2] it is found that a cell with a 30% compression electrode was found to be the best sample observed in this study in terms of capacity and maximum power. However, a cell with a 20% compression electrode has shown the highest energy efficiency due to the combined effects of cell resistance and electrolyte transport property. Another aspect of the electrode is its thickness. Increasing the electrode thickness initially improve the overall performance because the activation loss is reduced by means of an increased of the reaction active area. But on the other hand, when the thickness of the electrode reaches a certain value, the active surface area is enough for the electrochemical reactions. Thus, a higher increment of the electrode thickness leads to in the increase of the internal resistance which consists of the electronic resistance, ionic resistance and contact resistance [11].

Bipolar plates are necessary to keep the electrode's contact and to connect the cells in series. These components are usually made of graphite. This material is expensive and mechanically fragile. Moreover, it presents a weak behaviour against the oxidation at high anodic potential, thus it is necessary a good voltage control to protect these components [12]. There are bipolar plates with flow fields or without flow fields. A flow field is a component photo engraved above the bipolar plate and serves to macroscopically distribute reactants onto electrodes. Many researches have demonstrated that the battery with flow fields has a higher discharge voltage at higher flow rates, but exhibits a larger pressure drop. In [11] it was found that the battery with flow fields shown 5% higher energy efficiency than the battery without flow fields, when the batteries work at the flow rates corresponding to battery's maximum power-based efficiency.

Pumps are essential to pump the catholyte and anolyte from tanks to the stack. In

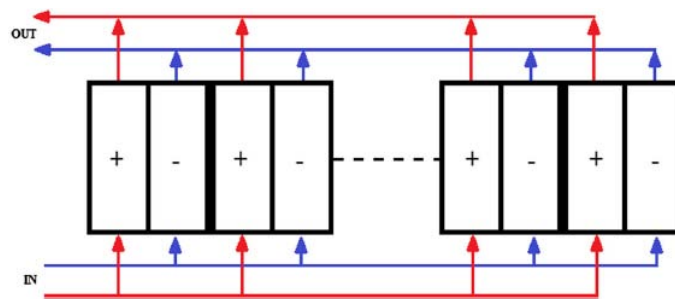


Figure 1.5: Illustration of the parallel circulation of the electrolytes inside cells.

conventional stack, cells are connected electrically in series and fed hydraulically in parallel as it is possible to see in figure 1.5. The feeding system is composed by pipes made of plastic because the electrolytes are corrosive, and they cannot be in contact with metallic parts. Even tanks, which contain the positive and negative electrolytes are made of plastic for the same reason. Moreover, flow meters, pressure meters and thermometers are present in academic systems to control some parameters like flow, pressure and temperature of electrolyte but they are not necessary in industrial plants.

1.4 Pros and Cons

1.4.1 Pros

- In RFBs power supplied is separated from energy storage. The power supplied is proportional at cell surface, cell active area and composition of stack; the energy storage depends on electrolyte volume and the concentrations of each reagent species. This feature allows for virtually unlimited capacity simply by using larger storage tanks. Practically speaking, energy of present designs spans from 10^2 to 10^7 Wh. Moreover, a charged battery is always available simply by replacing the electrochemical solutions;
- long life of materials because the redox reactions occur on the porous electrodes surface which provide the active sites on which the charge transfer takes place without matter exchange. Therefore, these RFBs do not undergo significant degradations. Moreover, the RFBs can sustain full charges and discharges without suffering damage and they do not feel the influence of the number of charge and discharge cycles;
- the electrolyte solutions have virtually unlimited life because RFBs operate by changing the metal ion valence, without consuming ion metals, thereby allowing for long cycle service life. In VRFBs the choice of the same metal in both reactions minimizes all the possible consequences of the inevitable contamination from one half-cell to another. Despite the high selectivity of the membranes against all species other than protons, it is not possible to completely eliminate the crossover from active ions, but while in the case of batteries with distinct reagents this would also result in irreversible degradation of the solutions, in the VRFB the only consequence is the progressive reduction of battery capacity. But

in VRFBs the original state can be periodically restored simply by re-mixing and re-balancing the electrochemical solutions;

- cell temperature can be easily controlled by regulating the electrolyte flow, allowing to operate the cells in the optimal conditions, e.g. at maximum efficiency;
- the kinetic of the reactions is intrinsically fast and this allows to reduce the response times of the system: the vanadium batteries can guarantee a service of regulation in frequency much faster than the common generators and to satisfy requests of power in times of the order of milliseconds. The times of discharge are very flexible and no self-discharges occurs because the two electrolytes are stored in different tanks, and cells can be left completely discharged for long periods with no negative effects. Finally, the VRFB exhibit high reliability and efficiency, which in plants of medium-large size is equal to 80% - 90%.

1.4.2 Cons

- VRFBs low power and energy densities, 0.15 W/cm² in the cells, 100 W/kg in the stack, and 25 Wh/kg in the solutions, imply large stacks and tanks, which are acceptable in stationary applications but are not acceptable in mobile applications at present. The power density and energy density of RFBs are low compared to other technologies because of the low cell potential, the limited number of exchange electrons and the solubility of vanadium which limits the maximum concentrations of reagents;
- after repeated charge/discharge cycles, crossover produces a net transfer of vanadium from one compartment to the other, solution imbalance and a reduction of the battery capacity;
- the viscosity of liquid reactants and the large cell active area imply relatively high pressure drops in the battery piping and related pumping power. Moreover, since the electrolytes are conductive, they are prone to shunt currents: the difference of potential between the cells which form the same stack implies the formation of currents from a cell to the other through distribution channels. Since reducing pumping power calls for short and large piping, whereas reducing shunt currents calls for long and small diameter piping, conflicting constraints arise, which are typically handled adopting piping sized to minimize the overall losses. These shunt currents and pumping losses reduce the RFB efficiency;
- RFBs are expensive enough, the higher costs are represented by electrolytes and membranes. An accurate analysis of the costs is accurately discussed in the next paragraph.

1.5 Costs

The VRFB is one of the most promising stationary electrochemical storage systems and the reduction of the costs is one of the major challenge. In [13] an analysis about the costs of these systems has been investigated based on the available studies published from 2004 to present. It is worth noting that a VRFB is a technology which was born 30 years ago but only in recent years it became a promising choice for energy storage, therefore the cost evaluations available are usually rough estimates. Moreover, VRFB

systems are scalable in a wide range of power and energy capacity. Systems that typically are present in literature are in a range of 2 KW-50 MW with an energy to power ratio E/P of 0.25-150 h. The most frequent batteries are in the range 1 MW-4MW with a single cell area below of 0.2 m². Raw material prices of vanadium are specified in \$ kg⁻¹ or €kg⁻¹ and are highly variable. From 2002 to 2017 prices of vanadium and vanadium pentoxide have been fluctuating in a range of 6-52 €kg⁻¹ and 2-45 €kg⁻¹, respectively. In future the authors think that it will be a dramatic reduction of the cost between -25% and -66%. Vanadium contributes for the 99% of the cost of electrolyte. Other costs are represented by manufacturing costs. The energy specific cost calculated from literature data are in a range of 45-334 €(kWh)⁻¹ [14][15]. However, in other studies the proportion of vanadium to electrolyte costs is approximately 90% or even less than 90%. In conclusion, according to many studies the vanadium electrolyte is evaluated very differently and accounts for 30-60% of total system costs.

The membrane is a key component in the VRFB cell. The typical membranes are made of Nafion. Nafion is quite cost, so alternative materials are under evaluation. Membrane costs are usually expressed in terms of areas (\$ m⁻² or €m⁻²), because membranes are thin films. Now membrane costs are in the range of 16-451 €m⁻². The wide range is due to different assumptions about the membrane material, thickness and production volume. The average price of Nafion membranes of all types (Nafion 112, 115, 117, 212) calculated is 300 €m⁻² in the present scenario. According to the available literature the membrane cost is about 3-30% of overall system cost.

In VRFB cells bipolar plates made from graphite are commonly used. Bipolar plates costs are usually expressed in \$ m⁻² or €m⁻². Plate costs are in a wide range of 37-418 €m⁻² with an average of 100 €m⁻² in present scenario [16][17][18]. The wide variability of the costs depends on material composition, plate geometry and manufacturing method adopted.

Felt electrode is another key component of the cells in the stack. The electrodes are general made of carbon felts and the costs are variable in the range of 14-63 €m⁻² with one exception of 150 €m⁻². The cost depends on the thickness and construction material. The overall average is 53 €m⁻² [19][20][21][22]. Costs for felt electrodes are expected to drop to about 16 €m⁻² [23]. The cost about felt electrodes is below 5% of the total cost.

According to [13] and the literature considered inside it the total costs related to energy capacity are in a range of 155-1738 €(kWh)⁻¹ in present day scenario. In an optimistic future scenario, the total costs will be in a range of 89-589 €(kWh)⁻¹. The total costs related the power are in a range of 884-12931 €kW⁻¹ in present day scenario and in a range of 564-2355 €kW⁻¹ in an optimistic future scenario. The realistic cost assumptions for VRFB systems are dependent on ratio E/P or the discharge duration. For example, for systems in a power range of 10-1000 kW providing energy for 4 h or 8 h capital costs of 650 €(kWh)⁻¹ and 550 €(kWh)⁻¹ respectively are applicable. It is worth noting that the European Commission has given the line guides about the development of future competitive Electrochemical energy storage systems (ECES). It has indicated a target of 150 €(kWh)⁻¹ and 5000 cycles life. Considering that VRFB systems prized around 600 €(kWh)⁻¹ and had an extremely long charge/discharge cycle life over 20000 (which considering daily charge/discharge cycles corresponds to 480000 h of operation), it is simple understood why VRFBs are one of the most promising choice for future energy storage.

1.6 Main VRFB plants installed

In the last few years more and more companies have installed these plants. There are VRFBs for industrial use and VRFBs for domestic use. Typical systems are in the order of kW to MW. Some of the major plants installed are described below in chronological order.

- 1996: 200 kW/800 kWh installed by Mitsubishi Chemicals at kashima-Kita Electric Power, Japan, for load-levelling [24].
- 1996: 450 kW/900 kWh installed by Sumitomo Electric Industries at Tasumi Sub-Station, Kansai Electric, Japan, for peak-shaving.
- 2000: 200 kW/1.6 MWh installed by Sumitomo Electric industries at Kansai Electric, Japan, for peak-shaving.
- 2001: 170 kW/1 MWh installed by Sumitomo Electric industries at Hokkaido Electric Power Wind farm, Japan, for wind turbine output power stabilization.
- 2001: 1.5MW/1.5MWh installed by Sumitomo Electric Industries in a semiconductor fabrication plant at Tottori Sanyo Electric, Japan, for peak-shaving and emergency back-up power [25].
- 2001: 250kW/500kWh installed by VRB Power at Stellen-bosch University for ESKOM Power Corporation, South Africa, for peak-shaving and UPS back-up power.
- 2001: 500kW/5MWh installed by Sumitomo Electric Industries at Gwansei Gakuin University, Japan, for peak-shaving.
- 2001: 45kW/90kWh installed by Sumitomo Electric Industries at CESI, Milan, Italy, for R& D about distributed power systems.
- 2003: 500kW/2MWh installed by Sumitomo Electric Industries in a High-Tech factory in Japan for UPS/peak-shaving [25].
- 2003: 250kW/1MWh installed by Pinnacle VRB for Hydro Tasmania at Huxley Hill Wind Farmon King Island for wind energy storage and diesel fuel replacement [26].
- 2004: 250kW/2MWh installed for Pacific Corp by VRB Power at Castle Valley, Moab, US-UT, for voltage support and rural feeder augmentation [27].
- 2005: 4MW/6MWh installed by Sumitomo Electric Industries for Electric Power Development Co, Ltd in Tomamae, Hokkaido, Japan, for wind energy storage and wind power stabilization [28].
- 2010: 100kWh made of 18kW stacks in Vierakker, The Netherlands, by Cellstrom GmbH, Austria.
- 2012: 1 MW/5 MWh installed by Sumitomo Electric Industries at Yokohama, Japan, for energy storage and support of a solar plant.
- 2015: 1 MW/4 MWh installed by Flow battery builder UniEnergy Technologies (UET) at the Turner Substation in Pullman, Washington, to support Washington State University's smart campus operations [29].

- 2015: 15 MW/60 MWh installed by Hokkaido Electric Power Co at Also, Japan, for frequency regulation [30].
- 2017: 2 MW/ 8 MWh installed by UniEnergy Technologies (UET) and Snohomish County Public Utility District (SnoPUD) at SnoPUD substation in Everett, Washington, powerful enough to keep the lights on in as many as 1000 homes for eight hours [31][32].
- 2017: 2 MW/ 8 MWh installed by Utility San Diego Gas and Electric (SDG&E) and Sumitomo Electric (SEI) at San Diego, California, to study how the technology can reliably integrate renewable energy and improve flexibility in grid management [33].

Chapter 2

Fluid dynamics theoretical background

In this chapter some of the most important aspects of fluid dynamics will be presented. The fluid dynamics is that discipline that studied the behaviour of liquids and gases.

2.1 Definition of fluid

Liquids (water, oil, etc.) can be easily deformed and can be spilled into containers or forced through a tube because the molecules are spaced farther apart and have a lot of freedom of movement. Moreover, the intermolecular forces are small. Gases (air, oxygen, etc.) have also greater molecular spacing and freedom of motion with negligible intermolecular forces. So, gases can be easily deformed and can fill whatever container in which they are placed. Both liquids and gases are fluids.

A fluid is a substance which deforms continuously when acted on by a shearing stress of any magnitude. A shearing stress is a force per unit area created whenever a tangential force acts on a surface.

Fluids are composed by molecules. To characterize the behaviour of a fluid, we consider the average value of the quantity of interest evaluated over a small control volume containing a large number of molecules. This volume is small compared with the physical dimension of the considered system, but large compared with the average distances between molecules. For gases at standard conditions the average distance between molecules is on the order of 10^{-9} m, and for liquids it is on the order of 10^{-10} m. The number of molecules per cubic millimeter is on the order of 10^{18} and 10^{21} for gases and liquids respectively. So, the high number of molecules in a very small volume demonstrates that using average values evaluated over this volume is reasonable. We can treat the fluid as a continuum and assume that all the fluid characteristics such as pressure, velocity, etc. vary continuously throughout the fluid.

To describe a fluid flow there are numerous parameters available. The physical size of the flow L , the speed of the flow U , and the pressure of the flow P are three of the most important parameters.

2.2 Eulerian and Lagrangian flow descriptions

There are two approaches to describe a flow. The first method is called *Eulerian method*. In this case we observe what happens to the fluid particle that flows at fixed points in space. Pressure, density, velocity, etc. are expressed as functions of space and time. The Eulerian method is ideal to describe an infinite number of particles. The final equations are non-linear.

The second method is called *Lagrangian method*. We observe what happens to the fluid particle during its motion and how the fluid properties change as a function of time. This method is convenient to determine the motion of individual fluid particles.

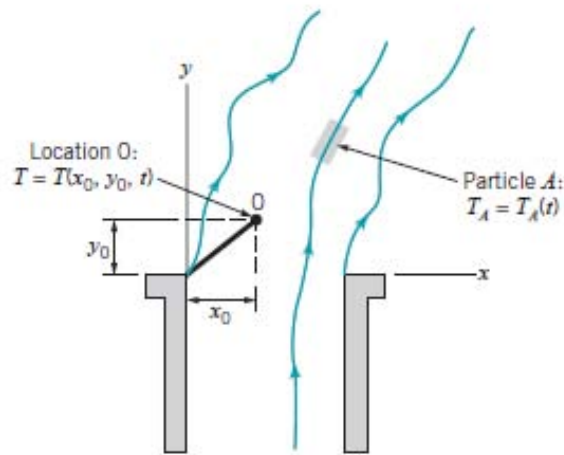


Figure 2.1: Eulerian and Lagrangian approaches [41].

Example: figure 2.1 shows smoke going up a chimney. Try to understand the differences between the Eulerian and Lagrangian approach:

- *Eulerian approach*: consider attaching a thermometer to the top of chimney (point O) and to record the temperature at that point as a function of time. As different smoke particles pass through the point O the temperature changes. So, we can obtain the temperature $T(x_0, y_0, z_0, t)$. The use of numerous fixed thermometers at various locations would provide the temperature field $T(x, y, z, t)$. We don't know the temperature of a particle as a function of time unless the location of the particle is known as a function of time.
- *Lagrangian approach*: thermometer is attached to a particle A and records the temperature. So, we obtain the particle's temperature $T_A(t)$ as a function of time. We can attach more thermometers to particles and track $T(t)$ for all of them. If position of each particle as a function of time is available, it is possible to translate Lagrange information into Euler information.

2.3 The material derivative

Consider a fluid particle moving along a trajectory (figure 2.2) and its velocity \mathbf{V}_A as a function of time t and location $\mathbf{r}_A = (x_A, y_A, z_A)$:

$$\mathbf{V}_A = \mathbf{V}_A(\mathbf{r}_A, t) = \mathbf{V}_A[x_A(t), y_A(t), z_A(t), t] \quad (2.1)$$

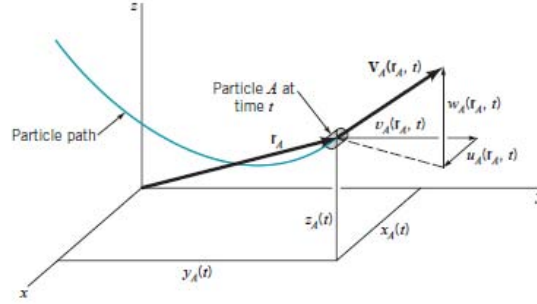


Figure 2.2: Velocity and position of particle A at time t [41].

The acceleration of particle A , denoted \mathbf{a}_A , is a function of time and location as well as the velocity and can be found as follows:

$$\mathbf{a}_A(t) = \frac{d\mathbf{V}_A}{dt} = \frac{\partial\mathbf{V}_A}{\partial t} + \frac{\partial\mathbf{V}_A}{\partial x} \frac{dx_A}{dt} + \frac{\partial\mathbf{V}_A}{\partial y} \frac{dy_A}{dt} + \frac{\partial\mathbf{V}_A}{\partial z} \frac{dz_A}{dt} \quad (2.2)$$

$$\mathbf{a}_A(t) = \frac{d\mathbf{V}_A}{dt} = \frac{\partial\mathbf{V}_A}{\partial t} + u_A \frac{\partial\mathbf{V}_A}{\partial x} + v_A \frac{\partial\mathbf{V}_A}{\partial y} + w_A \frac{\partial\mathbf{V}_A}{\partial z} \quad (2.3)$$

The expression above is valid for any particle. We can obtain the acceleration field from the velocity field as:

$$\mathbf{a}(t) = \frac{d\mathbf{u}}{dt} = \frac{\partial\mathbf{u}}{\partial t} + u \frac{\partial\mathbf{u}}{\partial x} + v \frac{\partial\mathbf{u}}{\partial y} + w \frac{\partial\mathbf{u}}{\partial z} \quad (2.4)$$

Where the scalar components a_x , a_y , and a_z can be defined as:

$$a_x = \frac{\partial u}{\partial t} + u \frac{\partial u}{\partial x} + v \frac{\partial u}{\partial y} + w \frac{\partial u}{\partial z} \quad (2.5)$$

$$a_y = \frac{\partial v}{\partial t} + u \frac{\partial v}{\partial x} + v \frac{\partial v}{\partial y} + w \frac{\partial v}{\partial z} \quad (2.6)$$

$$a_z = \frac{\partial w}{\partial t} + u \frac{\partial w}{\partial x} + v \frac{\partial w}{\partial y} + w \frac{\partial w}{\partial z} \quad (2.7)$$

Reassuming, we can write the acceleration field as follows:

$$\mathbf{a} = \frac{D\mathbf{u}}{Dt} \quad (2.8)$$

And the operator D/Dt of any quantities is given by:

$$\frac{D()}{Dt} \equiv \frac{\partial()}{\partial t} + u \frac{\partial()}{\partial x} + v \frac{\partial()}{\partial y} + w \frac{\partial()}{\partial z} \quad (2.9)$$

Usually, the shorthand notation used to indicate D/Dt is:

$$\frac{D()}{Dt} \equiv \frac{\partial()}{\partial t} + (\mathbf{u} \cdot \nabla)() \quad (2.10)$$

Where:

- $\frac{D()}{Dt}$ is called material derivative or substantial derivative or Lagrangian derivative. The material derivative describes the rate of change of some physical quantity of a fluid particle that moves with a velocity fields \mathbf{u} and can serve as a link between Eulerian and Lagrangian descriptions.
- $\frac{\partial()}{\partial t} + (\mathbf{u} \cdot \nabla)()$ is called Eulerian derivative. The Eulerian derivative is the sum of a partial time derivative and a partial spatial derivative. If we consider the velocity as variable, the first derivative represents the local acceleration while the second derivative represents the convective acceleration.

2.4 Navier-Stokes equations

In this section the Navier-Stokes equations will be defined. Some fundamental laws of physics, namely, conservation of mass, Newton's second law of motion, and the first and second laws of thermodynamics, will consider to determinate the Navier-Stokes equations.

Conservation of mass (or continuity equation) allows to control how much enters and leaves a control volume.

Newton's second law of motion says that forces can result from or cause changes in a flowing fluid's velocity magnitude and/or direction, and moment of force can result from or cause changes in a flowing fluid's moment of velocity. These forces and torques can be associated with work and power transfer.

The first law of thermodynamics is a statement of conservation of energy. The second law of thermodynamics identifies the loss of energy associated with every process.

2.4.1 Continuity equation

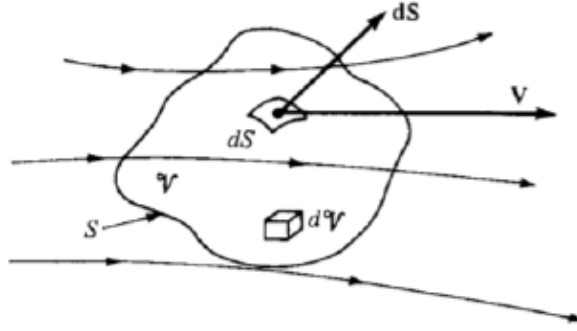
Consider a control volume V , ρ is the density, and \mathbf{u} is the velocity (figure 2.3). The mass inside the volume will be $m = \rho V$. The mass is conserved because mass can neither be created nor destroyed, its variation in a volume will be given by the amount of mass that enters or exits through its surface.

The mass flow through the surface is:

$$\Phi_\rho = \iint_S \rho \mathbf{u} \cdot \mathbf{n} dS \quad (2.11)$$

It represents the quantity of matter that enters or exits the volume. Since the mass is conserved, Φ_ρ coincides with the mass variation over time inside V given as follows:

$$\iint_S \rho \mathbf{u} \cdot \mathbf{n} dS = - \iiint_V \frac{\partial \rho}{\partial t} dV \quad (2.12)$$

Figure 2.3: Control volume V .

Using the divergence theorem, it is possible to transform the surface integrals in volume integrals:

$$\iint_S \rho \mathbf{u} \cdot \mathbf{n} dS = \iiint_V \nabla \cdot (\rho \mathbf{u}) dV \quad (2.13)$$

So, Equation (2.12) becomes:

$$\iiint_V \nabla \cdot (\rho \mathbf{u}) dV = - \iiint_V \frac{\partial \rho}{\partial t} dV \quad (2.14)$$

And moving all the terms to the left of the equal:

$$\iiint_V \left[\frac{\partial \rho}{\partial t} + \nabla \cdot (\rho \mathbf{u}) \right] dV = 0 \quad (2.15)$$

Now, for the arbitrariness of elementary volume, the differential form of the equation given below is:

$$\frac{\partial \rho}{\partial t} = - \nabla \cdot (\rho \mathbf{u}) \quad (2.16)$$

The equation above is the differential form of the continuity equation.

Reminding the concept of material derivative, it is possible writing the continuity equation as:

$$\frac{D\rho}{Dt} = -\rho \nabla \cdot \mathbf{u} \quad (2.17)$$

2.4.2 Newton's second law (momentum equation)

Consider a control volume V , ρ is the density, and \mathbf{u} is the velocity (figure 2.3). The Newton's second law of motion for a system is:

$$m\mathbf{a} = \mathbf{F} \quad (2.18)$$

where \mathbf{F} is the sum of external forces acting on the system. These forces involved are body and surface forces that act on what is contained in the control volume. The only body force considered is the one associated with the action of gravity. The surface forces taken into account are the pressure force and friction force.

The time rate of change of the linear momentum of the system is:

$$\frac{d}{dt}(m\mathbf{u}) = \mathbf{F} - \Phi_{\rho\mathbf{u}} \quad (2.19)$$

Where:

- $\frac{d}{dt}(m\mathbf{u}) = \frac{d}{dt} \iiint_V \rho \mathbf{u} dV$ is the linear momentum inside the control volume.
- $\mathbf{F} = \mathbf{F}_B + \mathbf{F}_S$ is the sum of external forces acting on the system. These are body forces and surface forces.

The body force is:

$$\mathbf{F}_B = \iiint_V \rho \mathbf{f} dV \quad (2.20)$$

Where \mathbf{f} is a unit mass force. From a dimensional point of view, it represents an acceleration.

The surface force is:

$$\mathbf{F}_S = \iint_S \mathbf{T} \cdot \mathbf{n} dS \quad (2.21)$$

Where \mathbf{T} is the tensions tensor that, for a Newtonian fluid, can be expressed as:

$$\mathbf{T} = -P\mathbf{I} + 2\mu\mathbf{E} + \lambda(\nabla \cdot \mathbf{u})\mathbf{I} \quad (2.22)$$

$$\mathbf{E} = \left(\frac{\mathbf{u} + \mathbf{u}^T}{2} \right) \quad (2.23)$$

$$\lambda = -\frac{2}{3}\mu \quad (2.24)$$

Where P is the pressure, \mathbf{I} is the identity tensor, μ is the dynamic viscosity, and λ is the volumetric viscosity. Indicating with Σ the tensor that contains the effects of viscosity given by:

$$\Sigma = 2\mu\mathbf{E} + \lambda(\nabla \cdot \mathbf{u})\mathbf{I} \quad (2.25)$$

we can rewrite \mathbf{T} as:

$$\mathbf{T} = -P\mathbf{I} + \Sigma \quad (2.26)$$

- $\Phi_{\rho\mathbf{u}} = \iint_S \rho \mathbf{u} (\mathbf{u} \cdot \mathbf{n}) dS$ is the elementary linear momentum flow that enters or exits the surface of control volume according to the normal unit vector \mathbf{n} .

So, rearranging all the terms we find:

$$\frac{d}{dt} \iiint_V \rho \mathbf{u} dV = \iiint_V \rho \mathbf{f} dV - \iint_S P(\mathbf{I} \cdot \mathbf{n}) dS + \iint_S (\Sigma \cdot \mathbf{n}) dS - \iint_S \rho \mathbf{u} (\mathbf{u} \cdot \mathbf{n}) dS \quad (2.27)$$

Using the divergence theorem, it is possible to transform the surface integrals in volume integrals:

$$\iiint_V \left[\frac{\partial}{\partial t} \rho \mathbf{u} - \rho \mathbf{f} + \nabla \cdot (P\mathbf{I}) - \nabla \cdot (\Sigma) + \nabla \cdot (\rho \mathbf{u} \mathbf{u}) \right] dV = 0 \quad (2.28)$$

Now, for the arbitrariness of elementary volume, the differential form of the equation given below is valid:

$$\frac{\partial}{\partial t} \rho \mathbf{u} - \rho \mathbf{f} + \nabla \cdot (P\mathbf{I}) - \nabla \cdot (\Sigma) + \nabla \cdot (\rho \mathbf{u} \mathbf{u}) = 0 \quad (2.29)$$

The equation above is the differential form of the momentum equation.

Reminding the concept of material derivative, it is possible writing the momentum equation as:

$$\rho \frac{D\mathbf{u}}{Dt} = \rho \mathbf{f} - \nabla \cdot P + \nabla \cdot (\boldsymbol{\Sigma}) \quad (2.30)$$

2.4.3 Energy equation

The first law of thermodynamics for a given system says that the time rate of increase of the total stored energy of the system is equal to the net time rate of energy addition by heat transfer into the system plus the net time rate of energy addition by work transfer into the system.

So, consider a total stored energy ε_{tot} per unit mass which takes into account both the internal energy per unit mass e and the kinetic energy per unit mass $u^2/2$:

$$\varepsilon_{tot} = \rho \left(e + \frac{u^2}{2} \right) \quad (2.31)$$

The variation over time of total stored energy can be expressed as:

$$d\varepsilon_{tot} = \delta \dot{q} + \delta \dot{w} - \Phi_{\varepsilon_{tot}} \quad (2.32)$$

Where:

- $d\varepsilon_{tot} = \frac{d}{dt} \iiint_V \varepsilon_{tot} dV = \frac{d}{dt} \iiint_V \rho \left(e + \frac{u^2}{2} \right) dV$ is the variation over time of total stored energy.
- $\delta \dot{q} = \delta \dot{q}_B + \delta \dot{q}_S$ is the heat flow that enters the system. It is divided into two parts: body heat flow and surface heat flow.

The body heat flow is:

$$\delta \dot{q}_B = \iiint_V \rho Q dV \quad (2.33)$$

Where Q is the radiation heat that acts on the system.

The surface heat flow is:

$$\delta \dot{q}_S = - \iint_S \mathbf{q} \cdot \mathbf{n} dS \quad (2.34)$$

The sign “-“ is used because \mathbf{n} is outgoing and the heat that enters the system increases the heat of the system. \mathbf{q} is the conductive heat that can be expressed by the Fourier’s law as:

$$\mathbf{q} = -k \nabla T \quad (2.35)$$

Where T is the temperature, and k is the thermal conductivity coefficient.

- $\delta \dot{w} = \delta \dot{w}_B + \delta \dot{w}_S$ is the work that enters the system. It is due to body forces and surface forces.

The work done by body forces is:

$$\delta \dot{w}_B = \iiint_V \mathbf{u} \cdot \rho \mathbf{f} dV \quad (2.36)$$

The work done by surface forces is:

$$\delta \dot{w}_S = \iint_S \mathbf{u} \cdot \mathbf{T} \cdot \mathbf{n} dS \quad (2.37)$$

And considering a Newtonian fluid:

$$\delta \dot{w}_S = \iint_S \mathbf{u} \cdot (-P\mathbf{I} + \boldsymbol{\Sigma}) \cdot \mathbf{n} dS \quad (2.38)$$

So, rearranging all the terms we find:

$$\frac{d}{dt} \iiint_V \varepsilon_{tot} dV = A + B \quad (2.39)$$

$$A = \iiint_V \rho Q dV + \iiint_V \mathbf{u} \cdot \rho \mathbf{f} dV \quad (2.40)$$

$$B = - \iint_S \varepsilon_{tot} (\mathbf{u} \cdot \mathbf{n}) dS + \iint_S k T \cdot \mathbf{n} dS + \iint_S \mathbf{u} \cdot (-P\mathbf{I} + \boldsymbol{\Sigma}) \cdot \mathbf{n} dS \quad (2.41)$$

Using the divergence theorem, it is possible to transform the surface integrals in volume integrals, and for the arbitrariness of elementary volume:

$$\frac{\partial \varepsilon_{tot}}{\partial t} + \nabla \cdot [\varepsilon_{tot} \mathbf{u}] = \rho Q + \nabla \cdot [k T] + \mathbf{u} \cdot \rho \mathbf{f} - \nabla \cdot [\mathbf{u} P] + \nabla \cdot [\mathbf{u} \cdot (\boldsymbol{\Sigma})] \quad (2.42)$$

Finally, reminding the concept of material derivative, the energy equation becomes:

$$\rho \frac{D}{Dt} \left(e + \frac{u^2}{2} \right) = \rho Q + \nabla \cdot [k T] + \mathbf{u} \cdot \rho \mathbf{f} - \nabla \cdot [\mathbf{u} P] + \nabla \cdot [\mathbf{u} \cdot (\boldsymbol{\Sigma})] \quad (2.43)$$

The equation above is the differential form of the energy equation.

2.4.4 Compressible Navier-Stokes equations

The continuity, momentum, and energy equations defined a system characterized by 5 unknowns in 5 differential equations:

$$\begin{cases} \frac{D\rho}{Dt} = -\rho \nabla \cdot \mathbf{u} \\ \rho \frac{D\mathbf{u}}{Dt} = \rho \mathbf{f} - \nabla P + \nabla \cdot (\boldsymbol{\Sigma}) \\ \rho \frac{D}{Dt} \left(e + \frac{u^2}{2} \right) = \rho Q + \nabla \cdot [k T] + \mathbf{u} \cdot \rho \mathbf{f} - \nabla \cdot [\mathbf{u} P] + \nabla \cdot [\mathbf{u} \cdot (\boldsymbol{\Sigma})] \end{cases} \quad (2.44)$$

Where:

$$e = \frac{R}{\gamma - 1} T \quad (2.45)$$

$$P = \rho R T \quad (2.46)$$

$$\boldsymbol{\Sigma} = 2\mu \mathbf{E} - \frac{2}{3}\mu (\nabla \cdot \mathbf{u}) \mathbf{I} \quad (2.47)$$

$$\mathbf{E} = \left(\frac{\mathbf{u} + \mathbf{u}^T}{2} \right) \quad (2.48)$$

The 5 unknowns are the three components of velocity vector \mathbf{u} , the density ρ , and the temperature T of fluid flow.

These equations are complex and analytic solutions are available only with some simplifications.

2.4.5 Incompressible Navier-Stokes equations

Assume a constant density and a constant dynamic viscosity. We can rewrite the continuity equation and momentum equation as follows:

- *Continuity equation*

Consider the index form equation:

$$\frac{\partial \rho}{\partial t} + \frac{\partial(\rho u_j)}{\partial x_j} = 0 \quad (2.49)$$

If ρ is constant:

$$\underbrace{\frac{\partial \rho}{\partial t}}_{=0} + \rho \frac{\partial u_j}{\partial x_j} = 0 = \frac{\partial u_j}{\partial x_j} = 0 \quad (2.50)$$

Finally, the continuity equation becomes:

$$\nabla \cdot \mathbf{u} = 0 \quad (2.51)$$

- *Momentum equation*

Consider the index form equation (assuming that $\mathbf{f} = 0$ for simplicity):

$$\rho \frac{\partial u_i}{\partial t} + \rho u_j \frac{\partial u_i}{\partial x_j} = - \frac{\partial P}{\partial x_i} + \frac{\partial}{\partial x_j} \left\{ 2\mu \left[\frac{1}{2} \left(\frac{\partial u_i}{\partial x_j} + \frac{\partial u_j}{\partial x_i} \right) \right] - \underbrace{\frac{2}{3}\mu \frac{\partial u_k}{\partial x_k} \delta_{ij}}_{=0(\text{continuity})} \right\} \quad (2.52)$$

If ρ and μ are constant:

$$\rho \frac{\partial u_i}{\partial t} + \rho u_j \frac{\partial u_i}{\partial x_j} = - \frac{\partial P}{\partial x_i} + \mu \frac{\partial^2 u_i}{\partial x_j \partial x_j} + \underbrace{\mu \frac{\partial}{\partial x_j} \left(\frac{\partial u_j}{\partial x_i} \right)}_{=\mu \frac{\partial}{\partial x_i} \left(\frac{\partial u_j}{\partial x_j} \right) = 0} \quad (2.53)$$

Finally, the momentum equation becomes:

$$\rho \frac{D\mathbf{u}}{Dt} = - \nabla P + \mu \nabla^2 \mathbf{u} \quad (2.54)$$

Reassuming, we obtain a system characterized by 4 unknowns (3 components of velocity and pressure):

$$\begin{cases} \nabla \cdot \mathbf{u} = 0 \\ \rho \frac{D\mathbf{u}}{Dt} = - \nabla P + \mu \nabla^2 \mathbf{u} \end{cases} \quad (2.55)$$

So, for a fluid with a constant density, we don't need more equations because the system above is no longer a thermodynamic system, but it is a mechanical system. This

means that the pressure no longer responds to the state equation $P = \rho RT$. Applying the divergence operator at momentum equation it is possible to find an equation for pressure when the fluid is incompressible:

$$\frac{\partial}{\partial x_i} \left\{ \rho \frac{\partial u_i}{\partial t} + \rho u_j \frac{\partial u_i}{\partial x_j} \right\} = \frac{\partial}{\partial x_i} \left\{ -\frac{\partial P}{\partial x_i} + \mu \frac{\partial^2 u_i}{\partial x_j \partial x_j} + \mu \frac{\partial}{\partial x_j} \left(\frac{\partial u_j}{\partial x_i} \right) \right\} = \quad (2.56)$$

$$= \underbrace{\rho \frac{\partial}{\partial t} \left(\frac{\partial u_i}{\partial x_i} \right)}_{=0(\text{continuity})} + \frac{\partial}{\partial x_i} \left(\rho u_j \frac{\partial u_i}{\partial x_j} \right) = -\frac{\partial^2 P}{\partial x_i \partial x_i} + \underbrace{\mu \frac{\partial^2}{\partial x_j \partial x_j} \frac{\partial u_i}{\partial x_i}}_{=0(\text{continuity})} \quad (2.57)$$

So, finally we obtain:

$$\nabla^2 P = - \nabla \cdot (\rho \mathbf{u} \cdot \mathbf{u}) \quad (2.58)$$

2.4.6 Dimensionless Navier-Stokes equations

Try to write the Navier-Stokes equations in dimensionless form. We will see it is common because these dimensionless equations depend on only the Reynolds number Re .

In order to find the dimensionless Navier-Stokes equations we consider some characteristic quantities:

- Characteristic velocity of system U_O
- Characteristic length of system L_O
- Characteristic time of system $T_O = \frac{L_O}{U_O}$
- Characteristic pressure of system $P_O = \rho_O U_O^2$
- Characteristic density of system ρ_O

Indicating with $()^*$ the dimensionless generic quantity, we can write:

$$\mathbf{u} = U_O \mathbf{u}^* \quad (2.59)$$

$$x_i = L_O x_i^* \quad (2.60)$$

$$t = T_O t^* = \frac{L_O}{U_O} t^* \quad (2.61)$$

$$P = P_O P^* = \rho_O U_O^2 P^* \quad (2.62)$$

Now, replacing these dimensionless parameters into the Navier-Stokes equations we can find the dimensionless Navier-Stokes equations as follows:

- *Continuity equation*

$$\begin{aligned} \nabla \cdot \mathbf{u} = 0 &= \frac{\partial u_i}{\partial x_i} = 0 \\ \frac{1}{L_O} \frac{\partial (U_O u_i^*)}{\partial x_i^*} = 0 &= \frac{\partial u_i^*}{\partial x_i^*} = 0 \\ &= \nabla^* \cdot \mathbf{u}^* = 0 \end{aligned} \quad (2.63)$$

• *Momentum equation*

$$\begin{aligned}
\rho \frac{D\mathbf{u}}{Dt} &= -P + \mu \nabla^2 \mathbf{u} = \rho \frac{\partial u_i}{\partial t} + \rho u_j \frac{\partial u_i}{\partial x_j} = -\frac{\partial P}{\partial x_i} + \mu \frac{\partial^2 u_i}{\partial x_j \partial x_j} \\
&= \rho \frac{U_O}{L_O} \frac{\partial (U_O u_i^*)}{\partial t^*} + \rho \frac{U_O}{L_O} u_j^* \frac{\partial (U_O u_i^*)}{\partial x_j^*} = -\frac{1}{L_O} \frac{\partial (\rho U_O^2 P^*)}{\partial x_i^*} + \frac{\mu}{L_O^2} \frac{\partial^2 (U_O u_i^*)}{\partial x_j^* \partial x_j^*} \\
&= \rho \frac{U_O^2}{L_O} \left[\frac{\partial u_i^*}{\partial t^*} + u_j^* \frac{\partial u_i^*}{\partial x_j^*} \right] = \rho \frac{U_O^2}{L_O} \left(-\frac{\partial P^*}{\partial x_i^*} \right) + \mu \frac{U_O}{L_O^2} \left(\frac{\partial^2 u_i^*}{\partial x_j^* \partial x_j^*} \right) \\
&= \left[\frac{\partial u_i^*}{\partial t^*} + u_j^* \frac{\partial u_i^*}{\partial x_j^*} \right] = -\frac{\partial P^*}{\partial x_i^*} + \frac{\mu}{L_O U_O \rho_O} \left(\frac{\partial^2 u_i^*}{\partial x_j^* \partial x_j^*} \right) \\
&= \left[\frac{\partial u_i^*}{\partial t^*} + u_j^* \frac{\partial u_i^*}{\partial x_j^*} \right] = -\frac{\partial P^*}{\partial x_i^*} + \frac{1}{Re} \left(\frac{\partial^2 u_i^*}{\partial x_j^* \partial x_j^*} \right) \\
&= \frac{D^* \mathbf{u}^*}{Dt^*} = -P^* + \frac{1}{Re} \nabla^{*2} \mathbf{u}^* \tag{2.64}
\end{aligned}$$

Reassuming, the system of dimensionless equations becomes:

$$\begin{cases} \nabla^* \cdot \mathbf{u}^* = 0 \\ \frac{D^* \mathbf{u}^*}{Dt^*} = -P^* + \frac{1}{Re} \nabla^{*2} \mathbf{u}^* \end{cases} \tag{2.65}$$

Where:

$$Re = \frac{U_O L_O}{\nu} \tag{2.66}$$

$$\nu = \frac{\mu}{\rho_O} \tag{2.67}$$

Using this system of dimensionless equations is convenient because different cases characterized by different dimensions, velocities, or kinds of fluid, are identical if properly rescaled. All dynamics with the same boundary conditions (properly rescaled) depends on only the Reynolds number.

Example: consider these two cases:

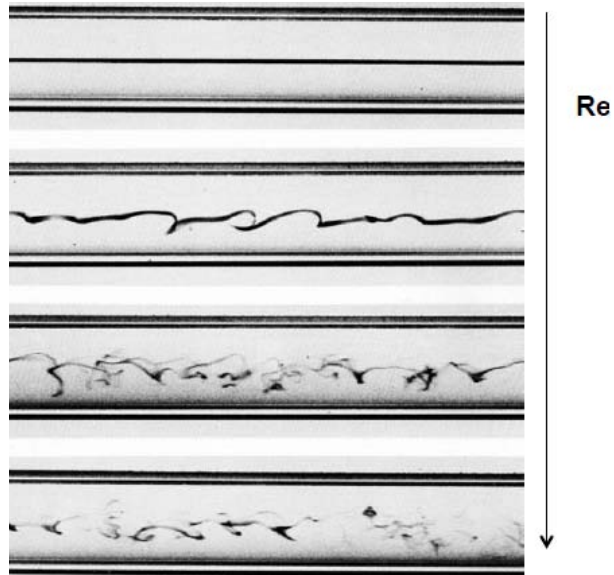
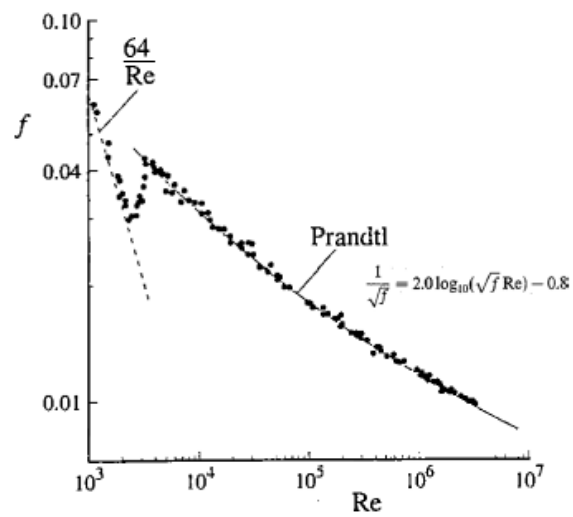
- Case 1: Air ($\nu = 10^{-5} m^2 s^{-1}$), $U = 0.1 m s^{-1}$, $L = 1 m$, $Re = 10^5$
- Case 2: Water ($\nu = 10^{-6} m^2 s^{-1}$), $U = 1.0 m s^{-1}$, $L = 0.01 m$, $Re = 10^5$

As seen the Re is the same for both cases. This means that the dimensionless solution is the same.

The Reynolds number indicates the ratio between the inertial forces (due to accelerations) and viscous forces (due to friction). Higher is the Reynolds number and higher the inertial forces are, while lower is the Reynolds number and higher the viscous forces are.

Figure 2.4 shows the behaviour of fluid with a colouring substance with increasing values of Re . We can see the differences between a laminar flow (when Re is low) and turbulent flow (when Re is high).

As seen in figure 2.5, before a certain value of Reynolds number (also called critical Reynolds number Re_{cri}) the friction factor decreases linearly with Re and the flow

Figure 2.4: Kinds of flow relate to Re .Figure 2.5: Friction factor versus Re .

is laminar. In correspondence of Re_{cri} the friction factor increases rapidly and then decreases but no linearly with Re . This increment of resistance is due to the formation of a chaotic multiscale regime in which the flow is made up many twisted vortexes. This regime is called turbulence.

2.5 Transport of chemical species

In this section the transport equation of chemical species will be treated. Consider the control volume V visible in figure 2.3. Consider a mixture of different chemical species inside a fluid flow. We indicate with:

- ρY_a the mass density of specie a;
- Y_a the mass fraction of specie a;
- \mathbf{V}_a the velocity of specie a;
- S_a the source/sink term of specie a.

The mass flow of specie a through the surface is:

$$\Phi_a = \iint_S \rho Y_a \mathbf{V}_a \cdot \mathbf{n} dS \quad (2.68)$$

Reminding the divergence theorem, we can write:

$$\Phi_a = \iiint_V \nabla \cdot (\rho Y_a \mathbf{V}_a) dV \quad (2.69)$$

The variation over time of the mass density of specie a is given by the opposite of sum of mass flows through the surface and the quantity products by the source term by means of chemical reactions as follows:

$$\frac{\partial(\rho Y_a)}{\partial t} + \nabla \cdot (\rho Y_a \mathbf{V}_a) = \rho S_a \quad (2.70)$$

If ρ is constant the equation above becomes:

$$\frac{\partial Y_a}{\partial t} + \nabla \cdot (Y_a \mathbf{V}_a) = S_a \quad (2.71)$$

The absolute velocity of specie a \mathbf{V}_a can be decomposed into the total fluid velocity \mathbf{u} and fluctuation \mathbf{v}_a :

$$\mathbf{V}_a = \mathbf{u} + \mathbf{v}_a \quad (2.72)$$

It is worth nothing that:

$$\sum_a Y_a \mathbf{V}_a = \mathbf{u} \quad (2.73)$$

$$\sum_a Y_a \mathbf{v}_a = 0 \quad (2.74)$$

So, the transport equation of chemical specie can be expressed as:

$$\frac{\partial Y_a}{\partial t} + \nabla \cdot (Y_a \mathbf{u}) + \nabla \cdot (Y_a \mathbf{v}_a) = S_a \quad (2.75)$$

Where:

- $\frac{\partial Y_a}{\partial t}$ is the variation over time of mass fraction.
- $\mathbf{u} \cdot (Y_a \mathbf{u})$ is the convective flow.
- $\nabla \cdot (Y_a \mathbf{v}_a)$ is the diffusive flow.
- S_a is the chemical source.

If there are only two chemical species, or a specie is in excess, the diffusion velocity of specie a in b is equal to the diffusion velocity of specie b in a . This velocity is opposed to the concentration gradient:

$$\mathbf{v}_a = \mathbf{v}_b = -D_{ab} \nabla Y_a = -D_{ba} \nabla Y_b \quad (2.76)$$

Replacing this velocity into the transport equation we find:

$$\frac{\partial Y_a}{\partial t} + \mathbf{u} \cdot \nabla Y_a = -\nabla \cdot (D_{ab} \nabla Y_a) + S_a \quad (2.77)$$

And considering a diffusion coefficient D constant:

$$\frac{\partial Y_a}{\partial t} + \mathbf{u} \cdot \nabla Y_a = D \nabla^2 Y_a + S_a \quad (2.78)$$

The measure unit of D is $m^2 s^{-1}$ as well as the cinematic viscosity ν . The value of D for molecules dissolved in water is about $10^{-10} m^2 s^{-1}$ while ν is about $10^{-6} m^2 s^{-1}$. The Schmidt number Sc is a dimensionless parameter which corresponds to the ratio between the cinematic viscosity and diffusion coefficient as follows:

$$Sc = \frac{\nu}{D} \quad (2.79)$$

Higher the Schmidt number and slower the molecular diffusion of species within liquids is. In our case the Sc is equal to 10^4 . This means that the molecular diffusion is really slow. In order to have an idea of how slow it is, 11 days to run across 1 cm are needed.

It is worth mentioning that when we consider a porous media, we must take into account a value of effective diffusion coefficient D_{eff} higher than the molecular diffusion coefficient D . The tortuosity of flow caused by porous structure improves the diffusion of species. The value of D_{eff} is about $10^{-6} m^2 s^{-1}$, so the Schmidt number is one order. Low Schmidt number indicates low drag and high dispersion. This means better porous media performances.

Now, it is convenient to find the dimensionless form of the transport equation. The procedure is the same as previously seen for the dimensionless Navier-Stoke equations. The dimensionless transport equation is:

$$\frac{\partial Y_a}{\partial t} + \mathbf{u} \cdot \nabla Y_a = \frac{1}{Pe} \nabla^2 Y_a \quad (2.80)$$

Where Pe is the Peclet number. It represents the ratio between convective transport phenomena and diffusion transport phenomena:

$$Pe = \frac{U_0 L_0}{D} = \frac{U_0 L_0}{\nu} \frac{\nu}{D} = Re Sc \quad (2.81)$$

Finally, the dimensionless equation becomes:

$$\frac{\partial Y_a}{\partial t} + \mathbf{u} \cdot \nabla Y_a = \frac{1}{Re Sc} \nabla^2 Y_a \quad (2.82)$$

Where:

- $\mathbf{u} \cdot \nabla Y_a$ is the convective flow.
- $\frac{1}{ReSc} \nabla^2 Y_a$ is the diffusive flow.

If the flow is laminar the mixing is slow, while if the flow is turbulent the mixing is higher. Even if the flow is not turbulent, it is possible to increase the mixing velocity by means of macroscopic motions. For example, as seen in figure 2.6, particular geometries can induce curved current lines which cause pressure gradients that lead to secondary motions that improve mixing.

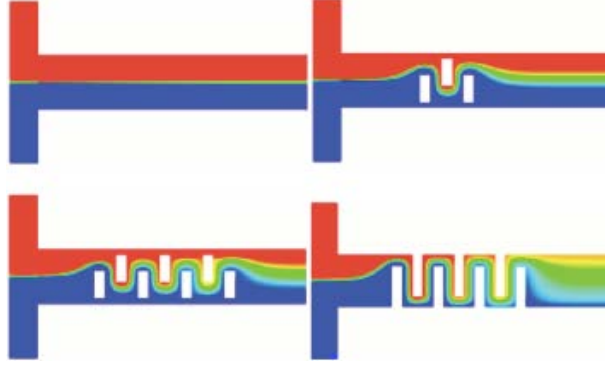


Figure 2.6: Geometries that improve fluid mixing.

Reassuming, the transport equation of chemical species is:

$$\frac{\partial Y_a}{\partial t} + \mathbf{u} \cdot \nabla Y_a = D_a \nabla^2 Y_a + S_a \quad (2.83)$$

While the dimensionless form is:

$$\frac{\partial Y_a}{\partial t} + \mathbf{u} \cdot \nabla Y_a = \frac{1}{Pe} \nabla^2 Y_a \quad (2.84)$$

Where:

$$Sc = \frac{\nu}{D} \quad (2.85)$$

$$Pe = ReSc \quad (2.86)$$

So, we can conclude saying that the scalar quantity Y_a inside a fluid which moves with a velocity \mathbf{u} is subjected to a Brownian motion. This means that Y_a is subjected to a spatial and temporal diffusion inside the flow. The Fick's law regulates this diffusion.

2.6 Flows through porous media

In this section the flows through porous media will be treated. In particular, the dimensionless Navier-Stokes equations discussed in previous sections are still valid. However, in a porous medium the geometry of the control volume border is particularly complex.

The Volume-Averaged Navier-Stokes (VANS) equations are used to treat flows through porous media. This approach is used because it requires less computational

power than the direct simulation (DNS). Indeed, a direct simulation of a complex porous medium could not be possible because present computers are not powerful enough. In order to solve the VANS equations, closure models for the drag force and subfilter-scale stress are needed.

Now, the derivation of VANS equations is given. Consider a flow in a rigid porous medium of figure 2.7, where β -phase is the fluid phase, and σ -phase is the solid phase. We indicate with \mathbf{u} the velocity of β -phase.

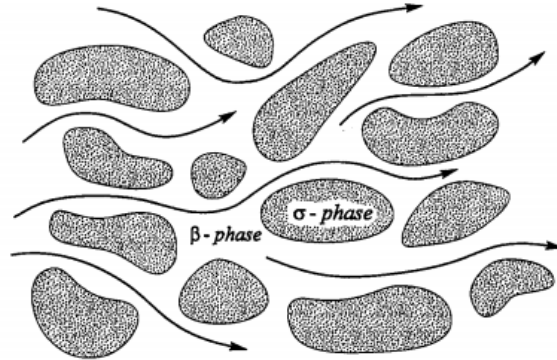


Figure 2.7: Flow in a rigid porous medium [45].

We indicate with ε the porosity of porous medium, namely the volume fraction of the β -phase defined as:

$$\varepsilon = \frac{V_\beta}{V} = 1 - \frac{V_\sigma}{V} \quad (2.87)$$

Where V is the total averaging volume, V_β is the empty volume occupied by fluid, and V_σ is the volume occupied by solid. The porosity depends on the considered volume. In a point of space, ε varies from 0 to 1. It is equal to 1 when the volume is completely occupied by empty space, and it is equal to 0 when the volume is completely occupied by solid. If we consider an average volume sufficiently large, the porosity is homogeneous enough.

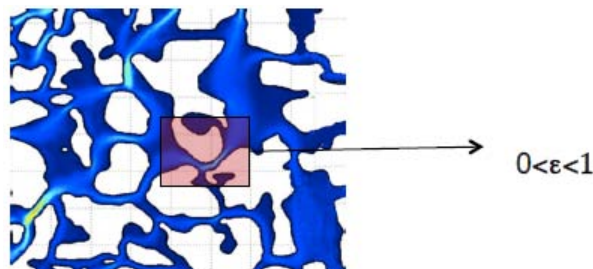


Figure 2.8: Porous structure.

Now, consider the superficial volume-averaged velocity at position \mathbf{x} :

$$\mathbf{u}_x^s = \frac{1}{V} \iiint_{V_\beta} \mathbf{u} dV \quad (2.88)$$

Where $\bar{\cdot}^s$ denotes the superficial volume averaged, \mathbf{x} is the spatial point when the volume average is evaluated, and $\mathbf{y} = \mathbf{r} - \mathbf{x}$ is the position vector relative to the centroid \mathbf{x} of the averaging volume V (figure 2.9).

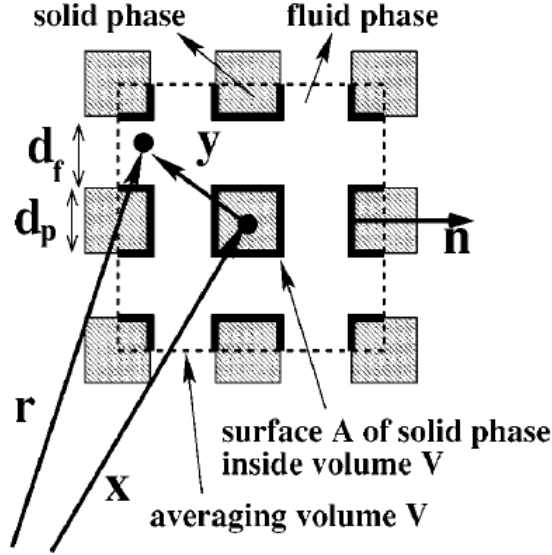


Figure 2.9: Averaging volume V [44].

The intrinsic volume-averaged velocity at position \mathbf{x} can be found as:

$$\mathbf{u}_{\mathbf{x}}^i = \frac{1}{V_\beta} \iiint_{V_\beta} \mathbf{u} dV \quad (2.89)$$

The relation between the superficial and intrinsic volume-averaged velocity is:

$$\mathbf{u}_{\mathbf{x}}^s = \varepsilon \mathbf{u}_{\mathbf{x}}^i \quad (2.90)$$

Now, for deriving the VANS equations, it is necessary to relate the volume average of a spatial derivative to the spatial derivative of a volume average by means of the spatial-averaging theorem. For example, the volume average of the gradient of the pressure and the velocity \mathbf{u} are respectively:

$$P_{\mathbf{x}}^s = P_{\mathbf{x}}^s + \frac{1}{V} \iint_{\partial V_\beta} \mathbf{n} u dA \quad (2.91)$$

$$\mathbf{u}_{\mathbf{x}}^s = \mathbf{u}_{\mathbf{x}}^s + \frac{1}{V} \iint_{\partial V_\beta} \mathbf{n} \mathbf{u} dA \quad (2.92)$$

Where A is the contact area between the fluid and the solid phase inside the averaging volume V , and \mathbf{n} is the normal unit vector at A that points from the fluid into the solid phase (figure 2.9).

In order to obtain the VANS equations, we have to apply the volume-averaging operator $\bar{\cdot}^s$ and the spatial-averaging theorem to the Navier-Stokes equations for a Newtonian and incompressible flow through a rigid porous medium as follows:

- *Continuity equation*

The superficial average of the continuity equation can be expressed as:

$$\frac{1}{V} \iiint_{V_\beta} \nabla \cdot \mathbf{u} dV = \nabla \cdot \mathbf{u}^s = 0 \quad (2.93)$$

Now, using the averaging theorem discussed above, the equation becomes:

$$\nabla \cdot \mathbf{u}^s = \nabla \cdot \mathbf{u}^s + \frac{1}{V} \iint_{\partial V_\beta} \mathbf{n} \cdot \mathbf{u} dA = 0 \quad (2.94)$$

Since the solid phase is impermeable, the final form of continuity equation is:

$$\nabla \cdot \mathbf{u}^s = 0 \quad (2.95)$$

- *Momentum equation*

The superficial average of the momentum equation can be expressed as:

$$\left\langle \rho \frac{\partial \mathbf{u}}{\partial t} \right\rangle^s + \rho \nabla \cdot \mathbf{u}^s = - \nabla P^s + \mu \nabla^2 \mathbf{u}^s \quad (2.96)$$

Considering a incompressible flow and a constant μ we can write:

$$\left\langle \frac{\partial \mathbf{u}}{\partial t} \right\rangle^s + \nabla \cdot (\mathbf{u}\mathbf{u})^s = - \frac{1}{\rho} \nabla P^s + \nu \nabla^2 \mathbf{u}^s \quad (2.97)$$

Since the volume of the β -phase contained inside the averaging volume is independent of time, we can defined the first term as follows:

$$\left\langle \frac{\partial \mathbf{u}}{\partial t} \right\rangle^s = \frac{1}{V} \iiint_{V_\beta} \frac{\partial \mathbf{u}}{\partial t} dV = \frac{\partial}{\partial t} \left\{ \frac{1}{V} \iiint_{V_\beta} \mathbf{u} dV \right\} = \frac{\partial \mathbf{u}^s}{\partial t} \quad (2.98)$$

Now, we can use the averaging theorem to express the convective term as follows:

$$\nabla \cdot (\mathbf{u}\mathbf{u})^s = \nabla \cdot \mathbf{u}\mathbf{u}^s + \frac{1}{V} \iint_{\partial V_\beta} \mathbf{n} \cdot (\mathbf{u}\mathbf{u}) dA \quad (2.99)$$

Since the solid phase is impermeable, it becomes:

$$\nabla \cdot (\mathbf{u}\mathbf{u})^s = \nabla \cdot \mathbf{u}\mathbf{u}^s \quad (2.100)$$

To eliminate the average of a product, we make use of the velocity decomposition given by Gray (1975):

$$\mathbf{u} = \mathbf{u} + \tilde{\mathbf{u}} \quad (2.101)$$

Where $\tilde{\mathbf{u}}$ is the subfilter-scale velocity. The convective inertial term becomes:

$$\mathbf{u}\mathbf{u}^s = \mathbf{u} \mathbf{u}^s + \mathbf{u} \tilde{\mathbf{u}}^s + \tilde{\mathbf{u}} \mathbf{u}^s + \tilde{\mathbf{u}}\tilde{\mathbf{u}}^s \quad (2.102)$$

If we neglect the variation of average quantities within the averaging volume, the Equation (2.102) takes the form:

$$\mathbf{u}\mathbf{u}^s = \mathbf{u} \mathbf{u}^s + \mathbf{u} \tilde{\mathbf{u}}^s + \tilde{\mathbf{u}}^s \mathbf{u} + \tilde{\mathbf{u}}\tilde{\mathbf{u}}^s \quad (2.103)$$

If we indicate with l_β the characteristic length for the β -phase, r_0 the radius of the averaging volume, and L the generic length-scale associated with averaged quantities, the simplification (2.103) requires that:

$$l_\beta \ll r_0, \quad r_0^2 \ll L^2 \quad (2.104)$$

This means to set the superficial average of the subfilter-scale velocity equal to zero:

$$\tilde{\mathbf{u}}^s = 0 \quad (2.105)$$

Under these circumstances and use $1 = \varepsilon$, Equation (2.103) becomes:

$$\mathbf{u}\mathbf{u}^s = \varepsilon \mathbf{u} \mathbf{u} + \tilde{\mathbf{u}}\tilde{\mathbf{u}}^s \quad (2.106)$$

And considering the relation (2.90):

$$\mathbf{u}\mathbf{u}^s = \frac{\mathbf{u}^s \mathbf{u}^s}{\varepsilon} + \tilde{\mathbf{u}}\tilde{\mathbf{u}}^s \quad (2.107)$$

Replacing the Equations (2.98) and (2.107) into Equation (2.97) we can find:

$$\frac{\partial \mathbf{u}^s}{\partial t} + \cdot \left[\frac{\mathbf{u}^s \mathbf{u}^s}{\varepsilon} \right] + \cdot \tilde{\mathbf{u}}\tilde{\mathbf{u}}^s = -\frac{1}{\rho} P^s + \nu \nabla^2 \mathbf{u}^s \quad (2.108)$$

The right-hand side of Equation (2.108) has been analyzed in detail by Whitaker and Quintard as follows:

$$\begin{aligned} & -\frac{1}{\rho} P^s + \nu \nabla^2 \mathbf{u}^s = \\ & -\frac{1}{\rho} P^s + \nu \left(\nabla^2 \mathbf{u}^s + \varepsilon \cdot \left[\frac{\mathbf{u}^s}{\varepsilon} + \frac{\mathbf{u}^s}{\varepsilon} \nabla^2 \varepsilon \right] \right) + \iint_{\partial V_\beta} \mathbf{n} \cdot \left[-\mathbf{I} \frac{\tilde{P}}{\rho} + \nu \tilde{\mathbf{u}} \right] dA \end{aligned} \quad (2.109)$$

If we consider regions where the terms ε and $\nabla^2 \varepsilon$ can be neglected, the final form of momentum equation is:

$$\begin{aligned} & \frac{\partial \mathbf{u}^s}{\partial t} + \cdot \left[\frac{\mathbf{u}^s \mathbf{u}^s}{\varepsilon} \right] + \cdot \tilde{\mathbf{u}}\tilde{\mathbf{u}}^s = \\ & -\frac{1}{\rho} P^s + \nu \nabla^2 \mathbf{u}^s + \iint_{\partial V_\beta} \mathbf{n} \cdot \left[-\mathbf{I} \frac{\tilde{P}}{\rho} + \nu \tilde{\mathbf{u}} \right] dA \end{aligned} \quad (2.110)$$

If we consider a flow through a homogeneous porous medium, namely with a constant value of porosity, characterized by small, stationary, and homogeneous velocities, the momentum equation becomes:

$$\begin{aligned} & \underbrace{\frac{\partial \mathbf{u}^s}{\partial t}}_{=0} + \underbrace{\cdot \left[\frac{\mathbf{u}^s \mathbf{u}^s}{\varepsilon} \right]}_{=0} + \underbrace{\cdot \tilde{\mathbf{u}}\tilde{\mathbf{u}}^s}_{=0} = \\ & -\frac{1}{\rho} P^s + \nu \underbrace{\nabla^2 \mathbf{u}^s}_{=0} + \iint_{\partial V_\beta} \mathbf{n} \cdot \left[-\mathbf{I} \frac{\tilde{P}}{\rho} + \nu \tilde{\mathbf{u}} \right] dA \end{aligned} \quad (2.111)$$

If we write the surface integral using the Whitaker parametrization, the Equation (2.111) simplifies to:

$$\frac{1}{\rho} P^s = -\nu \mathbf{K}^{-1} (\mathbf{I} + \mathbf{F}) \varepsilon \mathbf{u}^s \quad (2.112)$$

Where \mathbf{K} is the permeability tensor, \mathbf{I} is the unit tensor, and \mathbf{F} is the Forchheimer tensor. The Forchheimer tensor depends on the Reynolds number. If the Reynolds number is high, and thus the inertial effects are dominant, we must consider the \mathbf{F} tensor. If the Reynolds number is low enough, and thus the inertial effects are negligible, we can set the \mathbf{F} tensor equal to zero. In this work, being the Reynolds number small, the contribution of the Forchheimer tensor has been neglected. Darcy's law follows from the Equation (2.112) as:

$$P^s = -\mu \mathbf{K}^{-1} \mathbf{u}^s \quad (2.113)$$

If the porous medium is isotropic the permeability tensor can be written as:

$$\mathbf{K} = k \mathbf{I} \quad (2.114)$$

Where k is the permeability. It depends on porosity and fibre diameter. The unit of measure of permeability is m^2 . For example, for a medium composed of cylindrical fibres it values:

$$k = \frac{d_f^2 \varepsilon^3}{K_{kc} (1 - \varepsilon)^2} \quad (2.115)$$

Where K_{kc} is the Kozeny-Carman constant and d_f is the fibre diameter.

So, the Darcy's law as given above is valid if the Reynolds number is low. As seen, it is linear because the inertial effects due to the flow accelerations have been not considered.

Using the same procedure described above, it is possible to derive an equation for the transport of chemical species. The final equation for the transport of chemical species through porous media can be expressed as:

$$\frac{Y_a}{\partial t} + \mathbf{u} \cdot \nabla Y_a = \nabla \cdot (D_{eff} \nabla Y_a) + S \quad (2.116)$$

Where Y_a is the concentration of specie a .

2.7 Fundamental hydraulics

In this section the fundamental hydraulic principles that characterize a VRFB system will be presented. The pump losses are the pressure losses due to the movement of the electrolytes in a VRFB. These losses generally consist of losses in pipes, flow frame and porous electrode. The typical electrode is made on carbon felt or carbon paper and it generates a significant resistant to electrolyte flow. A desirable flow frame design is needed to reduce the shunt currents that affect the overall coulombic efficiency. The losses due to electrode and flow frame are dominant in the total pressure losses and thus can influence the battery performance. In this work the influence of flow rate on the pump losses has been investigate. The experimental results will be presented in chapter 3 and discussed in chapter 4.

2.7.1 Head loss in pipes

The head losses in pipes consist of head losses due to viscous effects in the straight pipes called major losses and head losses due to various pipe components such as elbows, bends, valves and others called minor losses, as shown below:

$$h_L = h_{Lmajor} + h_{Lminor} \quad (2.117)$$

It is worth mentioning that “major” and “minor” do not necessarily reflect the relative importance of each type of loss. For example, for a very short pipe system with many components the minor losses may be larger than the major losses.

Major losses

The pressure drop and head loss depend on the wall shear stress, τ_{wall} , between the fluid and pipe surface. There are two kinds of flow: laminar flow and turbulent flow. A fundamental difference between laminar and turbulent flow is that the shear stress for turbulent flow is a function of the density of the fluid, ρ , while for laminar flow the shear stress is independent of the density and it is a function only of the dynamic viscosity, μ . The pressure drop for laminar pipe flow is found to be independent of the roughness of the pipe because there is no thin viscous layer. Instead, for turbulent pipe flow it is necessary to include this parameter because there is a thin viscous layer, so the pressure drop is expected to be a function of the wall roughness.

The dimensionless parameter that indicates if a flow is laminar or turbulent is the Reynolds number defined as:

$$Re = \frac{\rho U D}{\mu} \quad (2.118)$$

Where U is the average velocity, D is the characteristic length, ρ is the density and μ is the dynamic viscosity. Typically, when the Re is less than 2100 the flow is laminar, while when the Re is more than 4000 the flow is turbulent. When Re is between 2100 and 4000 the flow is in the transition range. Both for laminar and turbulent pipe flow the pressure drop should be proportional to the pipe length. The most widely used equation in fluid dynamics to express the major losses is the Darcy-Weisbach equation, valid for any fully developed, steady, incompressible pipe flow:

$$h_{Lmajor} = f \frac{L U^2}{D 2g} \quad (2.119)$$

The unit of measurement of the last equation is meter. It is possible to express the Darcy-Weisbach equation in Pascal as follows:

$$\Delta P_{Lmajor} = f \frac{L \rho U^2}{D 2} \quad (2.120)$$

Where f is the Darcy friction factor. For laminar fully developed flow, the value of f is simply:

$$f = \frac{64}{Re} \quad (2.121)$$

For turbulent fully developed flow, the value of f is dependent on the Reynolds number Re and the relative roughness $\frac{\varepsilon}{D}$:

$$f = \phi \left(Re, \frac{\varepsilon}{D} \right) \quad (2.122)$$

It is not easy to relate the friction factor to the Reynolds number and the relative roughness. The information available in literature is a result of experiment conducted by J. Nikuradse in 1933 and amplified by many others since then. Nikuradse used artificial roughened pipes made by himself by gluing sand grains onto pipe walls. The pressure drop needed to produce a certain flow rate was measured a lot of time and the data were converted into the friction factor for the corresponding Reynolds number and relative roughness. In this way it was possible to determine the function $f = \phi\left(Re, \frac{\varepsilon}{D}\right)$. However, the roughness of commercial pipes is not uniform and well defined as in the artificial pipes used by Nikuradse, but it is possible to obtain the relative roughness and thus the friction factor. For example, typical roughness values for various materials are defined in Table 2.1 [41].

The Moody chart shown in figure 2.10 correlates the data of Nikuradse in terms of the relative roughness of commercially available pipe materials. For laminar flow the friction factor is independent of relative roughness while for turbulent flow the friction factor is dependent of both the Reynolds number and relative roughness. From $Re = 2100$ to $Re = 4000$ there are not values of friction factor because in this transition range the flow may be laminar or turbulent or an unsteady mix of both depending on the specific circumstances involved. It is worth noting that for any pipe, even smooth ones (relative roughness = 0), the head loss is not zero. This is a result of the no-slip boundary condition that requires any fluid to stick to any solid surface it flows over. The Colebrook formula given below is valid for the entire nonlaminar range of the Moody chart [41]:

$$\frac{1}{f} = -2.0 \log\left(\frac{\varepsilon/D}{3.7} + \frac{2.51}{Re \sqrt{f}}\right) \quad (2.123)$$

The difficulty of this relation is the non-linearity of the friction factor that requires an iterative scheme. Another equation, easier to use, is given by [41]:

$$\frac{1}{f} = -1.8 \log\left[\left(\frac{\varepsilon/D}{3.7}\right)^{1.11} + \frac{6.9}{Re}\right] \quad (2.124)$$

Where one can solve for the friction factor explicitly.

Table 2.1: Equivalent roughness for new pipes [41].

Pipe	Equivalent roughness [mm]
Riveted steel	0.9-9.0
Concrete	0.3-3.0
Wood stave	0.18-0.9
Cast iron	0.26
Galvanized iron	0.15
Commercial steel	0.045
Drawn tubing	0.0015
Plastic, glass	0.0 (smooth)

Minor losses

Most pipe systems are characterized by additional components such as elbows, bends, valves and others that increase the overall head losses of the system. The most common

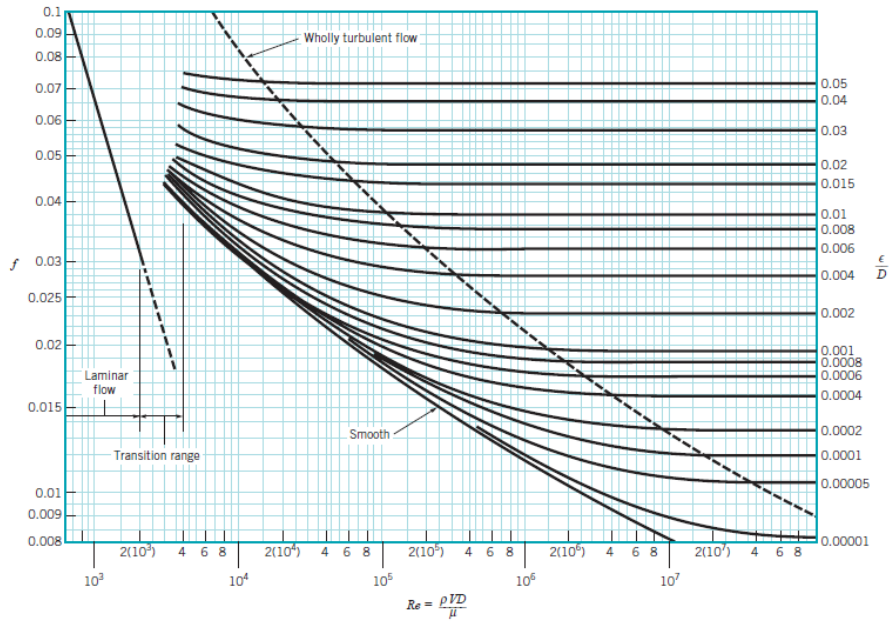


Figure 2.10: The Moody chart [41].

method used to determine these head losses or pressure drops consists of specify the loss coefficient K_L for any system component. This coefficient is strongly dependent on the geometry of the component considered and it may also depend on the fluid property, namely the Reynolds number. So, the minor head losses due to the components along the pipe are given by:

$$h_{Lminor} = K_L \frac{U^2}{2g} \quad (2.125)$$

The unit of measurement of the last equation is meter. It is possible to express this equation in Pascal as follows:

$$\Delta P_{Lminor} = K_L \frac{\rho U^2}{2} \quad (2.126)$$

Minor losses are sometimes given in terms of an equivalent length, L_{eq} . Namely, the head loss through a component is given in terms of the equivalent length of pipe that would produce the same head loss as the component. This method is shown as follows:

$$L_{eq} = K_L \frac{D}{f} \quad (2.127)$$

$$h_{Lminor} = f \frac{L_{eq}}{D} \frac{U^2}{2g} \quad (2.128)$$

Many pipe systems can be characterized by various transition sections in which the pipe diameter changes from one size to another. These pipe diameter changes may be smooth or abrupt and produce head losses. Such of these changes are now presented [41].

- The entrance of flow from a reservoir to a pipe (figure 2.11) or the exit of flow from a pipe to a reservoir (figure 2.12) are cases of pipe diameter changes that produce a head loss. It is worth noting that each geometry has an associated loss coefficient.
- A sudden contraction is another common head loss. The loss coefficient for a sudden contraction is a function of the area ratio A_2/A_1 as is shown in figure 2.13 (a).
- A sudden expansion is also a head loss and it is possible to obtain the loss coefficient by means of a simple analysis. Considering the continuity and the momentum equations it may be found the loss coefficient given by:

$$K_L = \left(1 - \frac{A_1}{A_2}\right)^2 \quad (2.129)$$

And plotted in figure 2.13 (b).

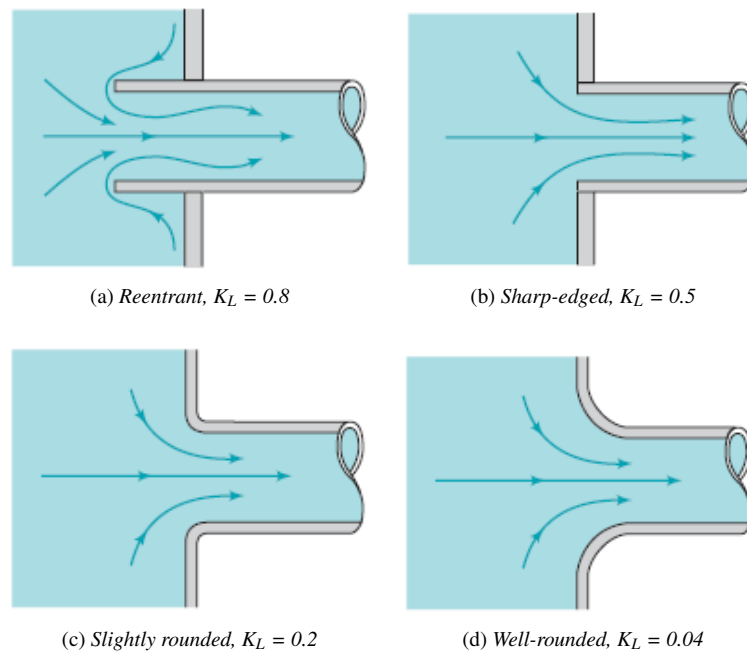


Figure 2.11: Entrance flow conditions and loss coefficient [41].

Moreover, bends in pipes produce a greater head loss than if the pipe were straight due to the separation of flow near the inside of bend and the swirling secondary flow that occurs because the curvature of the pipe centreline causes an imbalance of centripetal forces. The associated values of K_L for a 90° bend are shown in figure 2.14 [41].

Finally, components such as elbows, tees, reducers, valves, and filters can produce head losses. The values of K_L for such components depend strongly on the shape of component and weakly on the Reynolds number. Loss coefficients for pipe components are shown in Table 2.2 [41].

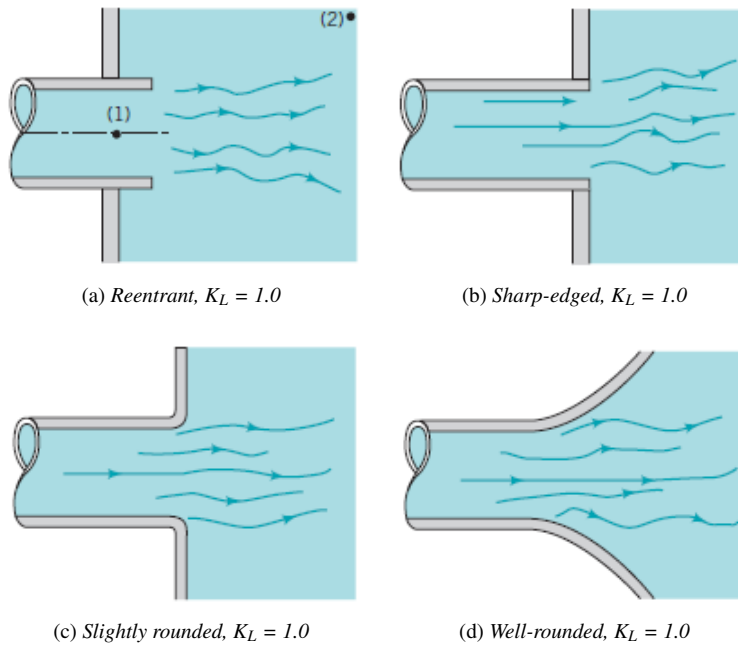


Figure 2.12: Exit flow conditions and loss coefficient [41].

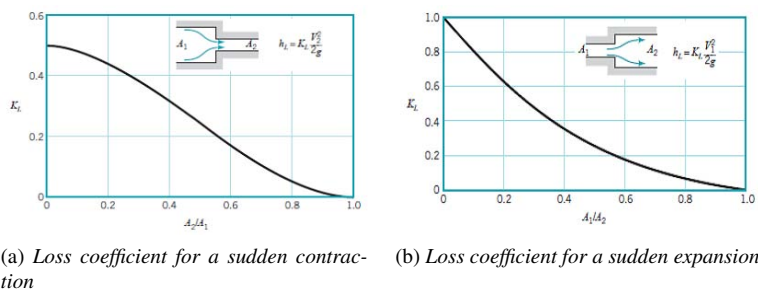


Figure 2.13: Loss coefficient for a sudden contraction and a sudden expansion [41].

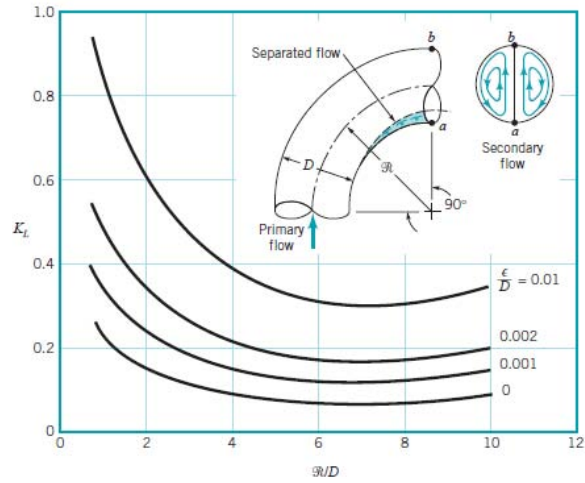













Figure 2.14: Loss coefficients of a 90° bend pipe [41].

Table 2.2: Loss coefficients for pipe components.

Component	K_L	
Elbows regular 90° flanged	0.3	
Elbows regular 90° threaded	1.5	
Elbows long radius 90° flanged	0.2	
Elbows long radius 90° threaded	0.7	
Elbows long radius 45° flanged	0.2	
Elbows regular 45° threaded	0.4	
180° return bends flanged	0.2	
180° return bends threaded	1.5	
Tees line flow flanged	0.2	
Tees line flow threaded	0.9	
Tees branch flow flanged	1.0	
Tees branch flow threaded	2.0	
Union threaded	0.08	
Valves globe fully open	10.0	
Valves angle fully open	2.0	
Valves gate fully open	0.15	
Valves gate 1/4 closed	0.26	
Valves gate 1/2 closed	2.1	
Valves gate 3/4 closed	17.0	
Valves swing check forward flow	2.0	
Valves swing check backward flow		
Valves ball fully open	0.05	
Valves ball 1/3 closed	5.5	
Valves ball 2/3 closed	210.0	

2.7.2 Pressure losses inside stack

The pressure losses inside the stack are due to the pressure drop through the porous electrodes and flow frame.

The flow frame consists of manifolds and channels that feed electrolyte into each half-cell. On the one hand flow frames characterized by long channels and manifolds with a small cross-sectional area help to reduce the shunt currents and other electrical issues, but on the other hand they produce a considerable pump loss associated to the higher pressure drop that affects the system efficiency. So, an appropriate trade-off between pump losses and flow frame design can improve the system. The pressure losses through manifolds and channels can be calculated using the Darcy-Weisbach equation.

A significant pressure drop in the reaction cell is caused by the porous electrodes. The porous electrode is a key component of the cells of the stack and it can be considered like a typical porous medium. So, the pressure drop through a given porous electrode can be determined by the Darcy's law as follows:

$$\Delta P = \frac{\mu \varepsilon L U}{K} = \frac{\mu \varepsilon L Q}{K A} \quad (2.130)$$

Where:

$$U = \frac{Q}{A} = \frac{1}{\varepsilon V} \int_V u_x dV \quad (2.131)$$

Where L is the length of the porous electrode, A is the cross-sectional area through which the electrolyte flows, K is the permeability of the porous electrode, U is the bulk intrinsic velocity of the generic cubic domain V along the streamwise direction x , μ is the dynamic viscosity, and ε is the porosity of the porous electrode. The pressure gradient $\Delta P/L$ corresponds to the applied body force. The permeability can be calculated if the pressure drop is available or can be imposed by Kozeny-Carman equation as shown below for a medium composed of cylindrical fibres:

$$K = \frac{d_f^2 \varepsilon^3}{K_{kc} (1 - \varepsilon)^2} \quad (2.132)$$

Where ε is still the porosity of the porous electrode, K_{kc} is the Kozeny-Carman constant and d_f is the fibre diameter.

2.7.3 Pump energy

The total pressure losses ΔP_{tot} are the sum of the total pressure losses in all components of the pipe system ΔP_{pipe} plus the pressure losses inside the stack ΔP_{stack} as described above:

$$\Delta P_{tot} = \Delta P_{pipe} + \Delta P_{stack} \quad (2.133)$$

The total hydraulic losses can be expressed as:

$$P_{tot} = \Delta P_{tot} Q \quad (2.134)$$

The pump power needed to circulate the electrolytes can be defined as:

$$P_{pump} = \frac{P_{tot}}{\eta} \quad (2.135)$$

Where Q is the flow rate, and η is the efficiency of the pump system generally characterized by the product of the electric motor efficiency, the inverter efficiency and finally the pump efficiency.

Chapter 3

Experimental investigation

In this chapter the Vanadium Redox Flow Battery available in the Energy Storage Lab at the University of Padua will be described. The project started in 2016 by Professor Massimo Guarnieri and co-workers is called VRFB-IS Experiment. This plant shown in figure 3.1 is characterized by an energy of 24 kWh and a design power of about 3.5 kW even if a peak of power of 9 kW has been reached. Finally, the experimental results obtained by the experimental campaign conducted will be presented. The experimental campaign has been done in order to investigate the effects of the electrolyte flow rate on the total losses that characterize the system. The losses taken into account are the internal resistance losses and the pump losses as described in previous chapters. As it will be possible to see higher is the flow rate, lower the internal resistance losses are, because the concentration overpotential is relatively small, but on the other hand the pump energy needed is higher. So, the aim of this job is to define the optimal flow rate for every currents and every state of charge that reduces the total losses and gives the maximum system efficiency. The fundamental parameter that can allow to change the flow rate at the same conditions (i.e. current and SOC) is the flow factor α defined as the ratio between the current flow rate and the stoichiometric flow rate. Thus, the flow factor is a multiplying factor applied to the minimum flow rate needed to make a complete reaction inside cell. The relation between the flow rate Q and the flow factor for charge and discharge is given as:

$$Q_{stoich} = \frac{I}{F C_v (1 - SOC)} \quad (charge) \quad (3.1)$$

$$Q_{stoich} = \frac{I}{F C_v SOC} \quad (discharge) \quad (3.2)$$

$$Q = \alpha Q_{stoich} \quad (3.3)$$

The flow factor is also a kind of safe coefficient. In particular way, during charge for high SOC it is fundamental that α is high enough in order to avoid that the applied current reacts with the cell components such us electrodes and bipolar plates. Indeed, the applied current must react only with the electrolyte because otherwise some issues and dams can occur and thus the components of the cells may damage. For example the minimum flow factor used in the VRFB of the University of Padua is 3.5.

3.1 The battery

The core of the battery is the stack. The stack available in Energy Storage Lab is composed by 40 cells electrically connected in series and feeded hydraulically in parallel. Each single cell is formed by two carbon felt electrodes and a Nafion membrane enclosed between two bipolar plate made of graphite. Above the bipolar plates are photo engraved the flow fields which distribute the flow in homogeneous mode within the electrode.

The two electrolytes are water solutions of sulfuric acid 5 M and vanadium salts 1.6 M. Anolyte and catholyte are stored in two separated tanks made of plastic with a capacity of 500 litres. The feeding system is characterized by plastic pipes and some valves which can allow to manage and control the flow of electrolytes. For example, when the battery is off it is possible to close the inlet and outlet valves of the electrolytes to the stack in order to have it full of electrolyte. Other two valves allow to close the flow rate in correspondence of the flow meters for example when a cleaning of the flow meters is needed. Another valve can put in contact the two tanks connected by a pipe. This valve can be open to restore the same volume of electrolytes inside tank. Finally, two three vie valves can permit the remixing of the electrolytes needed to eliminate the capacity losses due to the passage of vanadium ions through the membrane. Thanks to remixing the catholyte is send toward the negative tank while anolyte is send toward the positive tank. In this way it is possible to restore the vanadium species inside tanks.

Two magnetic drive pumps lead the electrolytes from tanks to stack. Once the electrolyte enters the stack and flows across the cells, then it exits from the stack and returns into the correspondent tank. It is worth mentioning that each pump is controlled by means of two inverters which allow a maximum flow rate of 29.5 litres. Each inverter is controlled by a voltage analogic input.

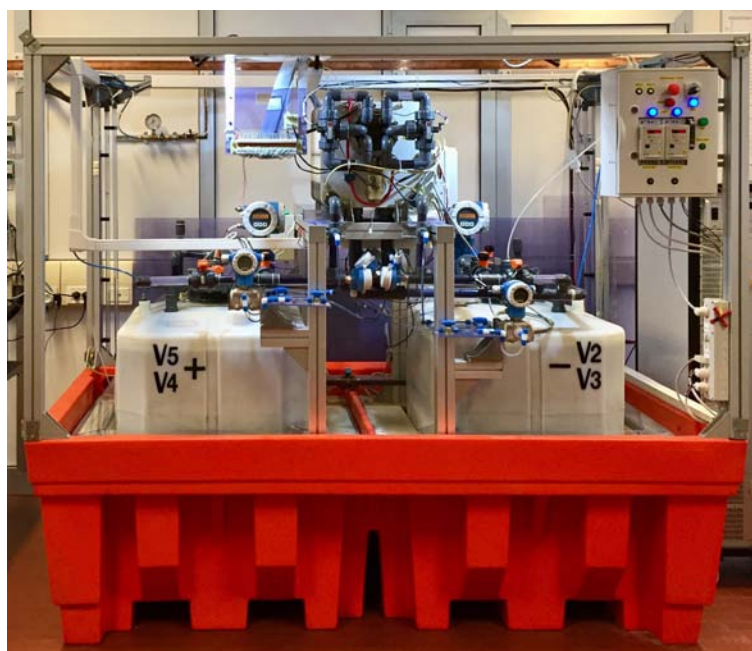


Figure 3.1: VRFB plant placed in Energy Storage Lab.

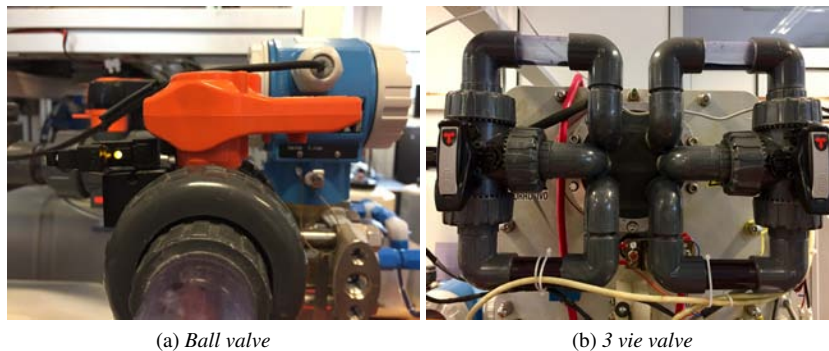


Figure 3.2: Valve system

3.2 The load

The energy needed to charge the battery or released from the battery during discharge is given or absorbed respectively by means of a Dana power supply (figure 3.3(a)). This device can release or absorb a current from 0 to 75 A. The energy produced during discharge is dissipated as heat through Joule effect because it is not possible to give it back to the grid. Moreover, a passive load composed by six resistors connected in parallel has been installed to allow discharge currents higher than 75 A. This passive load shown in figure 3.3(b) has a maximum discharge current of 600 A. It is worth mentioning that the Dana power supply can be managed by remote or local control and the current is imposed automatically by LabVIEW very accurately. While to control the current absorbed by the passive load it is necessary to regulate manually the resistance.

3.3 Acquiring and Control system

The acquiring and control system is composed by different measurement tools connected with a National Instruments compact DAQ connected with a computer where a LabVIEW program realized in the laboratory allows to control some parameters like flow rate, current, voltage exc. and moreover allows to visualize the measures done by the used transducers. In this section a short introduction to LabVIEW is given. Furthermore, an exhaustive description of the used transducers is provided. Finally, the NI modules and how they work will be treated.

3.3.1 LabVIEW

LabVIEW (Laboratory Virtual Instrumentation Engineering Workbench) is a system-design platform and development environment for a visual programming language from National Instruments [36]. The fundamental element of LabVIEW is the Virtual Instrument (VI) composed by the front panel, block diagram that contains the VI code and does the job and an icon which represents the program. The front panel is the user interface. As it is possible to see in figure 3.4, it is composed by a schematic illustration of the stack, valves and tanks. Moreover, indicators are present, and they can show the values of cells voltage, stack voltage, stack current, pumps power, OCV, electrolyte temperatures, electrolyte differential pressures, measures flow rate and state of charge measured by sensors and transducers. At the top there are the controls about



(a) Dana power supply



(b) Passive load

Figure 3.3: Load system

the power supply that allow to impose the charge or discharge current and voltage. On the right the cells voltage is available, and it is represented by green indicators. A red led turns on when the cell voltage is higher than 1.65 V. On the left there are the control panel and the flow rate control. The first one is used to control the program. There are these buttons: start program, stand-by program, exit program, program status and power switch. The second one is used to impose the flow rate of positive and negative electrolytes or the flow factor. Moreover, it is possible to change the PID (Proportional Integrative Derivative) parameters like proportional gain, integral time and derivate time to better control the flow rates. Two graphics allow to see the flow rate setpoint, the PID output (the analogic tension signal that controls the inverters) and the measured flow rates. At the bottom there are three panels: save panel, polarization curve panel and efficiency panel. The save panel allows to save every parameter measured by sensors. The polarization curve panel and the efficiency panel can automatically elaborate the polarization curves and the efficiency respectively.

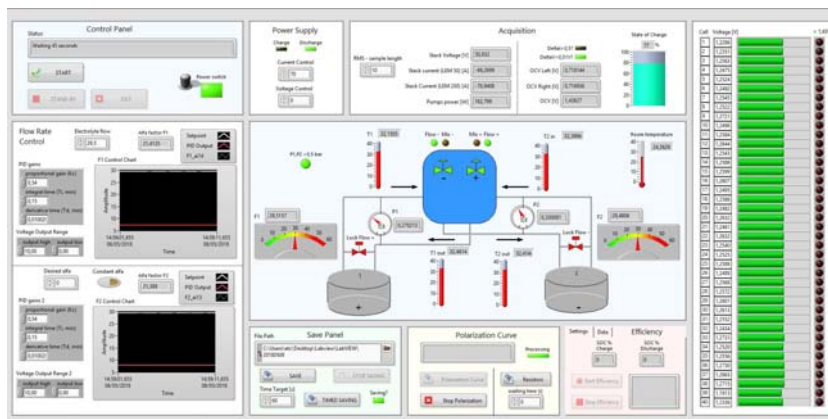


Figure 3.4: LabVIEW's front panel.

3.3.2 Transducers

The principle used transducers are flow meters, pressure meters, thermometers, current meters and a single-phase network analyzer. They are needed only for academic purposes to control some parameters like the flow rate, the electrolyte's differential pressure between inlet and outlet of the stack, the inlet and outlet temperatures of the stack and currents that enter or exit the battery during charge and discharge respectively. In a common industrial plant these meters are not necessary. Thus, these industrial systems result less complex than the system available in the Energy Storage Lab from this point of view. Anyway, the used transducers are described as follows:

- *Flow meters*: the used flow meters are Proline Promag 50 electromagnetic flow meters built by Endress+Hauser (figure 3.5(a)) able to do accurate measures of flow rate. They are based on Faraday induction law which claims that a conductor generates a tension when it moves inside a magnetic field. So, the fluid is the conductor which moves inside a constant magnetic field produced by two DC bobbins with alternate polarity. The tension induced is proportional to the flow velocity and it is measured by means of two electrodes [34]. The flow meters

have been installed between the pumps and the stack for both positive and negative electrolytes. The maximum measure error is $\pm 0.5\%$ on the instantaneous value ± 1 mm/s. These tools generate a current output from 4 mA (corresponding to a zero-flow rate) to 20 mA (corresponding to a maximum flow rate of 60 litres/minutes). This signal is brought to the compact DAQ and connected with a NI 9207 module able to do current and tension acquisitions. The alimentation is separated from the measure.

- *Pressure meters*: the used pressure meters are Deltabar S PDM75 pressure meters built by Endress+Hauser (figure 3.5(b)). The measure consists of a differential pressure between the inlet and outlet of the stack by means of a dedicated pressure line for both the positive and negative electrolytes. The output signal is a current output 0-20 mA [35] acquired by the NI 9207 module as well as the output signal of the flow meters. The alimentation is given by the measure channel.
- *Thermometers*: the used thermometers are resistance thermometers, also called resistance temperature detectors (RTDs), Pt100 where 100 Ohm is the resistance of the sensor at 0°C and Pt indicates platinum, namely the material with which is made the sensible element (figure 3.5(c)). In the system there are four RTDs that measure the inlet and outlet temperature from the stack of both the positive and negative electrolytes. Each RTD relates to a NI 9216 module by means of a four-wire connection. Two conductors are needed to measure the resistance, one serves to give the excitation current while the last is used as the ground reference of the module.
- *Single-phase network analyzer*: the used Z203 single-phase network analyzer built by Seneca is able to measure the absorbed power by the inverters needed for the functioning of the pumps. This tool is used like a wattmeter and can relay the measured active power through an analogic tension signal from 0 to 10 V. The full-scale of 10 V corresponded to a measured power of 625 W. The wattmeter is connected with a NI 9207 module and it is installed on the alimentation line of the two inverters and receives a separated alimentation.
- *Current meters*: the used current meters are the LEM HASS 50 S and the LEM HASS 200 S. The first one is used to measure currents until 75 A while the second one is used to measure currents higher than 75 A. Both current meters can measure either inlet current during the charge of the battery and outlet current during the discharge of the battery. These transducers are connected with a NI 9207 module. The measured currents are converted into an analogic tension signal by the current meters in turn measured by the Ni module.

3.3.3 National Instruments Modules

In this section the different National Instruments modules used in the measurement system are described. These modules are chosen according to the type of measure.

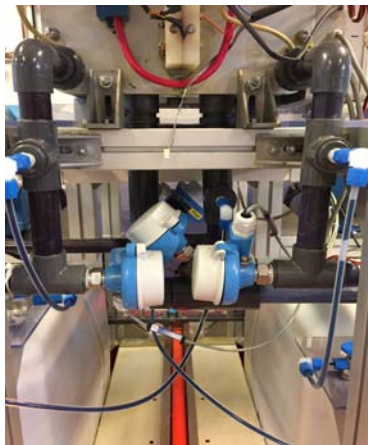
The *NI 9207 module* can read both current signals and voltage signals through current channels and voltage channels respectively. It is used to read the current analogic signals like flow rate and differential pressures and the voltage analogic signals such as stack voltage, stack current, OCV and pumps power from sensors. These signals



(a) Flow meter



(b) Pressure meter



(c) RTDs

Figure 3.5: Transducers

are scanned, amplified, conditioned and sampled by a 24-bit analogic-digital converter. The accuracy for current channels is $\pm 0.87\%$ gain error and $\pm 0.05\%$ offset error while the accuracy for voltage channels is $\pm 0.52\%$ gain error and $\pm 0.04\%$ offset error [37].

The *NI 9209 module* can read only voltage signals. It is used to read the 40 cells voltages. These signals are scanned, saved in a buffer, conditioned and then sample by a 24-bit analogic-digital converter. The accuracy of the voltage channel is $\pm 0.46\%$ gain error and $\pm 0.011\%$ offset error in the range of temperature between -40°C to 70°C . At 25°C the gain error is $\pm 0.06\%$ and the offset error is $\pm 0.003\%$ [38].

The *NI 9216 module* is specific for temperature measures. It is used to read the electrolytes temperatures from the RTDs. In this case the signals are filtered and then also in this case sample by a 24-bit analogic-digital converter. The accuracy is 0.15°C at the temperature of 25°C [39].

The *NI 9263 module* is used for control actions by means of analogic voltage outputs. These signals are send to the inverters which control the pumps engines simply changing the inverter's frequency through a signal from 0 to 10V. In this way it is possible to vary the flow rate. It is the same for current control and voltage control. Each channel is characterized by an analogic-digital converter and a protection against short-circuits and overvoltage. The accuracy is $\pm 0.35\%$ gain error and $\pm 0.75\%$ offset error in the range of temperature between -40°C to 70°C . At 25°C the gain error is $\pm 0.03\%$ and the offset error is $\pm 0.1\%$ [40].

3.4 Experimental campaign and data acquiring

The experimental campaign has been conducted as follows. First of all, the different values of flow factor, applied current and SOC have been chosen. For every value of SOC and for every value of applied current these tests have been replicated changing every time the value of flow factor. In this way it has been possible to investigate the behaviour of the battery at various SOC, applied currents and flow rates. These tests, summarized in Table 3.1, have been carried out only during discharge.

In every test the acquired data were saved for 60 seconds by LabVIEW only when the cell voltages were stable, namely when the stationary condition was reached. In particular way, LabVIEW saves automatically a sample of data every 0.8 seconds in an Excel file subdividing each measure in columns. The measures acquired by LabVIEW are the cell voltages, the stack voltage, the applied current, the open circuit voltage, the inlet and outlet temperatures and the pumps power. First of all, the media of these measures has been calculated and then interesting conclusions have been found by studying and analysing these parameters.

It is worth nothing that some experimental points are missing. In particular, in some cases it has been not possible to carry out some tests with small values of flow factor because the flow rate was too low (i.e. lower than 2.0 l/min) and in other cases it has been not possible to do some tests with large values of flow factor because the flow rate was too high (i.e. higher than 29.5 l/min). Moreover, it is worth mentioning that at $\text{SOC}=20\%$ and in some cases at very low values of flow factor (i.e. lower than 6) the cell voltages were not always in stationary conditions and this might have affected these measures.

The main results found from the experimental campaign will be treated in the next chapter.

Table 3.1: Experimental tests.

SOC [%]	Applied current [A]	Flow factor [-]
20	10	4, 6, 8, 10, 12, 14, 16, 18, 20
20	30	4, 6, 8, 10, 12
40	10	6, 8, 10, 12, 14, 16, 18, 20
40	30	4, 6, 8, 10, 12, 14, 16, 18, 20
40	50	4, 6, 8, 10, 12, 14
40	70	6, 8, 10
60	10	8, 10, 12, 14, 16, 18, 20
60	30	4, 6, 8, 10, 12, 14, 16, 18, 20
60	50	4, 6, 8, 10, 12, 14, 16, 18, 20
60	70	4, 6, 8, 10, 12, 14, 16
80	10	12, 14, 16, 18, 20
80	30	6, 8, 10, 12, 14, 16, 18, 20
80	50	4, 6, 8, 10, 12, 14, 16, 18, 20
80	70	4, 6, 8, 10, 12, 14, 16, 18, 20

3.5 Internal resistance analysis

The internal resistance has been profoundly discussed in chapter 1. From the experimental data it has been possible to find the polarization curves for every SOC at variable flow factor. These curves have been drawn by couples of points “Voltage-Current” obtained from the experimental tests and for any of these couples of points it was calculated the value of internal resistance by simply this relation:

$$R_{int} = \frac{OCV - V}{I} \quad (3.4)$$

Where OCV is the open circuit voltage, V is the stack voltage, and I is the electric current.

The figures 3.6, 3.7, 3.8, and 3.9 show the polarization curves for each value of SOC. As seen the polarization curves relative at SOC equal to 20% is characterized by fewer points than other curves because only currents of 10 A and 30 A have been applied. Indeed, higher currents would have requested too high values of flow rate or too low values of cell voltage (cell voltage less than 0.1 V could damage the electrodes). It is worth noting that the polarization curves do not show activation losses except the curves relative at SOC equal to 20% with flow factor less than 10 and the curves relative at SOC equal to 40% with a flow factor equal to 4. Finally, observing these curves it was found the most interesting result, namely that for each SOC there is a value of flow factor above which all the curves collapse one on the other. This means that from a certain value of flow factor the internal resistance doesn't depend on the flow rate and flow factor but depends only on other electric factors. This value of flow factor for any SOC will be called limit flow factor α_{lim} . So, in this study the internal resistance

has been considered as the sum of two main contributes than can be summaries as an ionic resistance R_{ion} and a flow resistance R_{flo} . The first one is due to electric factors and only depends on the State of Charge SOC. The second one is due to fluid dynamic phenomena and only depends on the flow rate Q and the flow factor α :

$$R_{ion} = \phi(SOC) \quad (3.5)$$

$$R_{flo} = \psi(\alpha, Q) \quad (3.6)$$

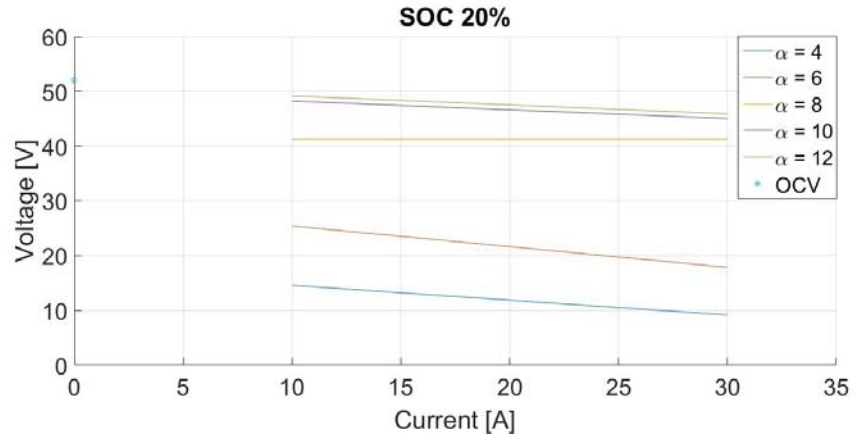


Figure 3.6: Polarization curve at SOC 20%.

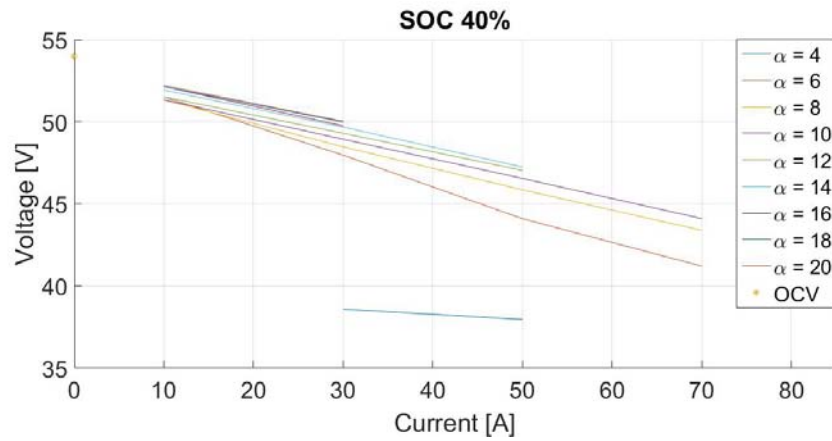


Figure 3.7: Polarization curve at SOC 40%.

The ionic resistance has been calculated by the slope of the polarization curves relative at α_{lim} for any SOC. These values are summarized in Table 3.2 and represented in figure 3.10. As seen the value of ionic resistance decreases as the SOC increases due to lower activation overpotential, ohmic overpotential and concentration overpotential because of a higher number of active species inside the electrolytes.

The flow resistance has been calculated as the difference between the internal resistance and the ionic resistance considering only the experimental data relative at values

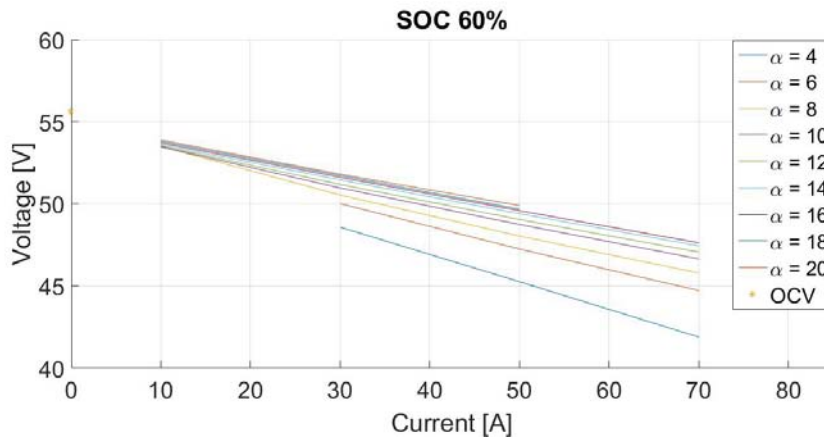


Figure 3.8: Polarization curve at SOC 60%.

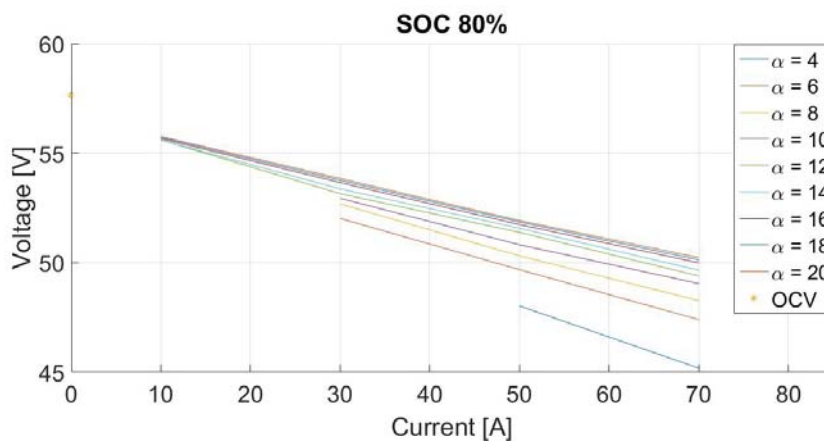


Figure 3.9: Polarization curve at SOC 80%.

Table 3.2: Ionic resistances at different SOC.

SOC [%]	Ionic resistance [Ohm]
20	0.1647
40	0.1172
60	0.1013
80	0.0946

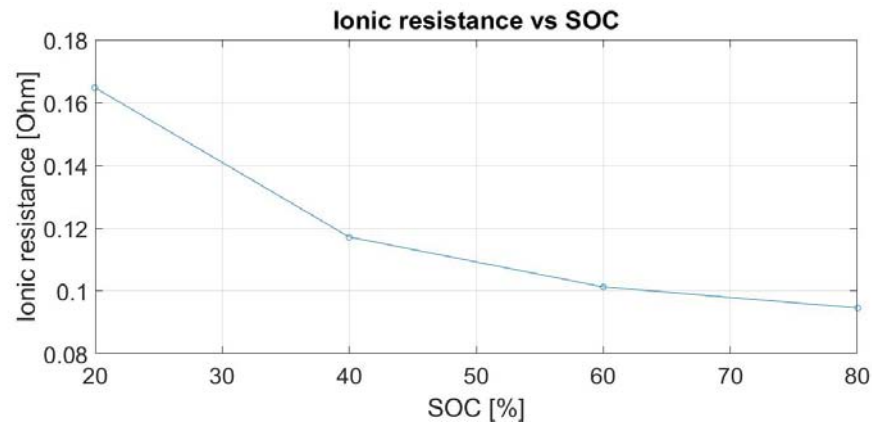


Figure 3.10: Ionic resistance relates to SOC.

of flow factor greater than or equal to 10 for any value of SOC except SOC 20%. This means that only experimental points characterized by stationary conditions have been taken into account.

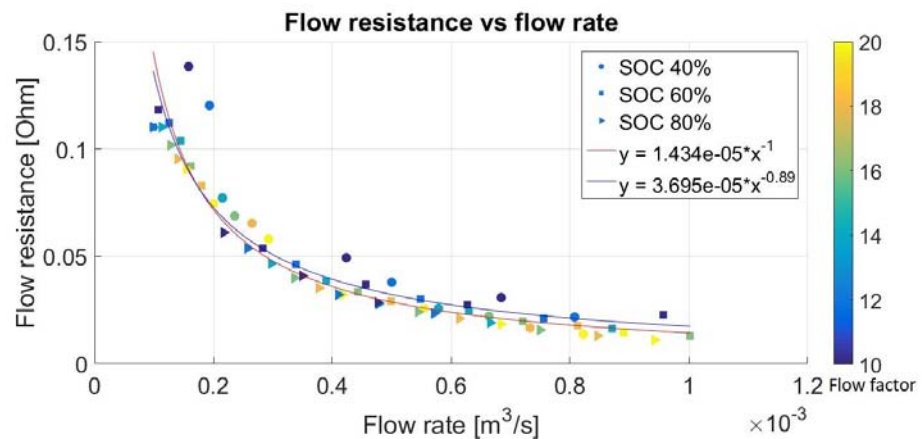


Figure 3.11: Flow resistance versus flow rate (lin-lin).

It is important nothing that regardless of the value of SOC the flow resistances decrease as the flow factor increase but only until a certain point. Indeed, these resistances tend to generate a kind of master curve which indicates that even if the value of flow factor rises besides a value of saturation flow factor α_{sat} the flow resistance doesn't change anymore but it depends only on the value of flow rate.

The figures 3.11 and 3.12 show that higher the flow rate, lower the flow resistance is. This important results will be analyzed in chapter 4.

3.6 Pump losses analysis

The pump losses are amply discussed in chapter 2. In this section an analyse of the pump losses based on the experimental data will be depth. From the experimental

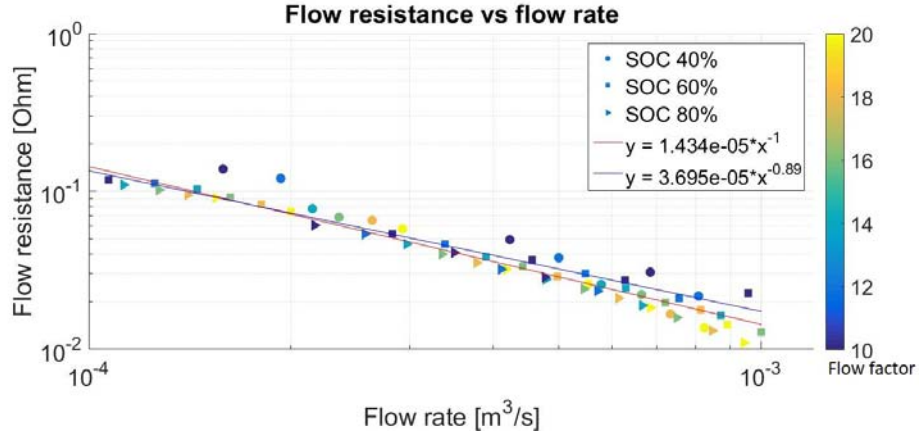


Figure 3.12: Flow resistance versus flow rate (log-log).

tests, the pump power needed to circulate the electrolytes and the differential pressure between inlet and outlet the stack are analysed in order to study the relation between these data and the flow rate to observe a correlation with the theoretical results.

As discussed in chapter 2, the pressure drop between inlet and outlet the stack can be obtained by the Darcy's law:

$$\Delta P_{stack} = \frac{\mu L_x \varepsilon}{k L_y L_z n} Q \quad (3.7)$$

Where Q is the flow rate, L_x , L_y , and L_z are the length, width and thickness of the porous electrode, ε is the porosity of the porous electrode, μ is the dynamic viscosity, n is the number of cells, and k is the permeability. These specifications are summarized in Table 3.3. It is worth noting that to calculate the pressure drop inside the stack it is

Table 3.3: Specifications of VRFB.

Parameters	Value
L_x	0.2 [m]
L_y	0.3 [m]
L_z	0.0057 [m]
ε	0.69
n	40

needed to consider the flow rate of the single cell and not the total flow rate because the cells are feed in parallel.

The total stack power lost P_{stack} inside the stack can be found by the product between the pressure drop and the total flow rate as follows:

$$P_{stack} = \Delta P_{stack} Q \quad (3.8)$$

And considering the ΔP_{stack} defined in (3.7):

$$P_{stack} = \frac{\mu L_x \varepsilon}{k L_y L_z n} Q^2 \quad (3.9)$$

From the experimental results it is expected to find a relation with the flow rate at least quadratic, according to the theory. The figures 3.13, 3.15, 3.17, 3.19, 3.14, 3.16, 3.18, and 3.20 show that this relation is a little more than quadratic. Probably, this is due to inertial effects at high value of flow rate when the Reynolds number is higher. The data fit of P_{stack} at various SOC as a function of flow rate is summarized in Table 3.4.

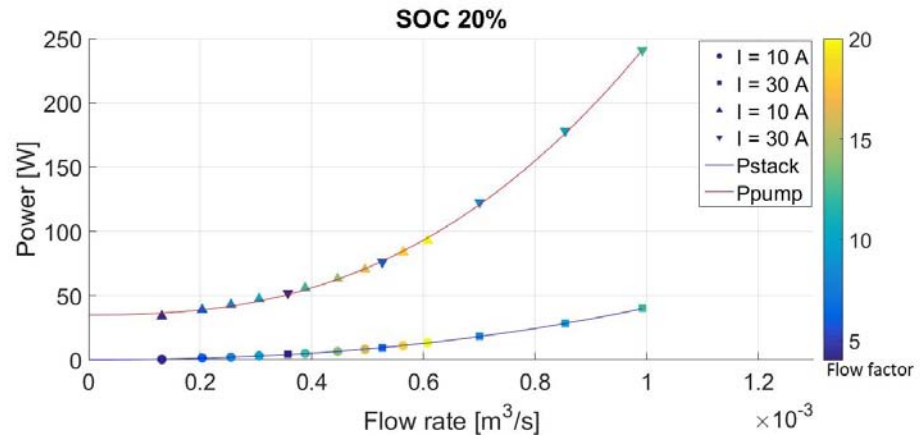


Figure 3.13: P_{pump} and P_{stack} vs flow rate SOC 20% (lin-lin).

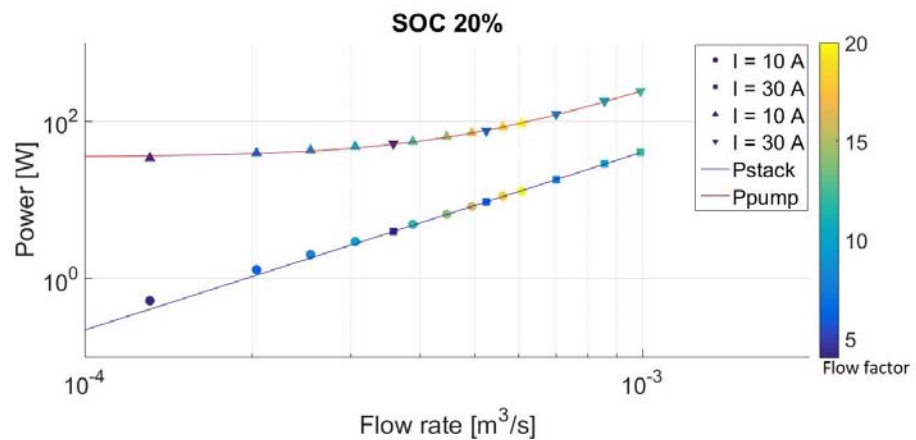


Figure 3.14: P_{pump} and P_{stack} vs flow rate SOC 20% (log-log).

The previous figures also show the pump power P_{pump} measured needed to the functioning of the plant. As seen this pump power is much greater than the total stack power is much greater than the total stack power lost inside the stack. This means that there are high losses inside the pipe system characterized by elbows, tees, valves, sudden contraction, sudden expansion, flow meters etc., and a low pump system efficiency.

The figures 3.21, 3.22, 3.23, and 3.24 shows the ratio P_{stack}/P_{pump} . As seen this ratio enhanced rapidly until a certain value of flow rate and then it stabilizes on a value approximately equal to 16%. This behaviour is due to that at low flow rates there are low values of pump efficiency that affect the system efficiency. This ratio seems very

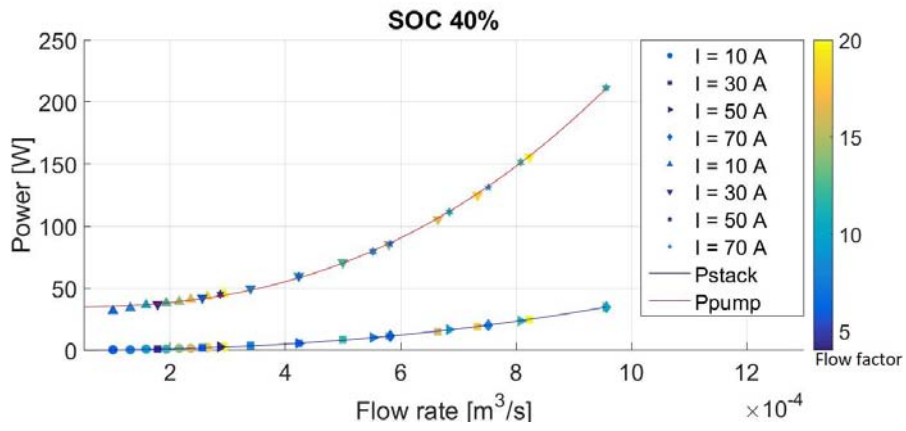


Figure 3.15: P_{pump} and P_{stack} vs flow rate SOC 40% (lin-lin).

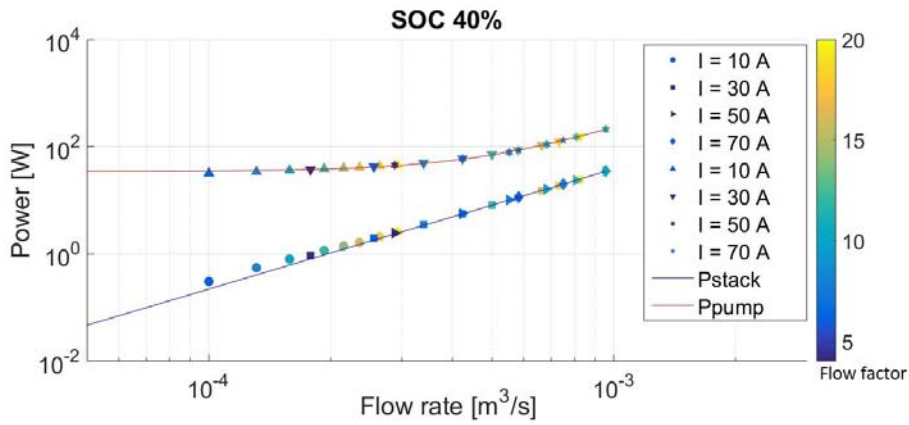


Figure 3.16: P_{pump} and P_{stack} vs flow rate SOC 40% (log-log).

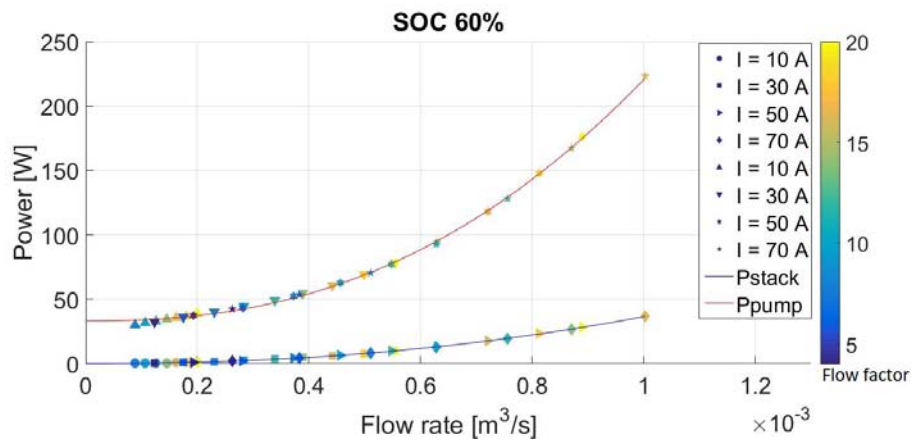


Figure 3.17: P_{pump} and P_{stack} vs flow rate SOC 60% (lin-lin).

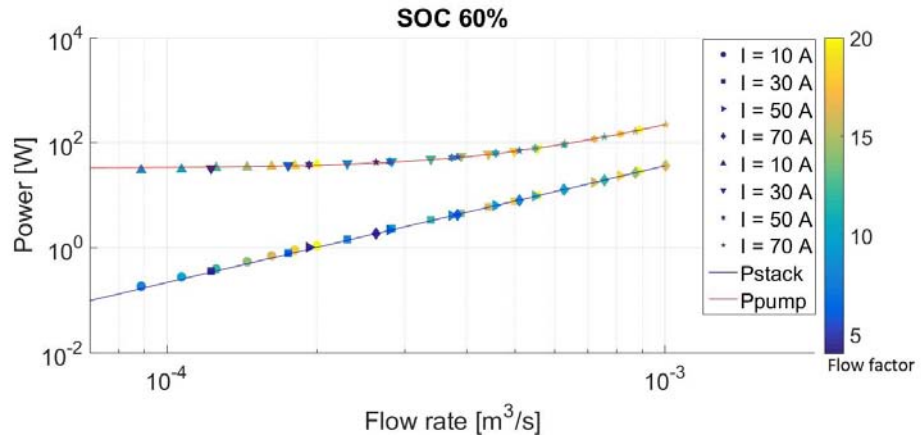
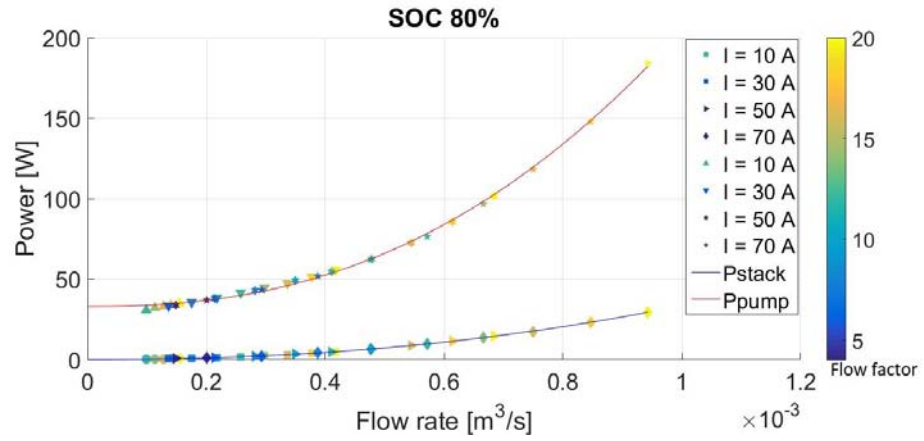
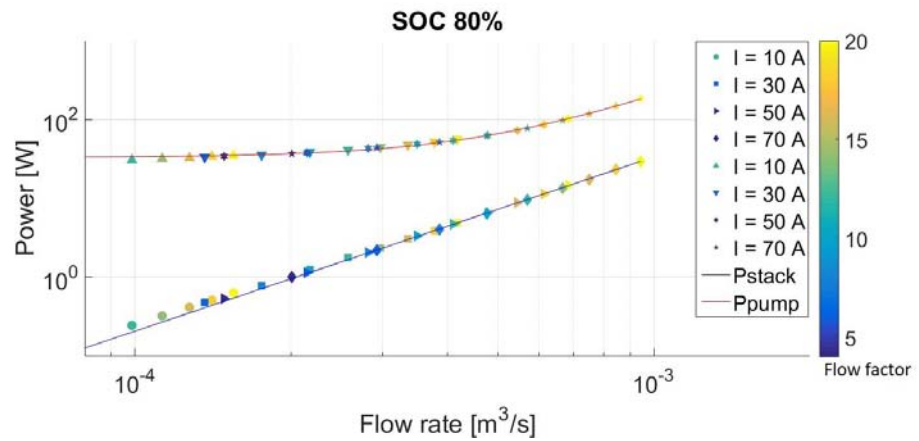
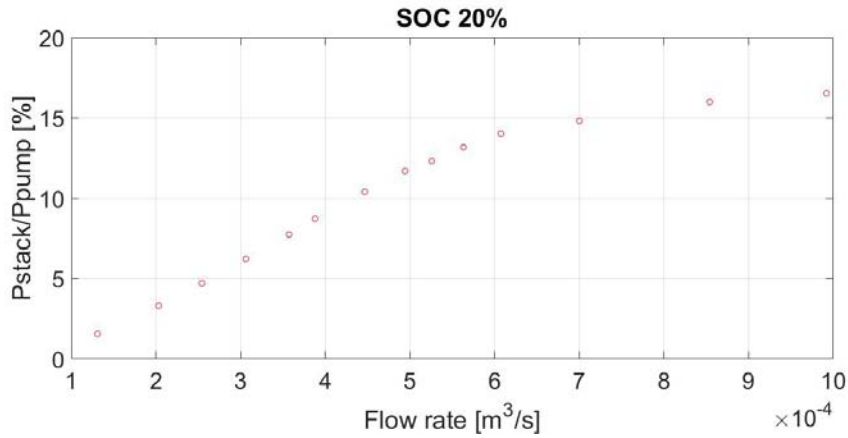
Figure 3.18: P_{pump} and P_{stack} vs flow rate SOC 60% (log-log).Figure 3.19: P_{pump} and P_{stack} vs flow rate SOC 80% (lin-lin).Figure 3.20: P_{pump} and P_{stack} vs flow rate SOC 80% (log-log).

Table 3.4: Data fit of P_{stack} .

SOC	P_{stack} vs Q	R-square
20	$P_{stack} = 2.44E + 8Q^{2.26}$	0.9999
40	$P_{stack} = 1.98E + 8Q^{2.24}$	0.9998
60	$P_{stack} = 1.68E + 8Q^{2.22}$	0.9999
80	$P_{stack} = 1.42E + 8Q^{2.21}$	0.9998

low, but it is important observing that some components of the feed system, such as the flow meters or some valves that contribute to enhance the pressure losses, are used only for academic research and they are not needed in industrial plants. Moreover, the pump system composed by pumps, inverters, and electric motors is not so efficient and maybe better performance can be reached thanks to better components.

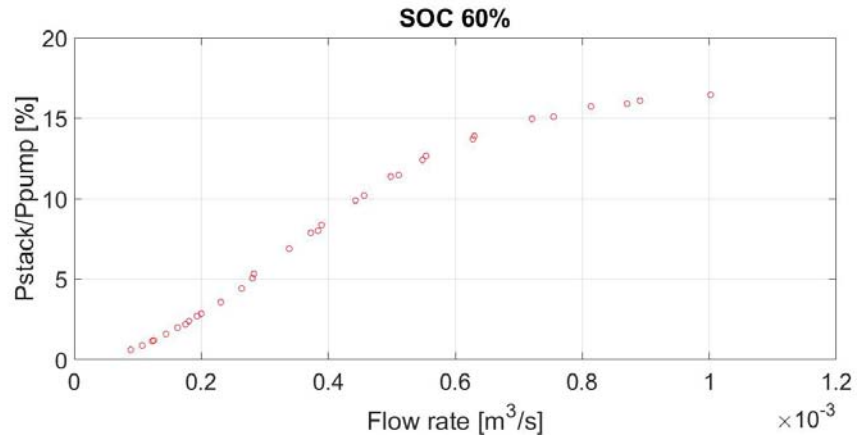
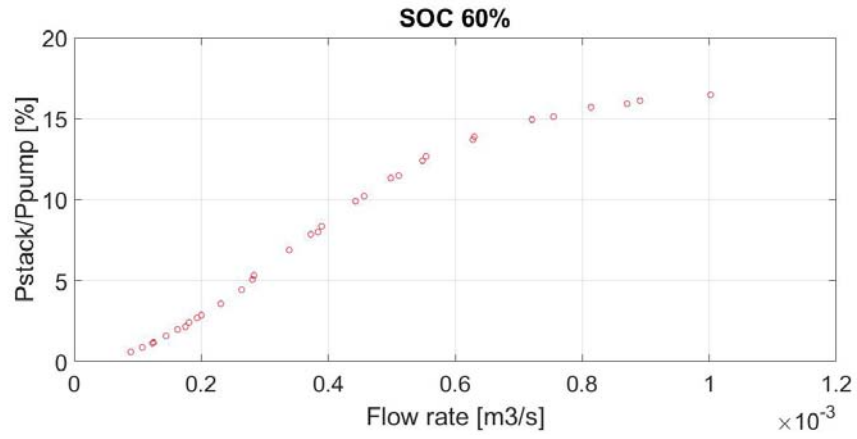
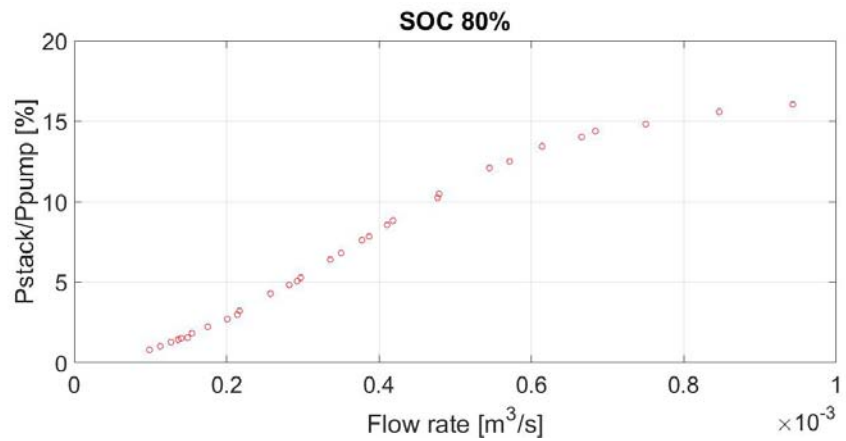
A study of the major and minor losses that characterized the feeding system as described in section 2.7.1 has been performed in order to define approximately the main loss components. This study has been investigated using a flow rate of 29.5 l/min for both the positive and negative electrolytes. The performance curve (figure 3.25) of the pumps used, model Sanso PMD-641 [43], show a total head roughly equal to 4.3 m. Thus, considering that the system is characterize by two pumps, the total head resulting from the datasheet is 8.6 m.

Figure 3.21: P_{stack}/P_{pump} versus flow rate SOC 20%.

By setting a value of pump efficiency equal to 0.65, an inverter efficiency equal to 0.95, and an electric motor efficiency equal to 0.75, the model of head losses has been implemented in MATLAB.

Table 3.5 shows the main components that characterized the VRFB system, the head losses expressed in meters, and the head losses expressed in Pascal. As seen the results of the implemented model are in line with the theoretical results.

Finally, considering the power needed to feed the inverters when the system is stopped equal to 8.5 W, the total pump power needed resultant from the model is 223.54 W that, compared with the experimental one equal to 223.20 W, shows an error equal to 0.15%.

Figure 3.22: P_{stack}/P_{pump} versus flow rate SOC 40%.Figure 3.23: P_{stack}/P_{pump} versus flow rate SOC 60%.Figure 3.24: P_{stack}/P_{pump} versus flow rate SOC 80%.

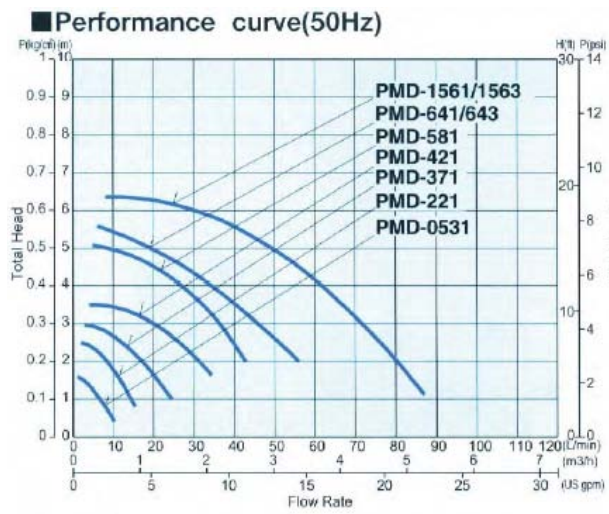


Figure 3.25: Performance curve Sanso PMD-641 pump [43].

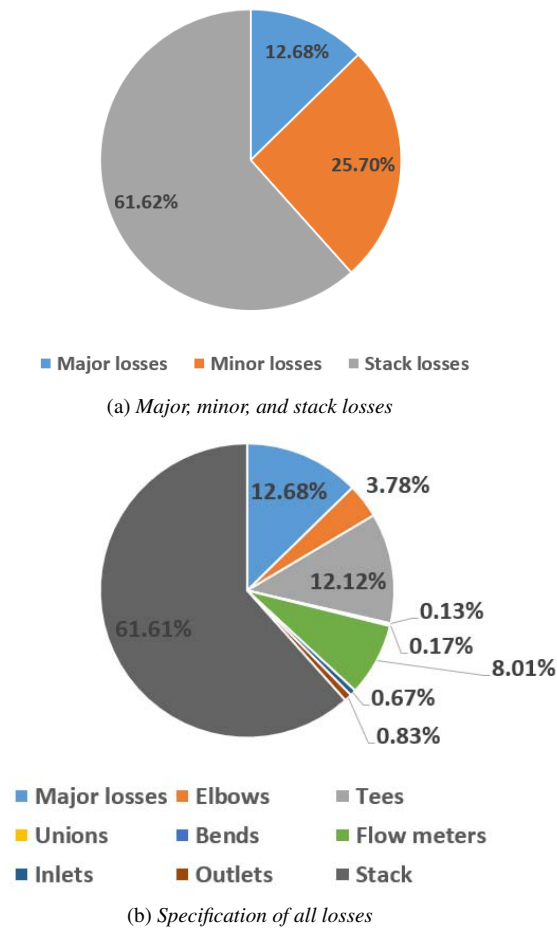


Figure 3.26: Representation of head losses.

Table 3.5: Head losses of main components of the VRFB system.

Components	Head losses [m]	Head losses [Pa]
Major losses	1.14	15142.32
Elbows	0.34	4516.13
Tees	1.09	14478.19
Unions	0.012	159.39
Bends	0.015	199.24
Flow meters	0.72	9563.57
Inlets	0.06	796.96
Outlets	0.075	996.21
Stack	5.54	73586.38
Total model	8.99	119411.83
Total theory	8.6	114231.56
Error [%]	4.53	4.53

3.7 Optimization of electrolyte flow rate

In this section an optimal flow rate management will be discussed in order to achieve the maximum overall efficiency of the battery. This battery efficiency is provided by the minimum value of total losses, which are characterized by hydraulic losses and electrical losses.

As seen in previous sections, the hydraulic power inside the stack required for providing electrolyte flow through porous media can be found as:

$$P_{pump} = \Delta P_{tot} Q \quad (3.10)$$

Where Q is the flow rate, and ΔP_{tot} is sum of differential pressure between inlet and outlet the stack, minor losses, and major losses along pipe system as follows:

$$\Delta P_{tot} = \Delta P_{stack} + \Delta P_{major} + \Delta P_{minor} \quad (3.11)$$

Internal battery electrical losses depend on internal resistance and current. The electrical power can be represented as follows:

$$P_{elec} = R_{int} I^2 \quad (3.12)$$

Where I is the applied current, and R_{int} is the internal resistance that is a function of flow rate, and SOC.

So, both pump power and electrical power depend on electrolyte flow rate. Pump power increases if the flow rate rises because the pressure drop is higher, while electrical power decreases if the flow rate increases because the internal resistance is lower. In particular, pump power is proportional to approximately Q^2 , while electrical power is proportional to roughly Q^{-1} .

Total power needed for the functioning of the stack can be expressed as the sum of hydraulic power and electrical power as follows:

$$P_{tot} = P_{pump} + P_{elec} \quad (3.13)$$

Analysing the experimental data, an optimal flow rate management for different SOC's and battery currents has been developed. As described previously, a total range of SOC's from 20% to 80% was chosen, while the battery currents applied were 10, 30, 50, and 70 A. The range of possible flow rates was selected in accordance with the capability of the hydraulic system. Flow rates below 2 l/min cause cell voltages less than 0.1 V that can damage the porous electrodes. Flow rates above 29.5 l/min are more than the maximum capability of the pumps. So, this optimization study was conducted considering a flow rate for both positive and negative electrolyte between 2 l/min and 29.5 l/min.

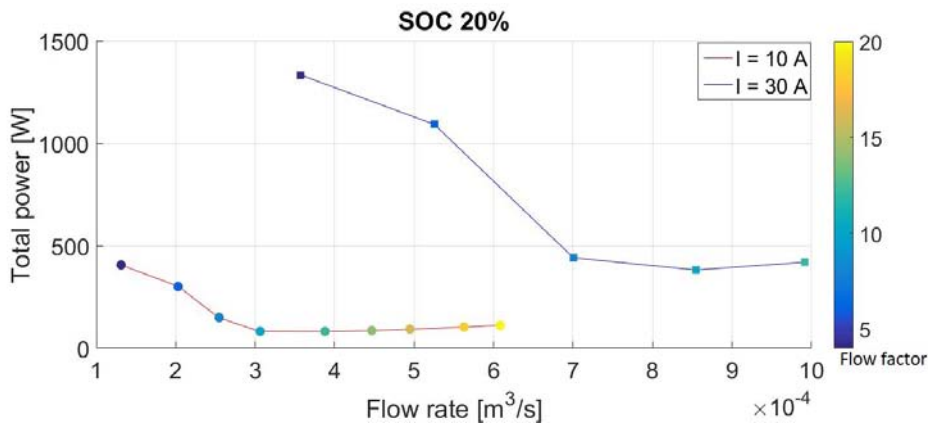


Figure 3.27: Total lost power versus flow rate (SOC 20%).

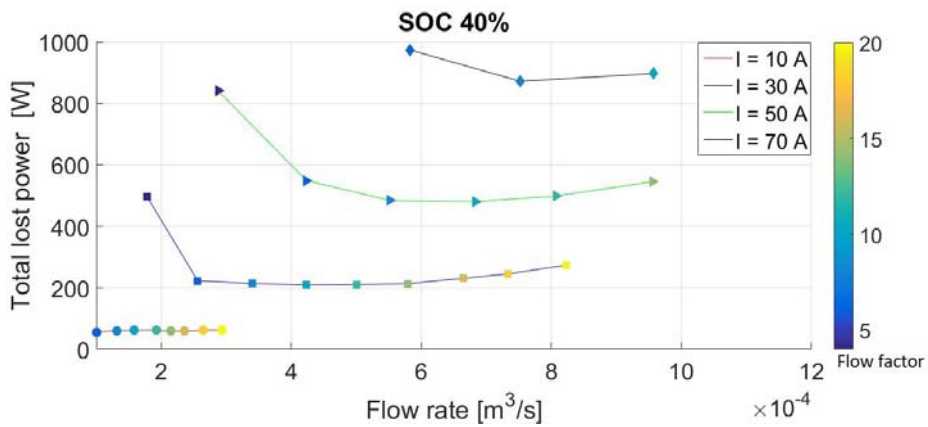


Figure 3.28: Total lost power versus flow rate (SOC 40%).

Figures 3.27, 3.28, 3.29, and 3.30 show the relation between total power and flow rate. As seen, total power for each of these curves have a minimum. Electrolyte flow rate at this point is the optimal value which ensures lower losses.

Battery efficiency η can be considered as the ratio between net power and gross power as follows:

$$\eta = \frac{P_{net}}{P_{gross}} \quad (3.14)$$

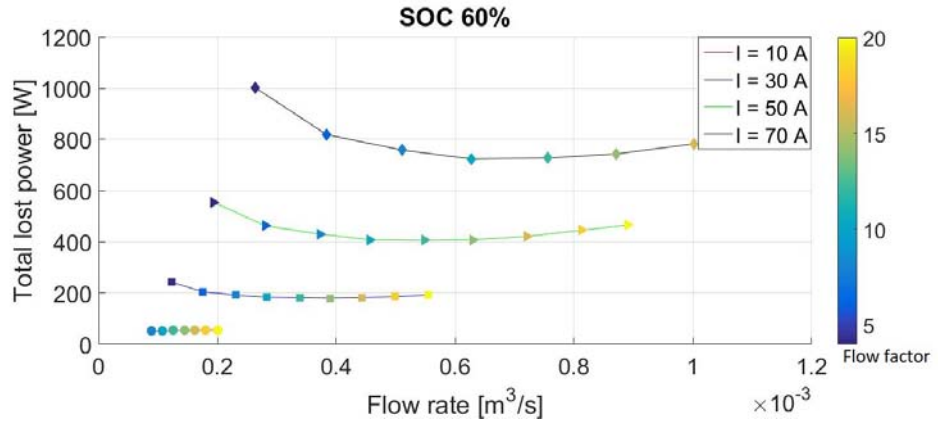


Figure 3.29: Total lost power versus flow rate (SOC 60%).

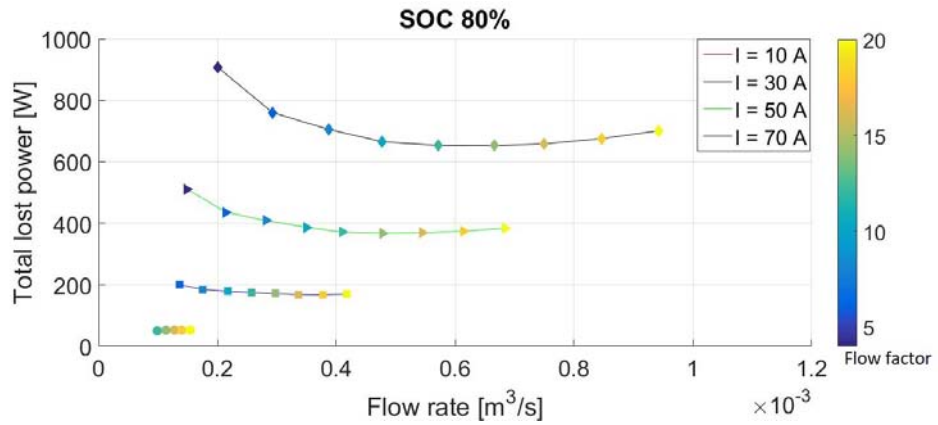


Figure 3.30: Total lost power versus flow rate (SOC 80%).

Where the net power is the useful power output from the battery, namely the output power without pump power and electrical power, defined as:

$$P_{net} = OCV * I - P_{pump} - P_{elec} \tag{3.15}$$

While, the gross power is the useful power plus pump power plus electrical power described as:

$$P_{gross} = OCV * I + P_{pump} + P_{elec} \tag{3.16}$$

Where OCV is the open circuit voltage.

Clearly, as seen in figures 3.31, 3.32, 3.33, and 3.34 the optimal flow rate which gives the lower losses also guarantees the maximum battery efficiency. Indeed, battery efficiency for each of these curves present a maximum. Figures 3.35, 3.36, 3.37, and 3.38 show the same results discussed above by means of a colour map that indicates the values of efficiency.

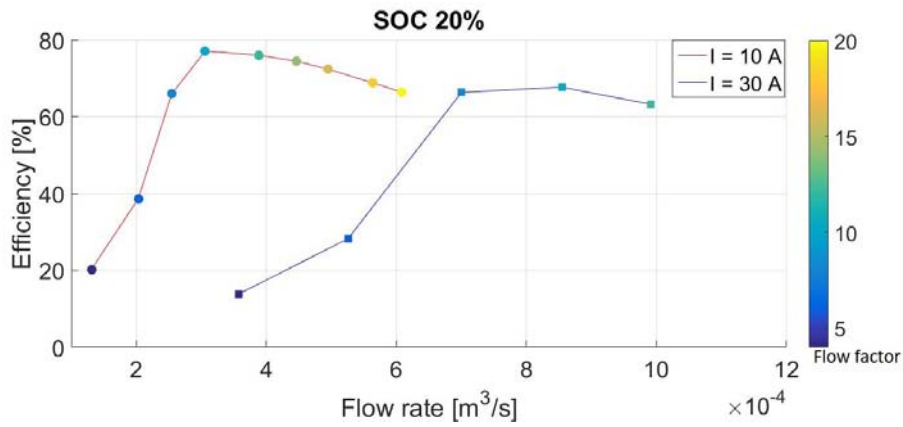


Figure 3.31: Battery efficiency versus flow rate (SOC 20%).

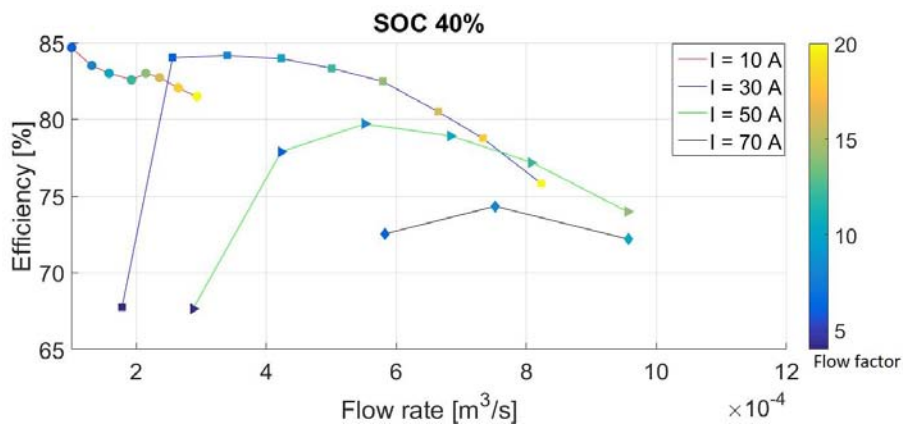


Figure 3.32: Battery efficiency versus flow rate (SOC 40%).

It is interesting to compare the maximum battery efficiency with the battery efficiencies related to the minimum and maximum available flow rates for every SOC

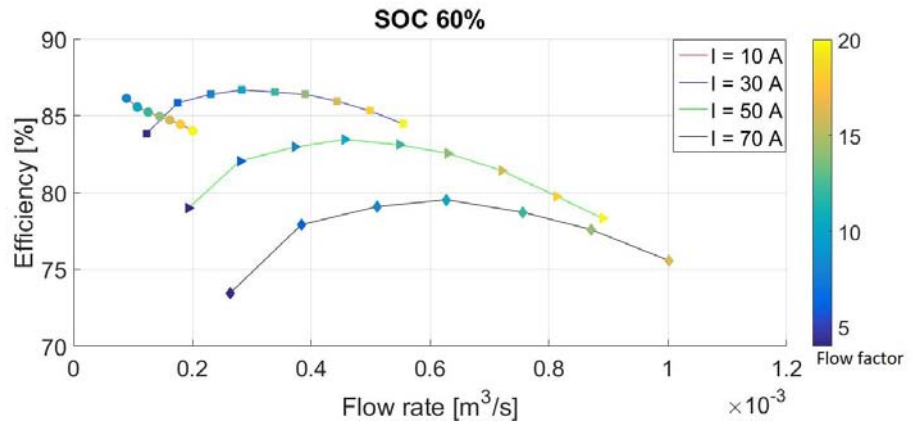


Figure 3.33: Battery efficiency versus flow rate (SOC 60%).

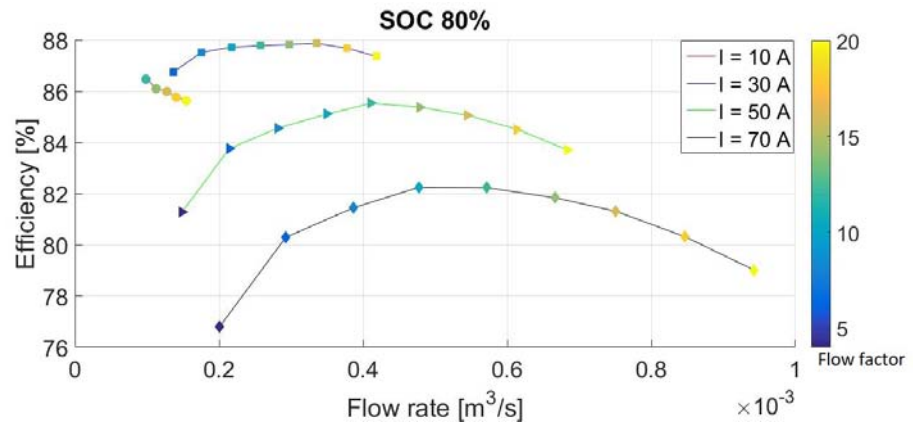


Figure 3.34: Battery efficiency versus flow rate (SOC 80%).

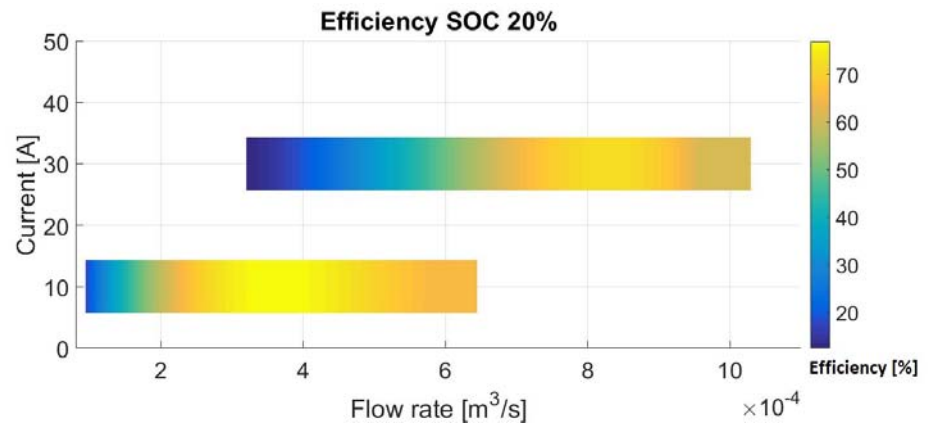


Figure 3.35: Battery efficiency versus flow rate, colour map (SOC 20%).

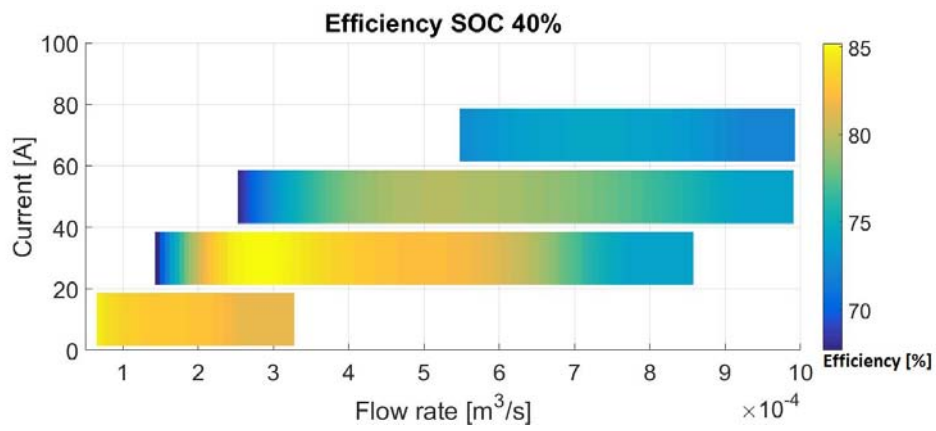


Figure 3.36: Battery efficiency versus flow rate, colour map (SOC 40%).

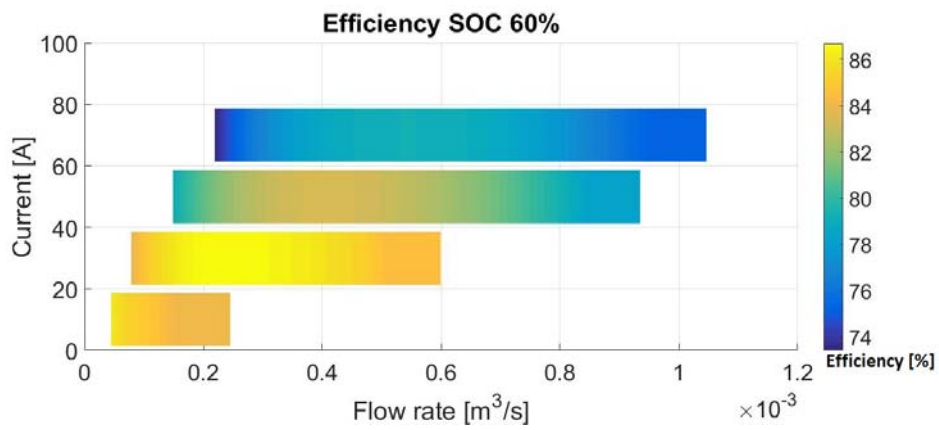


Figure 3.37: Battery efficiency versus flow rate, colour map (SOC 60%).

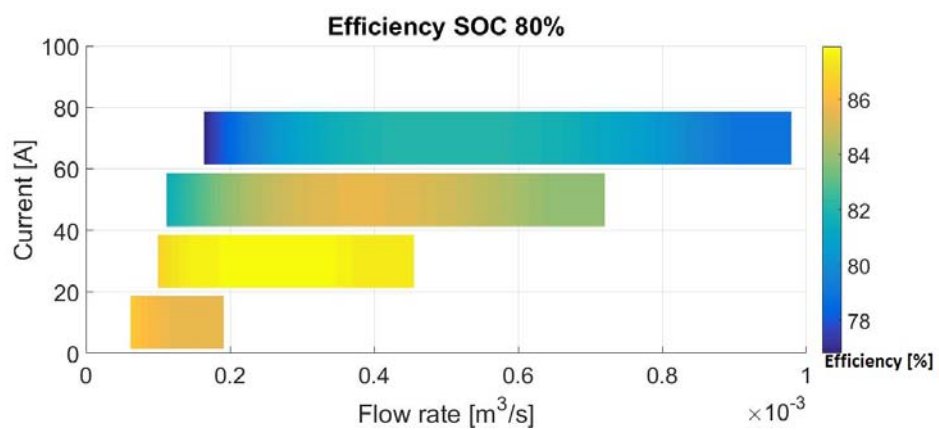


Figure 3.38: Battery efficiency versus flow rate, colour map (SOC 80%).

and applied current. This can show how much the optimization of the pumping process could improve VRFB efficiency. Results show that a flow rate optimization could achieve a greater efficiency up to 56% more compared to a minimum flow rate and up to 10% more compared to a maximum flow rate. Results of the study for various SOC and battery currents are summarized in Table 3.6.

Table 3.6: Battery efficiencies at various SOC and applied currents.

SOC [%]	Current [A]	Q_{opt} [l/min]	η_{opt} [%]	Q_{min} [l/min]	η [%]	$\Delta\eta$ [%]	Q_{max} [l/min]	η [%]	$\Delta\eta$ [%]
20	10	18.35	77.06	7.86	20.28	56.79	36.45	66.44	10.62
20	30	51.27	67.69	21.44	13.85	53.84	59.50	63.20	4.49
40	10	6.00	84.67	6.00	84.67	0.00	17.58	81.49	3.19
40	30	20.36	84.17	10.68	67.72	16.45	49.37	75.82	8.35
40	50	33.08	79.70	17.24	67.66	12.05	57.32	73.98	5.72
40	70	45.10	74.34	34.95	72.54	1.79	57.42	72.19	2.15
60	10	5.33	86.12	5.33	86.12	0.0	12.00	84.02	2.10
60	30	16.99	86.68	7.37	83.84	2.84	33.24	84.48	2.20
60	50	27.41	83.46	11.59	79.98	4.47	53.42	78.31	5.14
60	70	37.65	79.53	15.79	73.44	6.08	60.13	75.57	3.96
80	10	5.92	86.48	5.92	86.48	0.0	9.28	85.62	0.86
80	30	20.15	87.86	8.18	86.74	1.12	25.06	87.36	0.50
80	50	24.64	85.52	8.91	81.27	4.25	41.03	83.71	1.81
80	70	28.63	82.24	12.03	76.79	5.45	56.57	79.01	3.23

3.8 Viscosity measurement and permeability

In this section the viscosities of both positive and negative electrolytes will be investigated in order to find the permeability K of the porous medium. The initial idea was to measure the viscosities of the two electrolyte compositions of 1.6 M V in 5 M H_2SO_4 at different SOC using a capillarity viscometer. However, the viscometer has been ordered but unfortunately delivered times were longer than expected, not allowing the scheduled job. So, it was necessary to find the value of viscosities by means of a bibliography research. In [48] the authors have measured the viscosity of two electrolyte solutions characterized by 1.6 M V in 2.6 M H_2SO_4 at different SOC and temperatures using an automatic viscometer. It is worth nothing that our electrolytes are more acidic and maybe the viscosities may be slightly different. The results related to a temperature of 20°C are summarized in Table 3.7. It is noted from Table 3.7 that the viscosity of negative electrolyte solution is higher than the viscosity of positive electrolyte solution. This was visible also from figures 3.39, 3.40, 3.41, and 3.42 which show the already discussed P_{stack} for both the positive and negative half-cell. Indeed, fixed the value of flow rate, the pressure drop between inlet and outlet the negative half-cell is always greater than that of the positive half-cell. This means that the negative electrolyte has got a grater viscosity than the positive electrolyte.

The values of viscosities at different SOC are plotted in figure 3.43. As observed, it is shown that the measured values of viscosity decrease with increasing SOC for both

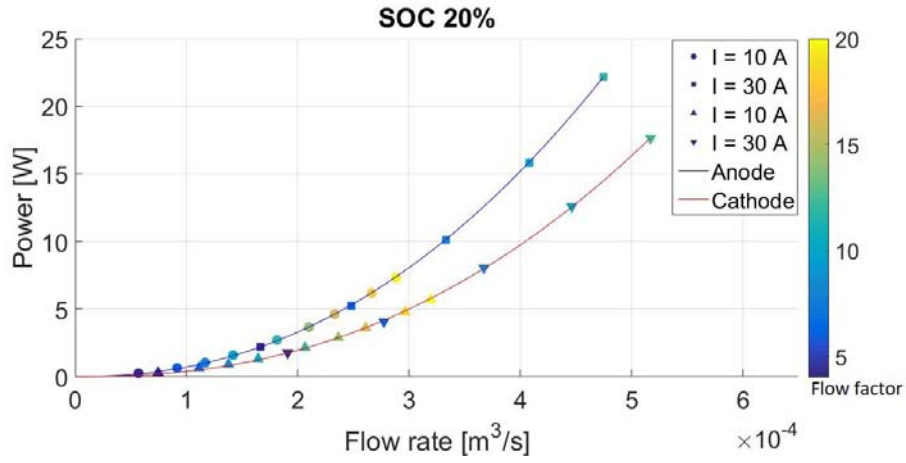
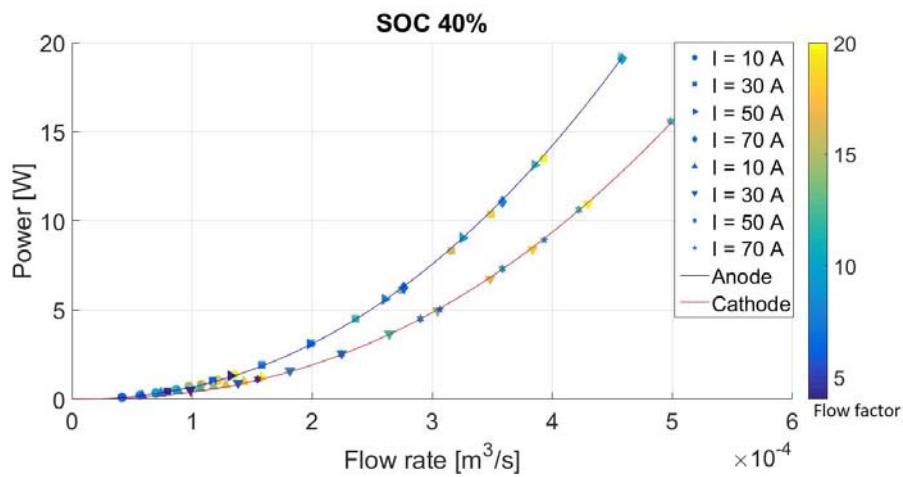
Figure 3.39: P_{stack} anode/cathode vs flow rate SOC 20% (lin-lin).Figure 3.40: P_{stack} anode/cathode vs flow rate SOC 40% (lin-lin).

Table 3.7: Measured viscosities of positive and negative electrolyte at different SOC's [48].

SOC	Negative electrolyte	Positive electrolyte
20	6.166 [$mPa \cdot s$]	5.134 [$mPa \cdot s$]
40	5.686 [$mPa \cdot s$]	4.941 [$mPa \cdot s$]
60	5.299 [$mPa \cdot s$]	4.733 [$mPa \cdot s$]
80	4.837 [$mPa \cdot s$]	4.560 [$mPa \cdot s$]

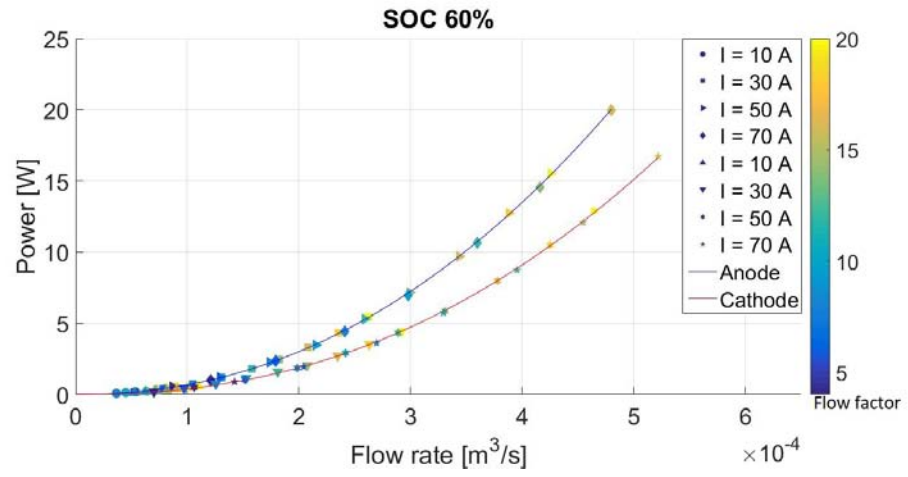


Figure 3.41: P_{stack} anode/cathode vs flow rate SOC 60% (lin-lin).

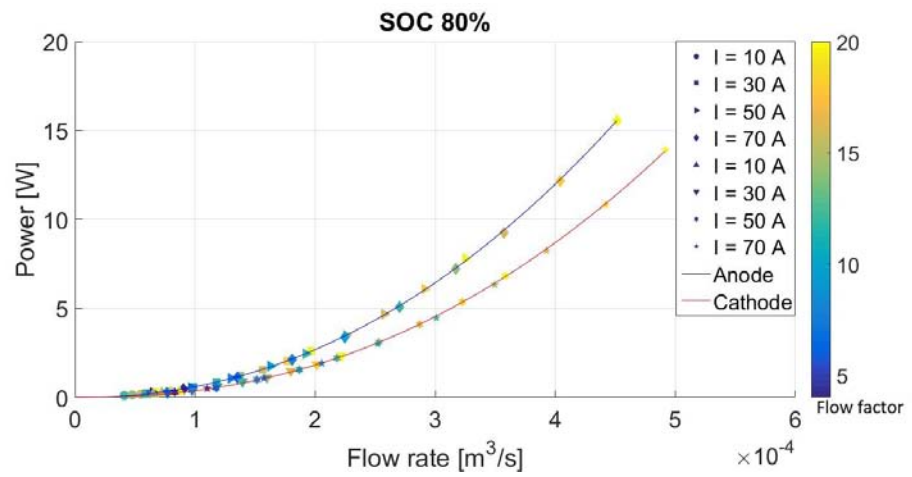


Figure 3.42: P_{stack} anode/cathode vs flow rate SOC 80% (lin-lin).

the positive and negative electrolytes. One possible explanation could be as follows. At high SOC the concentration of vanadium V(II) and V(V) are more than vanadium V(III) and V(IV). Maybe, the V^{2+} and VO_2^+ ions form weaker interactions with sulphate ions than the V^{3+} and VO^{2+} ions. This can lead in a small friction between particles and thus, as the SOC increase, the electrolytes viscosities decrease.

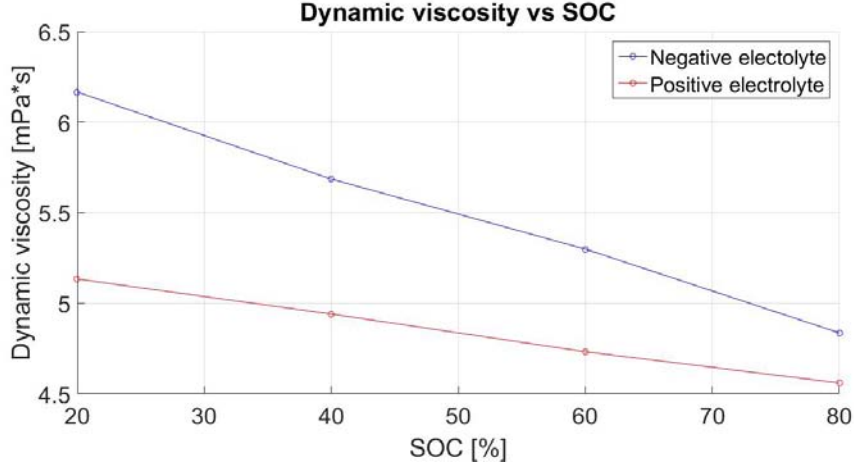


Figure 3.43: Measured viscosities at different SOC.

After this bibliography research, an estimate of the permeability of the porous electrode has been investigated using the Darcy's law previously discussed and the measured viscosities. Indeed, note the electrolytes viscosity, the permeability values of anode and cathode at different SOC have been calculated using the Darcy's law as follows:

$$P_{stack} = \frac{\mu L_x \varepsilon}{k L_y L_z} \frac{Q^2}{n} = A Q^2 \quad (3.17)$$

$$k = \frac{\mu L_x \varepsilon}{A L_y L_z n} \quad (3.18)$$

Where Q is the flow rate, L_x , L_y , and L_z are the length, width and thickness of the porous electrode, ε is the porosity of the porous electrode, n is the number of cells (see Table 3.3 for specifications), and μ is the dynamic viscosity (see Table 3.7).

Table 3.8: Data fit of P_{stack} - anode.

SOC	P_{stack} vs Q	R-square
20	$P_{stack} = 4.65E + 8Q^{2.20}$	0.9999
40	$P_{stack} = 3.99E + 8Q^{2.19}$	0.9998
60	$P_{stack} = 3.09E + 8Q^{2.17}$	0.9999
80	$P_{stack} = 2.56E + 8Q^{2.16}$	0.9998

Tables 3.8 and 3.9 show the data fit of P_{stack} of anode and cathode at different SOC. As seen, because of inertial effects at high values of flow rate, the relation

Table 3.9: Data fit of P_{stack} - cathode.

SOC	P_{stack} vs Q	R-square
20	$P_{stack} = 7.16E + 8Q^{2.31}$	0.9998
40	$P_{stack} = 5.23E + 8Q^{2.28}$	0.9996
60	$P_{stack} = 4.81E + 8Q^{2.27}$	0.9998
80	$P_{stack} = 4.06E + 8Q^{2.26}$	0.9997

Table 3.10: Data fit of P_{stack} - anode without inertial effects.

SOC	P_{stack} vs Q	R-square
20	$P_{stack} = 9.42E + 7Q^2$	0.9947
40	$P_{stack} = 8.75E + 7Q^2$	0.9967
60	$P_{stack} = 8.35E + 7Q^2$	0.9972
80	$P_{stack} = 7.33E + 7Q^2$	0.9970

between P_{stack} and flow rate is a little more than quadratic as previously discussed in section 3.6. So, in order to apply the Darcy's law in such a way to calculate the permeability, the inertial effects will be neglected. The new data fits with a quadratic relation between P_{stack} and flow rate are summarized in Tables 3.10 and 3.11 for anode and cathode respectively. As seen, the R-square is still very close to 1.

The values of permeability have been found from the multiplier coefficient of flow rate obtained from data fit. These values found for both anode and cathode are summarized in Table 3.12. The average values of permeability for positive and negative half-cell are $1.682E-10 m^2$ and $1.310E-10 m^2$ respectively. Now, using the average value of permeability equal to $1.496E-10 m^2$ it is possible to recalculate the values of viscosities. These new values are summarized in Table 3.13. The data fit gives the viscosities of electrolytes as a function of SOC as follows:

$$\mu = -2.481E - 5 * SOC + 0.0075 \quad (\text{Negative electrolyte}) \quad (3.19)$$

$$\mu = -9.795E - 6 * SOC + 0.0048 \quad (\text{Positive electrolyte}) \quad (3.20)$$

Finally, since the porous medium is the same for both the anode and the cathode, we would expect that the two found values of permeability should be the same. However, results show two different values of permeability. Maybe, it is due to that the values of viscosities measured in are slightly different than the real viscosity values of our electrolytes. So, a campaign of measures to investigate the electrolyte viscosities at different SOC's could be an interesting job for the future.

Table 3.11: Data fit of P_{stack} - cathode without inertial effects.

SOC	P_{stack} vs Q	R-square
20	$P_{stack} = 6.20E + 7Q^2$	0.9877
40	$P_{stack} = 5.93E + 7Q^2$	0.9931
60	$P_{stack} = 5.75E + 7Q^2$	0.9928
80	$P_{stack} = 5.38E + 7Q^2$	0.9924

Table 3.12: Values of permeability for anode and cathode.

SOC	Anode	Cathode
20	1.321E-10[m ²]	1.672E-10[m ²]
40	1.306E-10[m ²]	1.682E-10[m ²]
60	1.281E-10[m ²]	1.662E-10[m ²]
80	1.331E-10[m ²]	1.711E-10[m ²]
Average value	1.310E-10[m ²]	1.682E-10[m ²]
Standard deviation	2.193E-12	2.128E-12

Table 3.13: New calculated values of viscosity.

SOC	Negative electrolyte	Positive electrolyte
20	6.982 [mPa * s]	4.594 [mPa * s]
40	6.514 [mPa * s]	4.395 [mPa * s]
60	6.189 [mPa * s]	4.260 [mPa * s]
80	5.436 [mPa * s]	3.986 [mPa * s]

Chapter 4

Discussion and interpretation

In this chapter the main results found from the experimental campaign described in chapter 3 will be discussed. In particular, the dependence between flow rate, flow factor and flow resistance will be the first study investigated; while the strategies to improve the performances of the battery during charge and discharge will be the second topic treated.

4.1 Interpretation of flow resistance results

As discussed in chapter 3, the internal resistance has been divided into two main components: the first one depend on only electric factors and it has been called *ionic resistance*, the second one depends on only flow rate and flow factor and it has been called *ow resistance*. In this section we will try to motivate the behavior of this flow resistance.

The figures 4.1 and 4.2 show the flow resistance versus the flow rate in linear and logarithmic scale respectively. As it is noted from these figures, higher the flow rate, lower the fluid dynamics resistance is. The data were fitted with a tendency line which shows that this resistance is proportional to $Q^{-0.89}$. However, probably it is in reality proportional to Q^{-1} and may be that at high values of flow rate corresponding to high values of Reynolds number there are some inertial effects that reduce the exponent. The equations of these tendency lines are given below:

$$R_{flo} = 1.434e^{-5}Q^{-1} \quad (4.1)$$

$$R_{flo} = 3.695e^{-5}Q^{-0.89} \quad (4.2)$$

As seen, the flow resistance decreases as the flow factor α increases. The interesting and curious thing is that this behavior is true until a certain value of flow factor, that we called saturation flow factor α_{sat} . Exceeded α_{sat} , even if the value of flow factor tends to infinity the flow resistance doesn't decrease anymore with α , but it continues to decline as the flow rate increases. Indeed, from the saturation flow factor all experimental points collapse in a master curve that depends on flow rate. A possible reason of this behaviour is explicable as follows. Probably, it is due to the effects of the effective diffusivity. Indeed, the effective diffusivity is proportional to flow rate as follows:

$$D_{eff} \propto U_d \propto Q \quad (4.3)$$

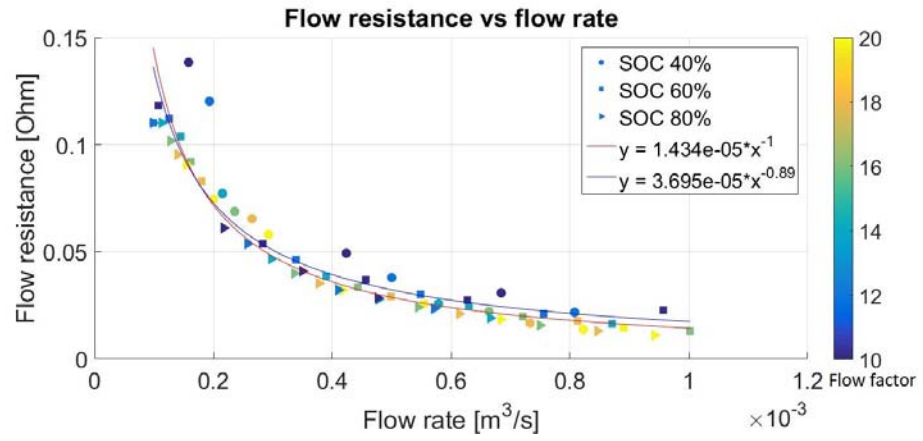


Figure 4.1: Flow resistance versus flow rate (lin-lin).

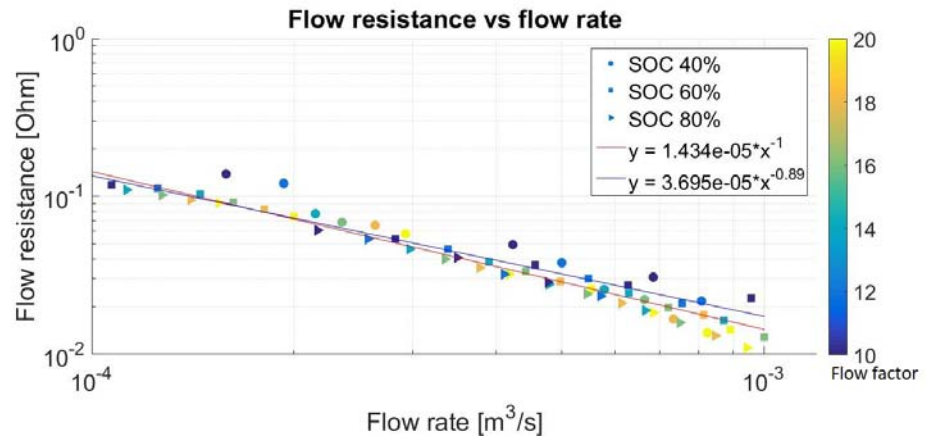


Figure 4.2: Flow resistance versus flow rate (log-log).

Where D_{eff} is the effective diffusivity, Q is the flow rate, U is the bulk velocity, d_f is the fibre diameter, and Re the Reynolds number. So, when the flow rate increases the effective diffusivity increases as well. In conclusion it is possible to relate the flow resistance with the effective diffusivity as:

$$R_{flo} = \frac{1}{D_{eff}} \quad (4.4)$$

Which shows that higher is the effective diffusivity and lower is the R_{flo} . Higher is the flow rate, which means that higher is the Reynolds number and thus the velocity, fastest the mixing of the electrolyte flow due to the porous media is. This involves that there is a greater convective transport of active species near the active surfaces of the electrode and this means that the reactions are faster and thus the flow resistances are lower. In figure 4.3 it is possible to see the gradient of active species concentration where Y is the concentration far from the active surface, and Y_{wall} is the concentration near the active surface. The species concentration drops near the surface of the porous media because the active species react with the applied current. It is worth noting that higher is the flow rate and higher is the gradient of species concentration. The species transport is convective from a microscopic point of view but from a macroscopic point of view it is considered as a diffusive transport characterized by a large value of diffusivity. Practically, we can consider two specie flows as follows:

$$\phi^{vis} = -D \left. \frac{dY}{dn} \right|^{vis} \quad (4.5)$$

$$\phi^{adv-vis} = -D \left. \frac{dY}{dn} \right|^{adv-vis} \quad (4.6)$$

The first one is a purely viscous specie flow when the value of flow rate is low and the second one is a advective-viscous specie flow due to the advection of the tortuous porous media when the value of flow rate is high. The molecular diffusivity is the same for both species flows while the species concentration gradient of the advective-viscous flow is greater than the purely viscous flow and this involves a low value of flow resistance. But, usually it is more convenient considered the reference concentration gradient with a higher value of diffusivity as follows:

$$\phi^{adv-vis} = -D_{eff} \left. \frac{dY}{dn} \right|^{vis} \quad (4.7)$$

Where:

$$D_{eff} = D \frac{\left. \frac{dY}{dn} \right|^{adv-vis}}{\left. \frac{dY}{dn} \right|^{vis}} \quad (4.8)$$

4.2 Performance optimization study

In chapter 3 the total losses that characterized a VRFB system have been discussed. These losses are the internal resistance losses and the pump losses. The pump power, caused by pump losses, and the electrical power, caused by internal resistance losses,

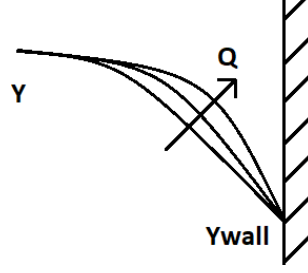


Figure 4.3: Gradient of active species near the active surface.

reduce the battery performances. As seen studying the experimental points derived from the experimental campaign, both pump power and electrical power depend on electrolyte flow rate. In particular we found that the pump power increases if the flow rate rises because the pressure drop is higher, while electrical power decreases if the flow rate increases because the internal resistance is lower. To be precise, pump power is proportional to approximately Q^2 , while electrical power is proportional to roughly Q^{-1} .

We considered the total power needed P_{tot} for the functioning of the battery as the sum of pump power P_{pump} and electrical power P_{elec} as follows:

$$P_{tot} = P_{pump} + P_{elec} \quad (4.9)$$

Analysing this P_{tot} for every SOC and applied current, we have found that there is a certain value of flow rate that minimized the total power. Then, we indicated with η the battery efficiency expressed as:

$$\eta = \frac{P_{net}}{P_{gross}} \quad (4.10)$$

Where P_{net} and P_{gross} represented the net power and the gross power respectively. So, studying this battery efficiency for every SOC and applied current has been found that the same value of flow rate that minimized the total power maximized the η .

It is noted from Table 4.1 how much the optimization of the pumping process could improve VRFB efficiency. In particular, using an optimal flow rate based on the considered value of SOC and applied current could achieve a greater efficiency up to 56% more compared to a minimum flow rate and up to 10% more compared to a maximum flow rate (see Table 4.1).

The roundtrip efficiency is a key parameter that characterized a VRFB system. This parameter can be found through a test which provides a complete charge from minimum SOC to maximum SOC available followed by a complete discharge from the final SOC until the starting SOC using a certain value of applied current.

In addition to roundtrip efficiency, also coulombic efficiency, energy efficiency, and voltage efficiency are important in evaluating the VRFB performance. All these efficiencies are defined as follows:

$$\text{Roundtrip efficiency} = \frac{\text{Discharge energy} - \text{Pump energy}}{\text{Charge energy} + \text{Pump energy}} \quad (4.11)$$

$$\text{Coulombic efficiency} = \frac{\text{Discharge capacity}}{\text{Charge capacity}} \quad (4.12)$$

Table 4.1: Battery efficiencies at various SOCs and applied currents.

SOC [%]	Current [A]	Q_{opt} [l/min]	η_{opt} [%]	Q_{min} [l/min]	η [%]	$\Delta\eta$ [%]	Q_{max} [l/min]	η [%]	$\Delta\eta$ [%]
20	10	18.35	77.06	7.86	20.28	56.79	36.45	66.44	10.62
20	30	51.27	67.69	21.44	13.85	53.84	59.50	63.20	4.49
40	10	6.00	84.67	6.00	84.67	0.00	17.58	81.49	3.19
40	30	20.36	84.17	10.68	67.72	16.45	49.37	75.82	8.35
40	50	33.08	79.70	17.24	67.66	12.05	57.32	73.98	5.72
40	70	45.10	74.34	34.95	72.54	1.79	57.42	72.19	2.15
60	10	5.33	86.12	5.33	86.12	0.0	12.00	84.02	2.10
60	30	16.99	86.68	7.37	83.84	2.84	33.24	84.48	2.20
60	50	27.41	83.46	11.59	79.98	4.47	53.42	78.31	5.14
60	70	37.65	79.53	15.79	73.44	6.08	60.13	75.57	3.96
80	10	5.92	86.48	5.92	86.48	0.0	9.28	85.62	0.86
80	30	20.15	87.86	8.18	86.74	1.12	25.06	87.36	0.50
80	50	24.64	85.52	8.91	81.27	4.25	41.03	83.71	1.81
80	70	28.63	82.24	12.03	76.79	5.45	56.57	79.01	3.23

$$\text{Energy efficiency} = \frac{\text{Discharge energy}}{\text{Charge energy}} \quad (4.13)$$

$$\text{Voltage efficiency} = \frac{\text{Energy efficiency}}{\text{Coulombic efficiency}} \quad (4.14)$$

Where battery charge/discharge energy and capacity are given by:

$$\text{Charge energy} = \int_0^{t_c} E_{charge} I_{charge} dt \quad [Wh] \quad (4.15)$$

$$\text{Discharge energy} = \int_0^{t_d} E_{discharge} I_{discharge} dt \quad [Wh] \quad (4.16)$$

$$\text{Charge capacity} = \int_0^{t_c} I_{charge} dt \quad [Wh] \quad (4.17)$$

$$\text{Discharge capacity} = \int_0^{t_d} I_{discharge} dt \quad [Wh] \quad (4.18)$$

Finally, using the values of optimal flow rate in function of SOC and current found for the discharge of the battery, and repeating the same tests also during charge, we could define a new strategy of charge and discharge of the battery. Instead of using a constant flow rate, or a constant flow factor, we could use the optimal flow rate in order to maximize the key parameters described above. This could allow to reach the maximum overall efficiency of the system. Therefore, an interesting job for the future could be to find the optimal flow rate also during the charge and try to develop an optimal flow rate management that can maximize the battery performances.

Chapter 5

Conclusions

The experimental campaign conducted on the VRFB present in Energy Storage Laboratory at the Dipartimento di Ingegneria Industriale of the University of Padua led to interesting results which are now reassumed.

First of all, we have considered the internal resistance as the sum of the ionic resistance and the electrochemical flow resistance. As seen, the first one depends on electrical factors and it decreases as the SOC increases due to minor concentration, ohmic, and activation losses. The second one depends on flow rate and flow factor and it decreases as flow factor increases but only until a certain value, called saturation flow factor. Exceeded this value, the electrochemical flow resistance continues to decline as the flow rate increases but it does not depend on flow factor anymore. This behaviour is due to the relation between the flow resistance and the effective diffusivity. In particular, higher the flow rate and higher the effective diffusivity is and so lower the flow resistance is.

Then, we have studied the total losses that characterized the system. As seen the pump power needed due to pump losses increases as the flow rate rises. On the other hand, the electrical power needed due to electrical losses decreases as the flow rate increases. So, both the pump power and electrical power depend on flow rate. In particular, we have seen that there are optimal flow rates in function of SOC and applied current that can allow to minimize losses and maximize the battery efficiency. Using an optimal flow rate, we can achieve a greater efficiency up to 56% more compared to a minimum flow rate and up to 10% more compared to a maximum flow rate. This optimal flow rate can be used to develop a new strategy of charge and discharge in order to improve some key parameters such as roundtrip efficiency, coulombic efficiency, energy efficiency, and voltage efficiency.

Moreover, the pump losses of the feeding system have been studied by means of a MATLAB model. It has been found that the flow meters needed to measure the flow rate are responsible of the major losses along pipes. However, the main hydraulic losses are inside the stack. Indeed, the losses inside stack represents more or less the 60% of the total pump losses.

The viscosities of two electrolytes have been analysed. We have seen that the negative electrolyte is characterized by a higher viscosity than the positive one. These values of viscosities found in literature have been used to calculate the permeability of porous electrodes from the experimental points acquired by the experimental campaign. Two slightly different values of permeability have been found for the positive and negative half-cell. It should be remarked that the permeability of the electrodes

should be equal, this can indicate that the values of viscosities of the two electrolytes can be different from what found in literature. It is worth reminding that the viscosities found in literature are relative to electrolytes less acidic than ours. Therefore, an interesting job for the future could be to measure the viscosities of electrolytes at various SOC's using a capillarity viscometer and recalculate the permeability values.

Appendix A

Appendix: Numerical model

In this study, a simulation of the behaviour of the electrodes which form the cells of the stack has been developed. The method used to simulate a flow through a porous media is based on the volume-averaging method. This method consists in modelling the flow as a continuum. The averaged flow is defined in both the fluid phase and solid phase and it is governed by the Volume-Averaged Navier Stokes equations (VANS) discussed in chapter 2. These equations are similar to the equations used in large-eddy simulations (LES). The difference is that the VANS equations consider also the drag force that the flow through a porous media experiences. The VANS equations found in chapter 2 are:

$$\nabla \cdot \mathbf{u}^s = 0 \quad (\text{A.1})$$

$$\begin{aligned} \frac{\partial \mathbf{u}^s}{\partial t} + \nabla \cdot \left[\frac{\mathbf{u}^s \mathbf{u}^s}{\varepsilon} \right] + \nabla \cdot \tilde{\mathbf{u}}\tilde{\mathbf{u}}^s = \\ - \frac{1}{\rho} P^s + \nu \nabla^2 \mathbf{u}^s + \iint_{\partial V_\beta} \mathbf{n} \cdot \left[-\mathbf{I} \frac{\tilde{P}}{\rho} + \nu \tilde{\mathbf{u}} \right] dA \end{aligned} \quad (\text{A.2})$$

And using the Whitaker parametrization of the surface integral in Equation (A.2):

$$\begin{aligned} \frac{\partial \mathbf{u}^s}{\partial t} + \nabla \cdot \left[\frac{\mathbf{u}^s \mathbf{u}^s}{\varepsilon} \right] + \nabla \cdot \tilde{\mathbf{u}}\tilde{\mathbf{u}}^s = \\ - \frac{1}{\rho} P^s + \nu \nabla^2 \mathbf{u}^s - \nu \mathbf{K}^{-1} (\mathbf{I} + \mathbf{F}) \varepsilon \mathbf{u}^s \end{aligned} \quad (\text{A.3})$$

Where \mathbf{u}^s is the superficial volume average velocity, $\tilde{\mathbf{u}}$ is the subfilter-scale velocity, ε is the porosity of porous medium, P is the pressure, ρ is the density, ν is the kinematic viscosity, \mathbf{K} is the permeability tensor, \mathbf{I} is the unit tensor, and \mathbf{F} is the Forchheimer tensor. If we consider that the permeability tensor is isotropic: $\mathbf{K} = K\mathbf{I}$, and the Forchheimer tensor \mathbf{F} can be neglected because the Reynolds number is small, the Equation (A.3) simplifies to:

$$\frac{\partial \mathbf{u}^s}{\partial t} + \nabla \cdot \left[\frac{\mathbf{u}^s \mathbf{u}^s}{\varepsilon} \right] + \nabla \cdot \tilde{\mathbf{u}}\tilde{\mathbf{u}}^s = - \frac{1}{\rho} P^s + \nu \nabla^2 \mathbf{u}^s - \frac{\nu}{K} \varepsilon \mathbf{u}^s \quad (\text{A.4})$$

These equations are valid for a Newtonian and incompressible flow through a rigid porous medium with a constant porosity. Now, closures for the subfilter-scale stress

and drag force are needed to solve the VANS equations. If we consider that in a porous medium the subfilter-scale dispersion is usually negligible with respect to the drag force, the final form of the momentum equation becomes:

$$\frac{\partial \mathbf{u}^s}{\partial t} + \nabla \cdot \left[\frac{\mathbf{u}^s \mathbf{u}^s}{\varepsilon} \right] = -\frac{1}{\rho} \nabla P^s + \nu \nabla^2 \mathbf{u}^s - \frac{\nu}{K} \varepsilon \mathbf{u}^s \quad (\text{A.5})$$

The continuity equation (A.1) and the momentum equation (A.5) have been used to implement a simulation of the flow over a porous medium consisting of a 3D cartesian grid. In particular, a Fortran code called CaNS (Canonical Navier Stokes) made available by Pedro Costa has been opportunely modified in order to implement the VANS equations found above. CaNS is a code for massively-parallel numerical simulations of fluid flows. It aims at solving any fluid flow of an incompressible, Newtonian fluid that can benefit from a FFT-based solver for the second order finite difference Poisson equation in a 3D cartesian grid.

A.1 Numerical Method

The numerical algorithm solves the Volume Averaged Navier-Stokes equations for an incompressible, Newtonian fluid with density ρ , and kinematic viscosity ν :

$$\begin{cases} \nabla \cdot \mathbf{u}^s = 0 \\ \frac{\partial \mathbf{u}^s}{\partial t} + \nabla \cdot \left[\frac{\mathbf{u}^s \mathbf{u}^s}{\varepsilon} \right] = -\frac{1}{\rho} \nabla P^s + \nu \nabla^2 \mathbf{u}^s - \frac{\nu}{K} \varepsilon \mathbf{u}^s \end{cases} \quad (\text{A.6})$$

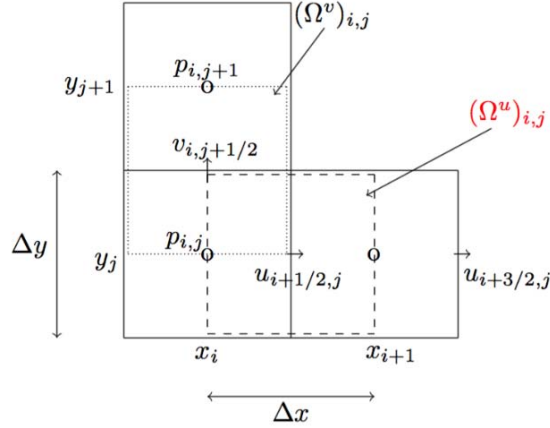


Figure A.1: 2D staggered grid.

These equations are solved in a structured 3D cartesian grid. Standard second-order finite-differences are used for spatial discretization with a staggered disposition of grid points. Figure A.1 shows an example of 2D staggered grid. On a staggered grid the pressure and velocity components are defined at different locations. In particular, the pressure P is defined at the cell centre, while the velocity components are defined at the

centre of the cell faces. In this way, the staggered grid does not result in the decoupling of the pressure and velocities. The equation above are coupled through a pressure-correction method, and integrated in time with a low-storage, three-step Runge-Kutta scheme (RK3). The advancement at each substep k is presented below in semi-discrete notation ($k = 1, 2, 3$; $k = 1$ corresponds to a time level n and $k = 3$ to a time level $n + 1$) [46]:

$$\mathbf{u}^* = \mathbf{u}^k - \Delta t (\alpha_k \mathbf{A} \mathbf{D}^k + \beta_k \mathbf{A} \mathbf{D}^{k-1} - \lambda_k P^{k-1/2}) \quad (\text{A.7})$$

$${}^2\Phi = \frac{\cdot \mathbf{u}^*}{\lambda_k \Delta t} \quad (\text{A.8})$$

$$\mathbf{u}^k = \mathbf{u}^* - \lambda_k \Delta t \Phi \quad (\text{A.9})$$

$$P^{k+1/2} = P^{k-1/2} + \Phi \quad (\text{A.10})$$

$$\mathbf{A} \mathbf{D} = -(\mathbf{u} \cdot \nabla) \mathbf{u} + \nu \nabla^2 \mathbf{u} \quad (\text{A.11})$$

Where \mathbf{u}^* is the prediction velocity, Φ is the correction pressure, and $\alpha_k, \beta_k, \lambda_k$ are the RK3 coefficients given as follows:

$$\alpha_k = \{8/15, 5/12, 3/4\} \quad (\text{A.12})$$

$$\beta_k = \{0, -17/60, -5/12\} \quad (\text{A.13})$$

$$\lambda_k = \alpha_k + \beta_k \quad (\text{A.14})$$

A sufficient criterion for a stable temporal integration is given in [46]:

$$\Delta t < \min \left(\frac{1.65 \Delta r^2}{\nu}, \frac{\bar{3} \Delta r}{\max_{i,j,k} (u + v + w)} \right) \quad (\text{A.15})$$

With $\Delta r = \min(\Delta x, \Delta y, \Delta z)$ and $\Delta x, \Delta y, \Delta z$ are the grid spacing in direction x, y, z.

A.2 Implementation

The numerical algorithm discussed above has been implemented in FORTRAN90/95, with a Message-Passing Interface (MPI) extension for distributed-memory parallelization, combined with a shared-memory parallelization (hybrid MPI-OpenMP). The geometry is divided into several computational subdomains in a pencil-like decomposition. In particular, the $N_p^x * N_p^y$ pencils are aligned in the z direction. An example of a pencil-like domain decomposition, with $N_x * N_y * N_z = 8^3$ grid cells and $N_p^x * N_p^y = 4^2$ computational subdomains (color-coded), is visible in figure A.2 [45].

In this job we simulate a flow through a rigid porous medium represented by means of a 3D domain. The domain size denoted with L_x^* , L_y^* , and L_z^* are calculated as follows:

$$L_x^* = \frac{L_x}{L_z} \quad (\text{A.16})$$

$$L_y^* = \frac{L_y}{L_z} \quad (\text{A.17})$$

$$L_z^* = \frac{L_z}{L_z} \quad (\text{A.18})$$

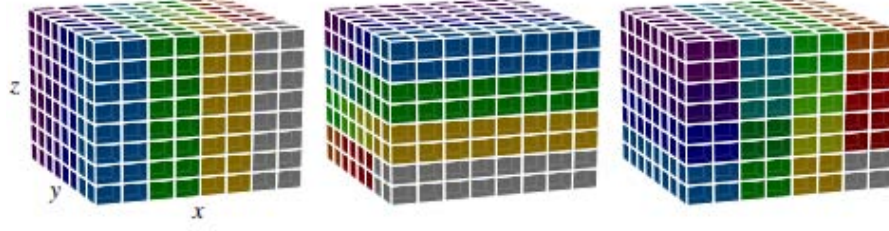


Figure A.2: Pencil-like decomposition [45].

Where L_x , L_y , and L_z are the physical dimensions of the porous medium. To be precise, the length L_x^* is higher than the exact value. This is due to the mask used to simulate the holes where the electrolyte enters the porous medium. According to the Immersed Boundary Method (IBM), the mask is needed to simulate the fluid-structure interactions. How does it work? Practically, we define this mask such that it is equal to zero in correspondence of wall, and equal to one in correspondence of holes. And then, the velocity components are multiplied by the values that the mask assumes. So, the length L_x^* is set in such a way that the distance between the inlet mask and outlet mask is equal to the width of electrode.

The number of points in direction x , y , and z are N_x , N_y , and N_z respectively. Zero-velocity no-slip and no-penetration boundary conditions are considered at all the boundaries, except for the inlet wall, which moves with a velocity $\mathbf{u}(x, y, z) = (U, 0, 0)$, and except for the outlet wall.

Other parameters needed for the simulation are the Reynolds number Re , the Schmidt number Sc , the Peclet number Pe , the porosity of the electrode ε , the dimensionless permeability K^* , and the kinematic viscosity ν defined as follows:

$$Re = \frac{UL_z}{\nu}, \quad U = \frac{Q_c}{L_y L_z} \quad (\text{A.19})$$

$$Sc = \frac{\nu}{D_{eff}} \quad (\text{A.20})$$

$$Pe = Re * Sc \quad (\text{A.21})$$

$$\varepsilon = \frac{0.94}{6.3} (L_x - 1.1), \quad (L_z \text{ in } [mm]) \quad (\text{A.22})$$

$$K^* = \frac{K}{L_z L_z} \quad (\text{A.23})$$

$$\nu = \frac{\mu}{\rho} \quad (\text{A.24})$$

Where ρ is the density, μ is the dynamic viscosity, U is the bulk velocity, Q_c is the single cell flow rate, and D_{eff} is the effective diffusivity. Tables A.1, A.2, and A.3

summarize physical and computational parameters used for the simulation.

Table A.1: Domain size and simulation parameters.

Parameter	Value
L_x	0.2 [m]
L_y	0.3 [m]
L_z	0.0057 [m]
L_x^*	39
L_y^*	52
L_z^*	1
N_x	180
N_y	1040
N_z	20
Q_c	1.1625E-5 [$m^3 s^{-1}$]
U	0.0068 [ms^{-1}]
Re	8.75
Sc	0.15
Pe	1.3125
ε	0.69
K	1.496E-10 [m^2]
K^*	4.604E-6
ρ	1354 [kgm^{-3}]
μ	0.006 [$Pa * s$]
ν	4.431E-6 [$m^2 * s^{-1}$]
D_{eff}	2.95E-5 [$m^2 * s^{-1}$]
ω	0.1 [$kgm^{-3} s^{-1}$]

Moreover, the transport of chemical species equation has been implemented as well. This equation is now given:

$$\frac{Y_a}{\partial t} + \mathbf{u} \cdot \nabla Y_a = \nabla \cdot (D_{eff} \nabla Y_a) + S \quad (A.25)$$

Where Y_a is the concentration of specie a , and S represents the sink term given as follows:

$$S = -\omega Y_a \quad (A.26)$$

Where ω is a constant value that indicates the rates of chemical specie that reacts in the unit of volume and time.

A.3 Simulation results and validation

Figures A.3, and A.4 show the abs velocity field, and the pressure field respectively. To better appreciate the abs velocity field, the values obtained have been opportunely rescaled (figure A.5). It is noted from figure A.5 that the flow accelerates in correspondence of holes where the electrolyte enters and exits the porous medium; while in the central part of the domain the flow velocity is homogeneous, and this is as expected. As seen from figure A.4, the pressure field is definitely smooth. The pressure decreases from inlet to outlet homogeneously. Figure A.6 shows the concentration of chemical

Table A.2: Velocity boundary conditions (N = Neumann boundary conditions, D = Dirichlet boundary conditions).

Component	Direction	Lower bound	Upper bound	Lower BC	Upper BC
u	x	D	N	1	0
u	y	D	D	0	0
u	z	D	D	0	0
v	x	N	N	0	0
v	y	D	D	0	0
v	z	D	D	0	0
w	x	N	N	0	0
w	y	D	D	0	0
w	z	D	D	0	0

Table A.3: Pressure boundary conditions (N = Neumann boundary conditions, D = Dirichlet boundary conditions).

Component	Direction	Lower bound	Upper bound
P	x	N	D
P	y	N	N
P	z	N	N

species. As seen, there is a scalar that varies from one to zero. It represents the vanadium ions V^{3+} ($Y = 1$) that are transformed into VO^{2+} ions ($Y = 0$), or V^{2+} ($Y = 1$) that are transformed into VO_2^+ ($Y = 0$) ions during charge at negative and positive half cell respectively; or vice-versa during the discharge.

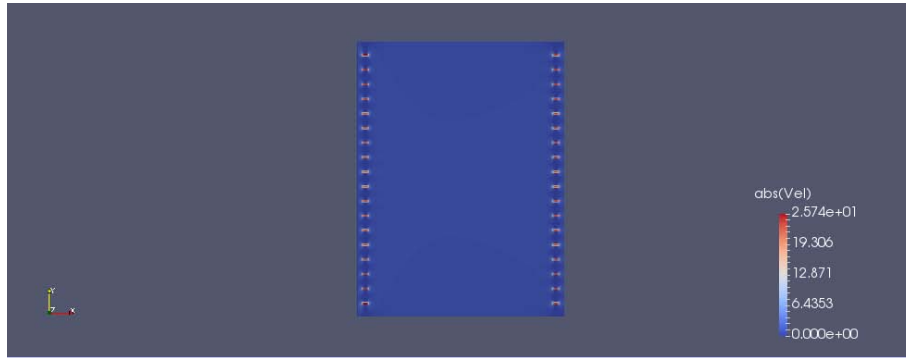


Figure A.3: Simulated abs velocity field.

In order to validate the code, the imposed flow rate Q_c has been compared with the

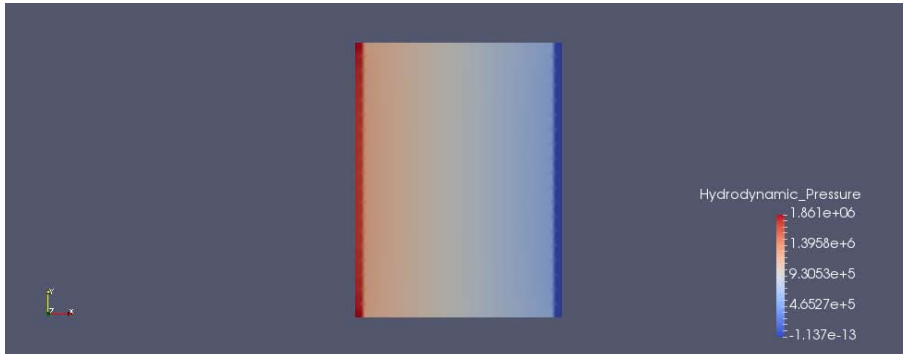


Figure A.4: Simulated pressure field).

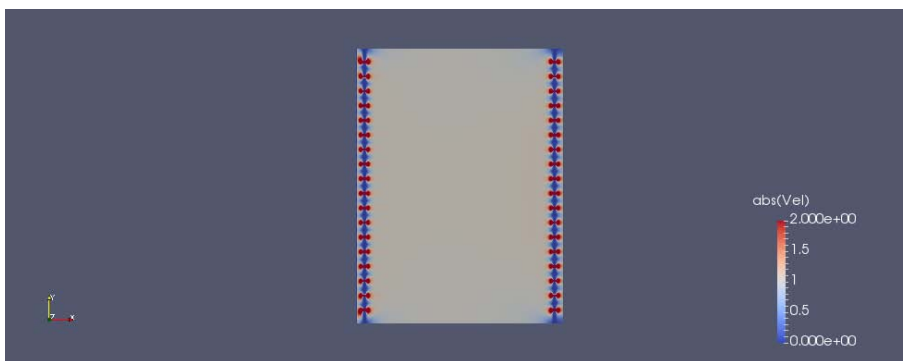


Figure A.5: Simulated abs velocity field (rescaled).

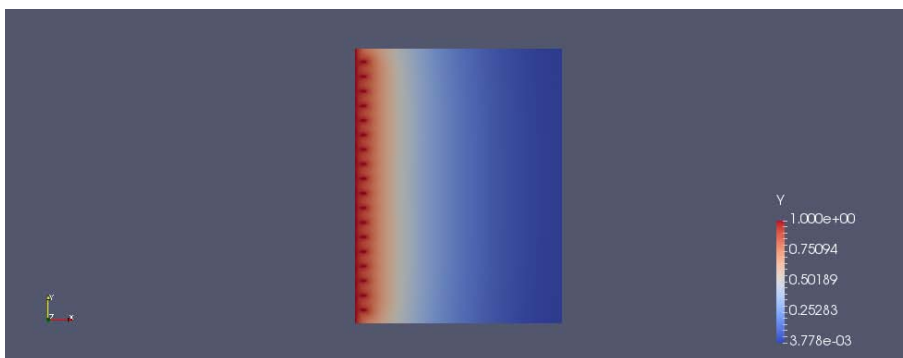


Figure A.6: Simulated concentration of chemical species.

flow rate Q^* calculated as follows from the Darcy's law:

$$Q^* = \frac{KL_yL_z}{\mu L_x \varepsilon} \Delta P \quad (\text{A.27})$$

$$Q^* = \frac{K}{L_z^2} \frac{L_y}{L_z} \frac{L_z}{L_x} \frac{1}{\varepsilon} \frac{L_z^3}{\mu} \Delta P \quad (\text{A.28})$$

$$Q^* = K^* \frac{L_y^*}{L_x^*} \frac{1}{\varepsilon} \frac{L_z^3}{\mu} \frac{\rho U^2}{\rho U^2} \Delta P \quad (\text{A.29})$$

$$Q^* = K^* \frac{L_y^*}{L_x^*} \frac{1}{\varepsilon} L_z^2 Re U \Delta P^* \quad (\text{A.30})$$

Where:

$$\Delta P^* = \frac{\Delta P}{\rho U^2} \quad (\text{A.31})$$

is the dimensionless differential pressure.

So, considering a flow rate Q_c equal to $1.1625\text{E-}5 [m^3 s^{-1}]$, and considering a dimensionless differential pressure resulting from the simulation equivalent to $6.536\text{E+}5$, the correspondent Q^* is $1.1351\text{E-}5 [m^3 s^{-1}]$. The difference between the two values of flow rate is only 2.35%. Now, comparing the value of real differential pressure equal to $39490 [Pa]$, and the simulated one equal to $40899 [Pa]$, we find that the committed error is 3.56%.

So, we can conclude that the simulation results show an excellent correspondence with experimental data. This means that we could simulate the behaviour of the porous electrode considering for example different materials, different dimensions, or different percentage of thickness compression in order to research and reach the better battery performances.

Bibliography

- [1] Moro, Trovò, Bortolin, Dal Col, Guarnieri, *An alternative low-loss stack topology for vanadium redox flow battery: Comparative assessment*, Journal of Power Sources 340 (2017) 229-241.
- [2] Kook Park, Shim, Hoon Yang, Chang-Soo Jin, Suk Lee, Young-Seak Lee, Shin, Jeon, *The influence of compressed carbon felt electrodes on the performance of a vanadium redox flow battery*, Electrochimica Acta 116 (2014) 447-452.
- [3] Alotto, Guarnieri, Moro, *Redox flow batteries for the storage of renewable energy: A review*, Renewable and Sustainable Energy Reviews 29 (2014) 325-335.
- [4] Xu, Zhao, Zhang, *Effects of SOC-dependent electrolyte viscosity on performance of vanadium redox flow batteries*, Applied Energy 130 (2014) 139-147.
- [5] Marini, *Attività di commissioning per un impianto sperimentale VRFB*, University of Padua, thesis (2017).
- [6] Chen, Hickner, Agar, Kumbur, *Optimizing membrane thickness for vanadium redox flow batteries*, Journal of Membrane Science 437 (2013) 108-113.
- [7] Chen, Hickner, Agar, Kumbur, *Optimizing membrane thickness for vanadium redox flow batteries*, Journal of Membrane Science 437 (2013) 108-113.
- [8] Sun, Skyllas-Kazacos, *Chemical modification and electrochemical behavior of graphite fibre in acidic vanadium solution*, Electrochimica Acta 36 (1991) 513-517.
- [9] Flox, Rubio-Garcia, Nafria, Zamani, Skoumal, Andreu, Arbiol, Cabot, Morante, *Active nano-CuPt₃ electrocatalyst supported on graphene for enhancing reactions at the cathode in all-vanadium redox flow batteries*, Carbon 50 (2012) 2372-2374.
- [10] Tsai, Yang, Ma, Xie, *Performance of a vanadium redox flow battery with and without flow fields*, Electrochimica Acta 77 (2012) 232-236.
- [11] Xu, Zhao, Zhang, *Preparation and electrochemical activation of iridium-decorated graphene as the electrode for all-vanadium redox flow batteries*, Electrochimica Acta 142 (2014) 61-67.
- [12] Skyllas-Kazacos, McCann, *Vanadium redox flow batteries (VRBs) for medium- and large-scale energy storage*, Woodhead Publishing Series in Energy 67 (2014) 329-386.

- [13] Minke, Turek, *Materials, system designs and modelling approaches in techno-economic assessment of all-vanadium redox flow batteries - A review*, Journal of Power Sources 376 (2018) 66-81.
- [14] U. S. Geological Survey, *Commodity statistics and information*, <http://minerals.usgs.gov/minerals/pubs/commodity/vanadium/>.
- [15] Radvak, *The International Flow Battery Forum*, (2012) 30-31.
- [16] Crawford, Viswanathan, Stephenson, Wang, Thomsen, Reed, Li, Balducci, Kintner-Meyer, Sprenkle, *Comparative analysis for various redox flow batteries chemistries using a cost performance model*, Journal of Power Sources 293 (2015) 388-399.
- [17] Ha, Gallagher, *Estimating the system price of redox flow batteries for grid storage*, Journal of Power Sources 296 (2015) 122-132.
- [18] Noack, Wietschel, Roznyatovskaya, Pinkwart, Tuebke, *Estimating the system price of redox flow batteries for grid storage*, Energies 9 (2016).
- [19] Mellentine, *Performance Characterization and Cost Assessment of an Iron Hybrid Flow Battery*, University of Iceland, University of Akureyri, thesis (2011).
- [20] Zhang, Moore, Watson, Zawodzinski, Counce, Electrochem, *Capital Cost Sensitivity Analysis of an All-Vanadium Redox-Flow Battery*, Journal of The Electrochemical Society 159 (2012) A1183-A1188.
- [21] Moore, Robert, Watson, Zawodzinski, Hareh, *A step-by-step design methodology for a base case vanadium redox-flow battery*, Chemical Engineering Education 46 (2012) 239-250.
- [22] Spellman, Stiles, Little, *Economic Report on Vanadium Redox Flow Battery with Optimization of Flow Rate*, University of Tennessee, Honors Thesis Projects (2013).
- [23] Viswanathan, Crawford, Stephenson, Kim, Wang, Li, Coffey, Thomsen, Graff, Balducci, Kintner-Meyer, Sprenkle, *Cost and performance model for redox flow batteries*, Journal Power Sources 247 (2014) 1040-1051.
- [24] Shibata, Sato, *Development of vanadium redox flow battery for electricity storage*, Power Engineering Journal (1999) 13(3):130-5.
- [25] Shigematsu, Kumamoto, Deguchi, Hara, *Applications of a vanadium redox-flow battery to maintain power quality*, IEEE/PES 2 (2002) 1065-1070.
- [26] Dawe, *Flow battery storage applications with wind power*, IEEE/PES GM (2005).
- [27] Hennessy, *Energy storage systems research program*, Annual peer review (2006).
- [28] McDowell, *International renewable energy storage conference*, IRES (2006).
- [29] Wesoff, Eric, St. John, Jeff, *Largest Capacity Flow Battery in North America and EU Is On-Line and Commissioned*, Greentech Media (2016).
- [30] Stone, Mike, *A Look at the Biggest Energy Storage Projects Built Around the World in the Last Year*, (2017).

- [31] Energy Storage Association, *UET and Snohomish County PUD Dedicate the World's Largest Capacity Containerized Flow Battery*, Energy Storage News (2017).
- [32] Herald, *PUD invests \$11.2 million in energy-storing units*, (2017).
- [33] Energy Storage Association, *SDG&E and Sumitomo unveil largest vanadium redox flow battery in the US*, Energy Storage News (2017).
- [34] Endress+Hauser, *Operating Instructions Proline Promag 50P, 53P*.
- [35] Endress+Hauser, *Operating Instructions Deltabar S FMD77, FMD78, PMD75*.
- [36] Wikipedia, <https://it.wikipedia.org/wiki/LabVIEW>.
- [37] National Instruments, *Datasheet NI 9207*.
- [38] National Instruments, *Datasheet NI 9209*.
- [39] National Instruments, *Datasheet NI 9216*.
- [40] National Instruments, *Datasheet NI 9263*.
- [41] Munson, Young, Okiishi, Huebsch, *Fundamentals of Fluid Mechanics*, John Wiley & Sons, Inc. (Sixth Edition).
- [42] Aaron, Tang, Papandrew, Zawodzinski, *Polarization curve analysis of all-vanadium redox flow batteries*, Journal Application Electrochemical 41 (2011) 1175-1182.
- [43] Sanso, *Datasheet New Magnet Pump-PMD series*.
- [44] Breugem, Boersma, *Direct numerical simulations of turbulent flow over a permeable wall using a direct and a continuum approach*, Physics of Fluids 17 (2005).
- [45] Whitaker, *The Forchheimer equation: a theoretical development*, Porous media 25 (1996).
- [46] Costa, *A FFT-based finite-difference solver for massively-parallel direct numerical simulations of turbulent flows*, KTH, Department of Mechanics, SE-100 44 Stockholm, Sweden.
- [47] Wesseling, *Principles of computational fluid dynamics*, Springer Science & Business Media 29 (2009).
- [48] Li, Xiong, Tang, Qin, Liu, Yan, *Investigation of the use of electrolyte viscosity for online state-of-charge monitoring design in vanadium redox flow battery*, Applied Energy 211 (2018) 1050-1059.